Theory and Application of SBS-based Group Velocity Manipulation in Optical Fiber

by

Yunhui Zhu

Department of Physics
Duke University

Date: _____

Approved:

_____
Daniel J. Gauthier, Supervisor

_____
Henry Greenside

_____
Jungsang Kim

_____
Haiyan Gao

_____
David Skatrud

Dissertation submitted in partial fulfillment of the requirements for the degree of
Doctor of Philosophy in the Department of Physics
in the Graduate School of Duke University
2013

ABSTRACT

Theory and Application of SBS-based Group Velocity Manipulation in Optical Fiber

by

Yunhui Zhu

Department of Physics
Duke University

Date: _____

Approved:

_____
Daniel J. Gauthier, Supervisor

_____
Henry Greenside

_____
Jungsang Kim

_____
Haiyan Gao

_____
David Skatrud

An abstract of a dissertation submitted in partial fulfillment of the requirements for the degree of Doctor of Philosophy in the Department of Physics in the Graduate School of Duke University
2013

Abstract

All-optical devices have attracted many research interests due to their ultimately low heat dissipation compared to conventional devices based on electric-optical conversion. With recent advances in nonlinear optics, it is now possible to design the optical properties of a medium via all-optical nonlinear effects in a table-top device or even on a chip.

In this thesis, I realize all-optical control of the optical group velocity using the nonlinear process of stimulated Brillouin scattering (SBS) in optical fibers. The SBS-based techniques generally require very low pump power and offer a wide transparent window and a large tunable range. Moreover, my invention of the arbitrary SBS resonance tailoring technique enables engineering of the optical properties to optimize desired function performance, which has made the SBS techniques particularly widely adapted for various applications.

I demonstrate theoretically and experimentally how the all-optical control of group velocity is achieved using SBS in optical fibers. Particularly, I demonstrate that the frequency dependence of the wavevector experienced by the signal beam can be tailored using multi-line and broadband pump beams in the SBS process. Based on the theoretical framework, I engineer the spectral profile to achieve two different application goals: a uniform low group velocity (slow light) within a broadband spectrum, and a group velocity with a linear dependence on the frequency detuning (group velocity dispersion or GVD).

In the broadband SBS slow light experiment, I develop a novel noise current modulation method that arbitrarily tailors the spectrum of a diode laser. Applying this method, I obtain a 5-GHz broadband SBS gain with optimized flat-topped profile, in comparison to the $\sim$ 40 MHz natural linewidth of the SBS resonance. Based on the broadband SBS resonance, I build a 5-GHz optical buffer and use this optical buffer to delay a return-to-zero data sequence of rate 2.5 GHz (pulse width 200 ps). The fast noise modulation method significantly stabilizes the SBS gain and improves the signal fidelity. I obtain a tunable delay up to one pulse-width with a peak signal-to-noise ratio of 7. I also find that SBS slow light performance can be improved by avoiding competing nonlinear effects. A gain-bandwidth product of 344 dB·GHz is obtained in our system with a highly-nonlinear optical fiber.

Besides the slow light applications, I realize that group velocity dispersion is also optically controlled via the SBS process. In the very recent GVD experiment, I use a dual-line SBS resonance and obtain a tunable GVD parameter of 7.5 ns^2/m, which is 10^9 times larger than the value found in a single-mode fiber. The large GVD system is used to disperse an optical pulse with a pulse width of 28 ns, which is beyond the capability for current dispersion techniques working in the picosecond and sub picosecond region. The SBS-based all-optical control of GVD is also widely tunable and can be applied to any wavelength within the transparent window of the optical fiber. I expect many future extensions following this work on the SBS-based all-optical GVD control using the readily developed SBS tailoring techniques.

Finally, I extend the basic theory of backwards SBS to describe the forward SBS observed in a highly nonlinear fiber, where asymmetric forward SBS resonances are observed at the gigahertz range. An especially large gain coefficient of 34.7 W^{-1} is observed at the resonance frequency of 933.8 MHz. This is due to good overlap between the optical wave and the high order guided radial acoustic wave. The interplay from the competing process known as the Kerr effect is also accounted for in the theory.

Acknowledgements

The six years of my Ph.D. study in Duke Physics has been truly enjoyable in a quite unexpected way and this is of course due to the intelligent, passionate people I live and study with, and I can only name a few here. First and foremost, I want to thank my advisor, Prof. Daniel Gauthier, for his knowledge, mentorship and strict but patient guidance. I could never make it this far without his encouragement and incitations. I also want to thank Prof. Jungsang Kim and Prof. Mark Neifeld for their guidance on my research projects.

I have enjoyed working with all of my colleagues in the Quantum Electronics Lab, and I want to thank all my collaborators, Edu Cabrera-Granado, Rui Zhang, Jing Wang, Myungjun Lee, Hannah Guilbert and Joel Greenberg. I have learnt a lot from cooperation in experiments and white board discussions. I also thank the non-optical half of the group who answered all of my electronic questions in the lab. Specific recognition goes to my thesis reader Hannah Guilbert, for insightful suggestions and tedious work on word editing.

Finally, I thank my friends and family for making life easy and comfortable, particularly my roommate Baiyu Chen, who helped me keep my life organized, and my wonderful husband Hang Yu who absorbed all my frustrations. I shall never forget what I learned and experienced during my years as a graduate student of physics.

Contents

List of Figures

List of Tables

1

Overview

1.1 Motivation: Slow light and design of the optical properties of materials

Slow light has become a highly researched topic since the discovery of a dramatic reduction of the group velocity in 1999 [1]. The group velocity, which refers to the speed at which a light pulse travels in the medium, was reduced to 17 m/s, and later completely stopped [2] in nonlinear optical materials. This interesting optical phenomena is generated by optically induced nonlinear optical resonances, which modify the complex susceptibility of the material dramatically at the vicinities of the resonances. By using different kinds of resonances, the group velocity can be dramatically changed in different ways. In fact, the group velocity can be made very small, known as "slow light," or very large (larger than the speed of light in vacuum), known as "fast light," or even negative [3–6]. The unprecedent small and large values of group velocities have attracted a lot of research interests. For example, there has been a lot of research on the fundamental physics of the information speed in fast light materials, which is verified to be non-superluminal, thus does not violate casuality [7].

Moreover, the control of group velocity in fast and slow light experiments has al-

lowed the design of optical properties of materials via nonlinear optical interactions. While initial slow/fast light experiments control the group velocity via natural nonlinear optical resonances, advanced techniques, starting from broadband slow light, have been developed to artificially engineer the profile and resonant frequency of the optical resonances. Using advanced techniques that tailor arbitrarily nonlinear optical resonances and that I developed, it is now possible to modify the optical properties of materials with a high degree of control, designing the resonance wavelength, bandwidth and wavevector profiles at will. As a result, I am able to design functional optical material with properties that optimize function performance [8, 9]. In addition, this technique has been extended to general optical property design beyond fast/slow light. As one example, I have successfully made the group velocity linearly dependent on the frequency, resulting in a huge group velocity dispersion 10^9 times larger than that in normal optical fiber [10].

Optical control of the optical properties of medium is important also due to its implications for all-optical computation [4, 11]. The manipulation of an optical pulse using another light beam enables interesting all-optical applications, such as all-optical switching [12], all-optical buffer [13] and all-optical storage [2, 14]. Traditionally, optical signals transferred through the telecommunication channels need to be converted into electronic signals and then processed by electronic devices. After the processing, the electronic signals are converted back into optical pulses to be sent through optical channels again. Heat dissipation from the conversion procedure is considered as the ultimate limit of processing speed [15]. All optical devices solve this problem by eliminating the need for optical-electric-optical conversion, and thus are expected to greatly enhance the speed.

The control of the group velocity was first demonstrated in atomic gases [1], but the technique has only become popular and widely applicable after the recent demonstration of slow and fast light in optical fiber via simulated Brillouin scattering (SBS),

in which our group is a major contributor [8, 9, 16–18]. Compared to the atomic gas system, optical fiber based SBS slow light system enjoys a much simpler table-top configuration. It is also much more flexible in terms of resonant frequency, which is tunable over the whole transparent range of the optical fiber, while the resonance frequencies of the atomic resonances are usually fixed. The incoherent nature of the SBS resonance is also key to the development of the arbitrary SBS tailoring technique. Using this technique, we are able to realize bandwidths up to tens of gigahertz, a bandwidth that is compatible with the data rates of modern optical communication channels. As mentioned before, the technique I developed also enables arbitrarily reshaping of the profiles of SBS resonance, extending the fast/slow light techniques into general optical property design.

In this thesis, I present my contributions in the recent development of group velocity control using SBS in optical fibers. This is still a rapidly emerging field, and many of the techniques and applications I present in the thesis are still in progress.

1.2 Background

1.2.1 Stimulated Brillouin scattering in optical fiber

Brillouin scattering is a nonlinear opto-acoustic coupling process in which an incident pump beam is scattered by propagating acoustic vibrations in a nonlinear material, most commonly an optical fiber. The scattered optical beam acquires a frequency shift characterized by the Brillouin frequency, Ω_B, in the material. From a quantum mechanical standpoint, the photons in the counter-propagating optical beams are coupled to the excitation quanta of phonons in the medium. In an optical fiber, where light waves and acoustic vibrations are tightly confined, a self-reinforced process occurs between the optical and acoustic waves, giving rise to the stimulated Brillouin scattering (SBS) process. In this process, the interference beat between the two optical waves stimu-

lates acoustic vibrations, and the acoustic waves in turn scatters light wave from the higher frequency beam into the lower frequency beam, thereby reinforcing the optical interference beat. The SBS process can be very efficient in optical fibers even at low power levels ($\sim$ mW), giving rise to strong gain and/or absorption resonances.

SBS was first reported by Chiao *et al.* since 1964 [19, 20] and has been extensively studied even since [20, 21]. SBS is the dominant nonlinear scattering process in an optical fiber [22] and plays a limiting role in passive optical fiber transmission channels. SBS detracts a large amount of power from the input beam into the backward direction, and thus limits the maximum amount of power that can be transmitted over a fiber [22, 23]. On the other hand, SBS is useful when utilized in active applications such as fiber-based Brillouin amplifiers and lasers.

In this thesis, I intentionally utilize the SBS process to modify the refractive index and group velocity in the optical fiber. Techniques based on SBS in optical fibers benefit from the low power requirement, tunable resonant frequency, wide range of transparent window, inexpensive setup and room-temperature operation, all of which makes all-optical fast and slow light applications easy and accessible, leading to a boom of research interest in this field [4].

1.2.2 Group index and slow light

The propagation of a light wave in optical materials is characterized by the refractive index n, defined as

$$n = \frac{c}{v_p}, \tag{1.1}$$

where c is the speed of light in vacuum and v_p is the phase velocity of light wave in the material. As a result of phase retard of the reemitted waves from the atoms of the material, the overall phase propagation of the light wave is slightly delayed. For common materials, such as air, water and silica, the refractive index value usually falls

into the range of $1 < n < 3$ at visible and infrared wavelength ranges. For example, diamond has a large refractive index of 2.46.

However, the phase velocity cannot accurately describe the propagation of the intensity profile of a temporally-varying optical wave. To characterize the propagation of an optical pulse in materials, I refer to the group index n_g, defined as

$$n_g = \frac{c}{v_g}, \tag{1.2}$$

where v_g is the group velocity of the light wave in the material. The group index is obtained by

$$n_g = n + \omega \frac{dn}{d\omega}, \tag{1.3}$$

where ω is the frequency of the light wave.

Usually, refractive index has little dependence on the frequency of the light wave, and therefore the value of group index is similar to that of the refractive index, *i.e* $n \sim n_g$.

In 1999, however, Professor Hau's group has successfully reduced group velocity of a light wave to 17 m/s in atomic gases, corresponding to a group index of 1.7×10^7 (Fig. 1.1). Such a dramatic reduction of group velocity is known as the slow light. The extremely small group velocities are found at the vicinity of an optical resonance, where large dispersion occurs in a narrow spectral region. We see from Eq. (1.3) that a large normal dispersive term $dn/d\omega$ results in a small v_g.

Slow light with remarkably low group velocity is a promising solution for spatial compression of optical energy and the enhancement of linear and nonlinear optical effects. The continuously tunable delay lines also provide great opportunities in optical telecommunication for data buffering, synchronization and jitter correction [13, 14, 24], as well as in interferometry for scanning a reference arm without moving parts [25–27] and slow light radar [28]. As a result, achieving slow light in a

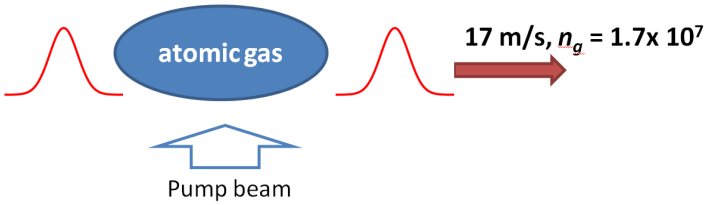

FIGURE 1.1: Slowlight in atomic gases.

wide variety of material systems using different physical mechanisms is a topic of intensive study [1, 29, 30]. Among various slow light approaches, stimulated-Brillouin-scattering-based slow light in single-mode optical fibers has attracted much interest since 2006, when our group and Professor Thévenaz's group demonstrated the idea of broadband SBS [5, 31]. Because of the optically controllable delay time and tunability of the bandwidth [31, 32], stimulated Brillouin scattering (SBS) slow light devices demonstrate great potential for all-optical applications and many research works have followed in recent years [2, 3, 8, 9, 16, 18, 33].

1.2.3 Optical buffer

A direct application of slow light is the optical buffer. Buffering refers to the temporal storage of information by the delay of signal flow (see Fig. 1.2). It is a fundamental function in the telecommunication and data processing systems [13, 34]. While ordinary buffers delay electronic signals, an optical buffer is a device that delays optical pulses. By bypassing the step of converting optical signals to the electrical ones, as needed for conventional buffering, optical buffers offer the potential for faster optical communications. Recently, research interest in slow-light has boosted the development of all-optical slow-light based optical buffers [4, 9, 13]. Large optical pulse delay has been observed in several slow-light experiments [1, 29, 30].

Among various slow-light buffering approaches, SBS-based slow-light optical buffers provide optically tunable resonance wavelength and delay time, which has been shown

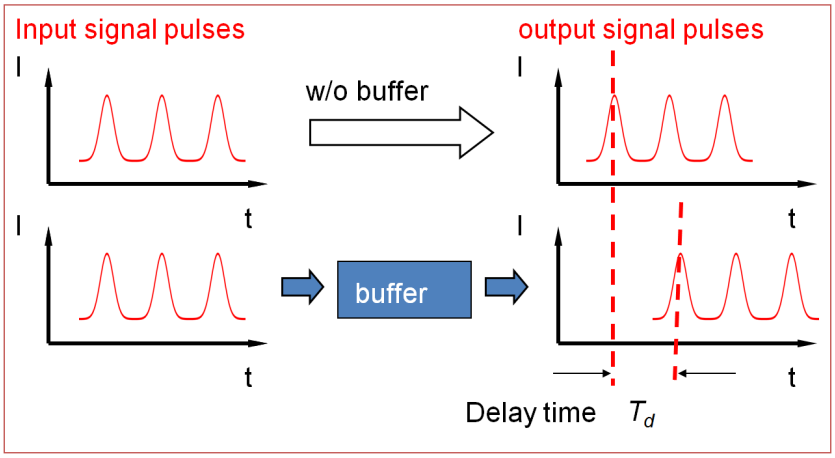

FIGURE 1.2: An optical buffer delays the propagation of optical pulse sequences. T_d is the delay time of the optical buffer

to benefit applications such as optical packet switches and data synchronization [13, 24].

In SBS slow light devices, the bandwidth is determined by the linewidth of the SBS resonance. The intrinsic linewidth, Γ_B, of the resonance in a normal single-mode fiber is ~40 MHz (FWHM), which is determined by the decay rate of acoustic phonons in the optical fiber [35]. The data rate in such a system is limited to ~Γ_B, insufficient for modern optical communication applications with GHz data rates. To solve this problem, broadband SBS slow light has been developed, in which the linewidth of the SBS resonance is broadened using a multi-frequency laser source as the pump beam [33, 36–38]. Specifically, a multi-channel SBS slowlight system has been demonstrated by passing an incoherent pump laser source through a spectral-slicing filter [33].

Professor Gonzalez-Herráez *et al.* and our group first demonstrated broadband SBS by tailoring the pump spectrum in 2006 [31] and 2007 [16]. Using the well-known Brillouin spectrum broadening technique by direct current modulation of a semiconductor pump laser [39], Gonzalez-Herráez increased the SBS bandwidth to ~325 MHz [31]. Since then, a number of research groups have successfully broadened

the bandwidth of the SBS slow light, making it much larger than the intrinsic linewidth of SBS resonance [9, 16, 40]. Broadband SBS slow-light has been demonstrated with bandwidths up to tens of GHz [8, 18, 41], a data rate compatible with modern optical communication systems.

Applying the arbitrary tailoring technique I developed to the broadband optical buffer, I find improvement of delay and reduced distortion under pump power constraints [18, 42]. Fractional delays as large as three have been demonstrated recently [18].

1.2.4 Competing effects

In broadband SBS slow light applications, performance of the device can be degraded due to competing optical nonlinear effects. These nonlinear effects are enhanced by the large pump power required to generate the broadband SBS resonance. Amplified spontaneous Brillouin scattering has been discussed as an intrinsic limitation on SBS in many previous works [43–45]. Other competing effects such as stimulated Raman scattering [39], Rayleigh backscattering [46]. Recently, I also find that modulation instability caused by Kerr nonlinearity [8] also degrades slow light performance in broadband SBS systems.

The competing processes affect the SBS slow light in two ways.

- Depletion of the pump power. Competing effects can transfer power in the pump beam into non-optical forms, counter-propagating directions, or into other frequency ranges. The depletion of the pump power reduces the attainable SBS gain and thus limits the slow light delay.

- Generation of noisy beams that mix with the signal. Some of the competing effects generate beams that co-propagate with the signal beam. Because these generated beams are initiated from amplification of thermal and quantum noises,

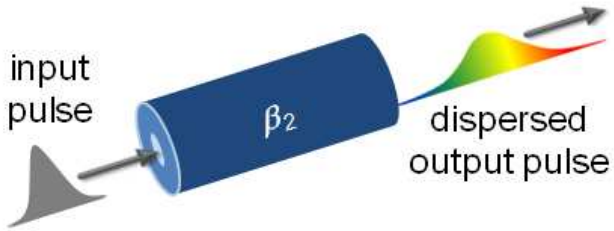

FIGURE 1.3: An input transform-limited optical pulse broadens temporally and develops a linear frequency chirp as it propagates through a material with group velocity dispersion parameter β_2

they are noisy in nature and reduce the signal-to-noise ratio for the slow light operation.

A good SBS-based device needs to eliminate and/or suppress the completing effects to optimize its performance.

1.2.5 Group velocity dispersion

Group velocity dispersion (GVD) refers to the linear dependence of group velocity on frequency. Upon propagation in a GVD material, different frequency components travel at different group velocities, and are relocated to different temporal positions. A transform limited optical pulse with a short temporal duration (thus a broad spectrum) will get broadened propagating in a GVD material, as shown in Fig. 1.3. In addition, the spectrum of the optical wave is displayed in the temporal domain. GVD material is widely used in various applications such as short pulse manipulation [47, 48], temporal domain Fourier optics [49, 50] and quantum information processing [51–53]. Breakthrough research over the past decade has demonstrated unprecedented control over the frequency-dependent refractive index of optical materials. For example, it is now possible to obtain negative values of the refractive index using metamaterials [6] and extremely large or negative values of the group index using laser-induced mate-

rial resonances or photonic crystals [4]. In contrast, engineering the group velocity dispersion (GVD) is limited to the domain of broadband, ultra-fast light pulses [54]. Yet, emerging applications, such as quantum key distribution [49, 50], quantum [51] and classical [48, 52, 55] information processing, and temporal cloaking [56], require or can benefit from large GVD that can disperse longer duration pulses. I demonstrate giant values of the GVD parameter β_2 are obtained by arranging the SBS resonances and placing the amplifying resonance next to an absorbing resonance.

1.2.6 Forward SBS

Besides the commonly used backwards SBS, the unconventional SBS in the forward direction has attracted research interest in recent years. Forward spontaneous Brillouin scattering (FSBS) in optical fibers was first discussed by Shelby *et al.* [57] in a process known as guided acoustic-wave Brillouin scattering (GAWBS). Since then, GAWBS has been extensively explored in fibers with different core dimensions and polarization properties [58–61]. The FSBS process between two non-degenerate optical modes was first characterized by Russell *et al.* [62], where the frequency shift was of-the-order-of 17 MHz. More recently, highly efficient FSBS at gigahertz frequencies has been demonstrated by Kang *et al.* [63] using a small-core (diameter 2 μm) photonic crystal fiber (PCF) coupling to the torsional and radial modes. Current researches on FSBS at gigahertz frequencies suggest that the process may be used in a wide variety of photonic applications, such as frequency comb generation, active phase modulation, optical frequency conversion, and high-frequency mode locking of fiber lasers [58, 59, 64].

1.3 Outline

The rest of the thesis is organized as follows. In Ch. 2, I present the theory of SBS in an optical fiber. In this chapter, I derive the effective wavevector K, which represents

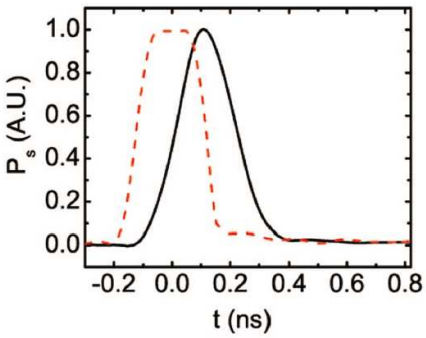

FIGURE 1.4: Slow light performance using periodic modulation method in HNLF. Averaged output signal profiles at pump power $P_p = 350$ mW for a single pulse (black solid line), together with the undelayed pulse profile at $P_p = 0$ mW (red dashed line) in HNLF. A delay of 160 ps is shown at this pump power.

the modified optical properties of the optical fiber under the modulation of the SBS resonance. The refractive index and group velocity are obtained from the real part of the wavevector K. Particularly, I derive the SBS resonance with multiple pump lines and broadband pump beams. This is the theoretical framework for the SBS resonance tailoring and optimization technique.

In Ch. 3, I present the theory for the broadband slow light using a rectangular-shaped SBS gain profile. I describe my experiment where I generate and optimize such a flat-topped gain profile using periodic current modulation of the diode pump laser source. I experimentally demonstrate a delay for an optical pulse of 200-ps width (shown in Fig. 1.4). The delay time is in good agreement with the prediction of model.

In Chapter 4, I introduce my arbitrary SBS tailoring technique using noise current modulation. I apply the novel technique into the optimization of a broadband SBS optical buffer. The experiment I performed shows significant improvement compared to previous methods in that the arbitrarily tailored resonance yields much more stable output signals. The data fidelity measurements of the broadband optical buffer show that this method profoundly reduces SBS gain fluctuations and improves signal data fidelity, while maintaining the delay performance. A preview of the eye diagram for

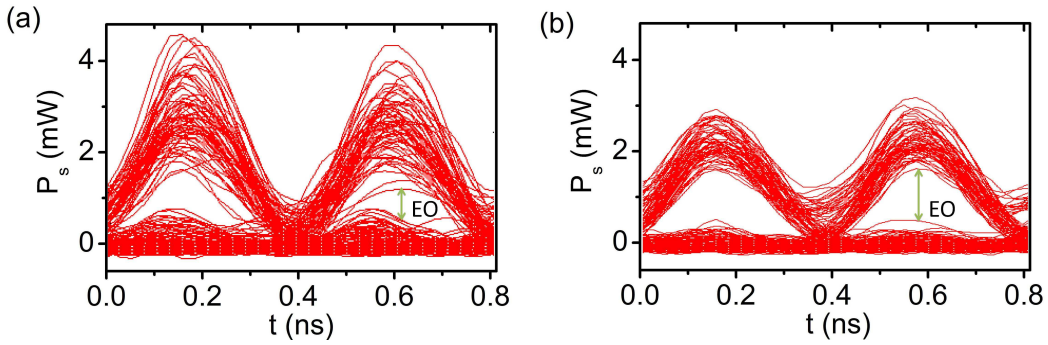

FIGURE 1.5: Eye diagrams of delayed and amplified data sequences for (a) slow and (b) fast modulation waveforms at $P_p = 350$ mW in HNLF. The arrows in the figure show the EO for each case. A 50% increase of EO is demonstrated in the fast modulation method.

the fast and slow modulation method is shown in Fig. 1.5, where the improvement of data eye-opening is significant.

In Chapter 5, I introduce common competing processes and analyze their effect on the broadband SBS slow light system. Particularly, I discover that pump depletion occurs as a result of the modulation instability (MI) in a LEAF fiber and quantify the limitation on delay-bandwidth product in the experiment. To my knowledge, this is the first analysis of the modulation instability in SBS experiments. The results show that MI is suppressed in a normal dispersive optical fibers in the SBS fast/slow light experiments. The criterion is useful in future design of fiber based SBS applications.

In Ch. 6, I extend the arbitrary SBS resonance tailoring technique into general optical property design beyond slow/fast light. Instead of designing a resonance to obtain a large group velocity, I obtain an SBS modified material with an unprecedent large group velocity dispersion. The recent experiment on the exceptionally large group velocity utilizes a dual-lined SBS resonance in an optical fiber. The GVD parameter, β_2, is 10^9 times larger than that in silica fibers without the SBS resonance. This is the first demonstration of using SBS to optically control the group velocity dispersion. The large GVD in this experiment greatly enlarges the range of dispersion values that

we can obtain, enables dispersive techniques for optical pulses in the nanosecond (ns) region. Similar to the invention of slow light using SBS in optical fiber, this work is expected to greatly reduce the complexity of experimental setup and thus makes GVD control widely applicable, even in previously unconsidered temporal scales.

In Ch. 7, I reconsider the fundamental aspects of the SBS process and describe the observation of the forward stimulated Brillouin scattering in a highly nonlinear optical fiber. In this process, co-propagating optical beams are coupled to the radial guided modes of acoustic vibration in the optical fiber. The strong coupling between the guided radial acoustic wave and the optical wave in a single mode fiber was previously considered unlikely. I prove both theoretically and experimentally that the strong FSBS resonances in the application-favorable gigahertz range do exist. The findings significantly lower the cost and increase the accessability for the FSBS applications. The many different modes of guided acoustic vibrations in a cylindrical waveguide give rise to multiple FSBS resonance peaks with different resonant frequencies. I calculate the coupling strength for these multiple resonances. Additionally, interplay with Kerr effect is accounted for in our theoretical model and experiment.

Finally, in Ch. 8, I summarize the main results and suggest future work directions.

2

Theory of stimulated Brillouin scattering in optical fiber

This chapter covers the theoretical framework for stimulated Brillouin scattering (SBS) in an optical fiber. I will first review nonlinear optical processes in an optical fiber, including a number of competing nonlinear effects other than SBS that will become relevant in the following chapters. I will then present the theory of acoustic-optical coupling in an optical fiber and derive the solution for a stimulated Brillouin scattering resonance pumped by a monochromatic laser beam. The presence of SBS change dramatically the effective refractive index profile as experienced by the signal beam. Furthermore, by tailoring the SBS resonance profile with multiple-line or distributed broadband pump beam, the optical properties of the SBS resonance can be controlled and optimized for specific applications. The theoretic framework laid out in this section is used throughout the rest of the thesis.

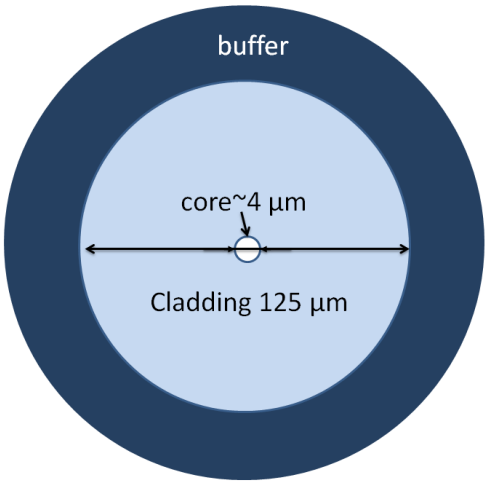

FIGURE 2.1: structure of a highly nonlinear optical fiber

2.1 Nonlinear optical processes in an optical fiber

2.1.1 Optical fiber

Optical fiber is the most widely used optical waveguide in the modern world [19, 65, 66]. An optical fiber is a transparent waveguide typically made of high quality extruded glass (silica). It is composed of the large cladding and a small core area (see Fig. (2.1)), where the refractive index is slightly larger than that in the cladding material. The refractive index difference causes internal total reflection that confines light tightly in the core of the fiber. Power in the light wave is thereby confined inside the transparent fiber and is transmitted over large distances with minimum loss [19, 65]. Particularly, in a single mode fiber, the optical field is only allowed in one mode called the HE_{11} mode [65], which is a nearly azimuthally symmetric radial profile concentrated in the core area.

Apart from its important role of passive optical signal transmission in fiber-optic communications [66], optical fiber is also a very popular and important waveguide for the study of active nonlinear optical processes [19, 66]. Nonlinear optical phenomena are usually enhanced in optical fiber due to the tight confinement of the optical wave

that dramatically increases the light intensity for a given power, and also due to the propagation distances that enables long interaction length. For example, a typical highly nonlinear optical fiber confines the light field to a mode area of $\sim$ 10 μm^2 through a distance of several km, while the length of a nonlinear crystal is typically on the order of a few millimeters and the focal light field area is $\sim$ 100 μm^2. As a result, nonlinear effects can be evident at much lower power levels inside an optical fiber [19].

2.1.2 Nonlinear susceptibility

The response of an optical fiber to a light wave is mostly linear and fast, i.e, the polarization $P(t)$ of the material is proportional to the amplitude of the input light field $E(t)$ by [67, 68]

$$P(t) = \epsilon_0 \chi E(t), \tag{2.1}$$

where ϵ_0 is the permittivity of vacuum, and χ is the linear susceptibility. While E and P are vectors in general, I simplify the description by limiting E and P in one of the two orthogonal polarization modes inside the optical fiber [65]. This polarization is called the linear polarization P^L. The time-varying material polarization $P(t)$ is the source for generating new optical fields.

However, with high intensity light waves confined in the small core area of an optical fiber, the fiber response P deviates from the simple linear relation. In this case, the polarization P contains both linear and nonlinear parts, $P = P^L + P^{NL}$ [68].

Nonlinear optical processes are treated by expanding the polarization to include higher-order contributions [19]. In doing that, we assume that the response of the polarization P to the higher-order terms of light field E is important, but small enough so that the nonlinear response can be treated as a perturbation. In this case, the

polarization is expanded as

$$P(t) = \epsilon_0(\chi_1 E(t) + \chi_2 E(t)^2 + \chi_3 E(t)^3 + ...), \tag{2.2}$$

where the nonlinear susceptibilities χ_2 and χ_3 are called the second and third-order susceptibility, respectively. Here, the nonlinear polarization $P^{NL} = \chi_2 E(t)^2 + \chi_3 E(t)^3 + ...$

Usually, the second-order nonlinearity is the leading nonlinear term. However, only materials with asymmetric orientations (such as noncentrosymmetric crystals) are capable of demonstrating a second-order susceptibility [68]. Optical fibers made of amorphous silica have zero second-order susceptibility and hence the leading-order nonlinearity is proportional to third-order susceptibility (χ_3), giving rise to the optical Kerr effect and third-harmonic generation, for example [19].

In the Kerr effect, an intense optical wave modulates the refractive index of the material and induces light scattering from the refractive index variations. For example, in a four-wave-mixing process, two intense pump waves modulate the refractive index of the optical fiber and create a moving refractive index grating at the beat frequency of the two pump beams. A weak beam input into the waveguide scatters off the grating, and is converted into light beams with new frequencies up or down shifted by the frequency difference of the two pump beams. This kind of process is known as the parametric processes because the final status of the material is unchanged; thus only "parametricly" involved in the light scattering process

The optical Kerr effect gives rise to processes such as self phase modulation, cross phase modulation, four-wave mixing and the modulation instability. These effects are readily observable in optical fibers and I will discuss them as competing processes in Chs. 3 and 7.

Apart from parametric Kerr effects, nonlinear light scattering takes place when the final state is different from the initial state. This type of nonlinear process alters the

states of the optical fiber and induces inelastic light scattering that couples light field with the internal states of the fiber material. It is called nonlinear light scattering, including [68]

- Raman scattering, interaction of light with the vibrational modes of the molecules in optical fiber, or optical phonons,
- Brillouin scattering, interaction of light with the propagating pressure/density wave, or acoustic phonons,
- Rayleigh scattering, interaction of light with static density distribution

A full description of the nonlinear light scattering processes thus involves both optical and vibrational waves in the optical fiber and an optical-acoustic coupling theory is required.

2.2 Stimulated Brillouin scattering

2.2.1 Overall interpretation

Brillouin scattering is light wave scattering from a propagating sound wave in optical fiber [19, 68]. In typical Brillouin scattering processes, the light wave and sound waves are coupled via electrostriction and the density-induced refractive index changes in the optical fiber medium. (A less common type of Brillouin scattering is caused by absorption of light that induces temperature changes and hence density changes.) On one hand, a strong optical field induces material density variations via electrostriction, which makes the material more dense in areas with high optical intensity. On the other hand, density variations change the refractive index of the material, which in turn act as optical gratings that scatters light wave into the down-shifted (Stokes) and up-shifted (anti-Stokes) frequencies. When there is only one external beam applied, the sound wave and the scattered light field are generated from noise (thermal noise

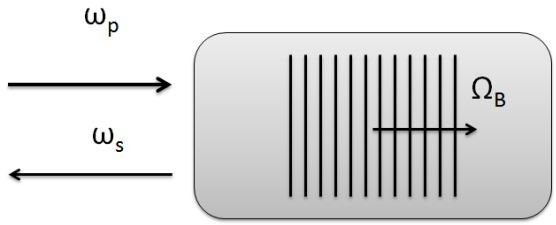

FIGURE 2.2: Geometry of the SBS processes. Two counter-propagating beams (signal beam frequency ω_s and pump beam frequency ω_p) are coupled to the longitude acoustic wave (frequency Ω_B).

and/or quantum noise)[45, 68, 69], and such a process is called spontaneous Brillouin scattering.

When there is an additional external seeding signal beam, a resonant stimulated Brillouin scattering (SBS) process can occur [19, 68] in both the backward direction (Fig. 2.2) and the forward direction (to be discussed in Ch. 7). Stimulated Brillouin Scattering takes place when a signal beam of frequency ω_s and a strong pump beam of frequency ω_p are coupled to an acoustic wave in an optical fiber [68]. The interaction between the three fields leads to strong coupling when the frequency difference of the light waves matches the frequency of the acoustic excitation (Brillouin frequency Ω_B) in the medium. When the frequencies are matched, the beating from the interference of the two optical waves produces a propagating density wave in the fiber. This acoustic wave then in turn acts as a refractive index grating that scatters the higher-frequency beam into the lower-frequency beam, inducing an amplification/absortion of the signal beam. When the signal beam is on the lower-frequency side, i.e, the Stokes side, the amplification of the Stokes beam increases the intensity of the beat signal between the optical waves and thus reinforces the sound wave. The self-enhanced feedback results in an exponential increase of the signal beam, efficiently transferring optical power into the signal beam until depletion of the pump beam sets in.

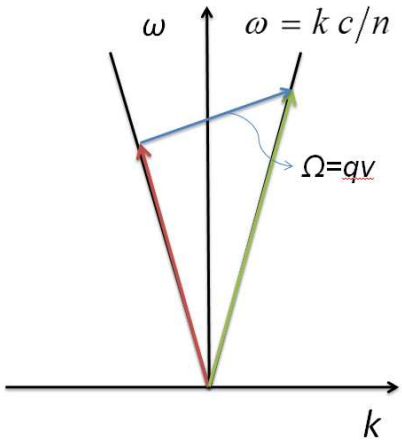

FIGURE 2.3: Energy and phase matching conditions for the backward SBS. The solid curve is the optical dispersion relation. The green and red arrows denote the optical beams, and the blue arrow denotes the acoustic wave.

2.2.2 Energy and phase matching conditions and Brillouin frequency Ω_B

We can obtain the value of Brillouin frequency Ω_B through simple energy and phase matching conditions. In order to obtain a strong coupling, the frequency and wavevector of the beating between the optical fields must match that of the acoustic wave. The energy and phase matching conditions are given by [19]

$$\begin{aligned} \Omega &= \omega_p - \omega_s, \\ q &= k_p - k_s, \end{aligned} \tag{2.3}$$

respectively, where Ω is the frequency of the acoustic wave, k_p, k_s and q are the wavevectors of the optical beams and the acoustic wave. Note that a negative sign of wavevector is assumed when it counter-propagates with the pump beam. Figure 2.3 shows the energy and phase matching conditions for the backward SBS process.

The phase matching conditions cannot be fulfilled for arbitrary ω_p and ω_s due to constraints on the dispersion relationship for optical and acoustic waves. In the case

of backward SBS, these dispersion relationships are given by [19]

$$\begin{aligned} |k_j| &= n\omega_j/c,\ (j=s,p) \\ q &= \Omega/v, \end{aligned} \tag{2.4}$$

where c is the speed of light in vacuum, n is the refractive index of the optical fiber and v is the speed of sound in the material. Combining Eq. (2.3) and Eq. (2.4), energy and phase matching are achieved when

$$\Omega = \frac{\frac{2v}{c/n}\omega_p}{1+\frac{v}{c/n}} \equiv \Omega_B \approx \frac{2v}{c/n}\omega,\ q = 2n\omega/c, \tag{2.5}$$

where $\omega = \omega_p \approx \omega_s$. Note that the approximation is valid because $v \ll c/n$ in an optical fiber.

2.2.3 Acoustic-optical coupling in optical fiber

To describe the acoustic-optical coupling between optical field $E(t)$ and material density variation $\rho(t)$ in full detail, we refer to the coupling equation between P and E derived from the Maxwell equations, given by [19, 68]

$$\nabla^2 E - \frac{n^2}{c^2}\frac{\partial^2 E}{\partial t^2} = \frac{1}{\epsilon_0 c^2}\frac{\partial^2 P^{NL}}{\partial t^2}, \tag{2.6}$$

and the acoustic wave equation [68]

$$\frac{\partial^2 \rho}{\partial t^2} - (v^2 + \Gamma\frac{\partial}{\partial t})\nabla^2\rho = \nabla\cdot\overrightarrow{f}, \tag{2.7}$$

where Γ is a damping parameter. The driving source is the divergence of the force per unit volume $\overrightarrow{f} = \nabla p_{st}$, where p_{st} is the pressure. In the case of electrostriction, p_{st} is determined by the optical field E given by [68]

$$p_{st} = -\frac{1}{2}\epsilon_0\gamma_e\overline{E^2}, \tag{2.8}$$

where γ_e is the electrostriction constant and $\overline{E^2}$ represents the averaged value of E^2 over time.

On the other hand, the nonlinear polarization P^{NL} in Eq. (2.6) is determined by the density variation ρ, given by

$$P^{NL} = \epsilon_0 \delta\chi E = \epsilon_0 \rho_0^{-1} \gamma_e \rho E, \tag{2.9}$$

where ρ_0 is the background material density.

Using the density variation expression and inserting into the nonlinear polarization equation, we obtain the coupling equations that describe the evolution of the optical and acoustic fields, which are given by

$$\nabla^2 E - \frac{n^2}{c^2}\frac{\partial^2 E}{\partial t^2} = \frac{\gamma_e}{c^2 \rho_0}\frac{\partial^2(\rho E)}{\partial t^2} \tag{2.10}$$

$$\frac{\partial^2 \rho}{\partial t^2} - (v^2 + \Gamma\frac{\partial}{\partial t})\nabla^2 \rho = -\frac{1}{2}\epsilon_0 \gamma_e \nabla^2(\overline{E^2}), \tag{2.11}$$

The optical and acoustic fields can be solved from these equations with boundary conditions. I next solve for the backward SBS resonances using the coupled equations. More discussions on forward SBS is given in Ch. 7.

2.2.4 Single-lined SBS resonance

Now consider the case for a monochromatic pump beam E_p and counter-propagating monochromatic probe beam E_s, coupling with a single-frequency acoustic wave ρ (frequency $\Omega = \omega_p - \omega_s$,wavevector q), as shown in Fig. 2.5.

The optical field E is given by

$$E(z,t) = E_p + E_s = A_p e^{i(-\omega_p t + k_p z)} + A_s e^{i(-\omega_s t - k_s z)} + c.c., \tag{2.12}$$

and the acoustic field given in term of the material density variation ρ is given by

$$\rho(z,t) = \rho_0 + [\rho e^{i(-\Omega t + qz)} + c.c.]. \tag{2.13}$$

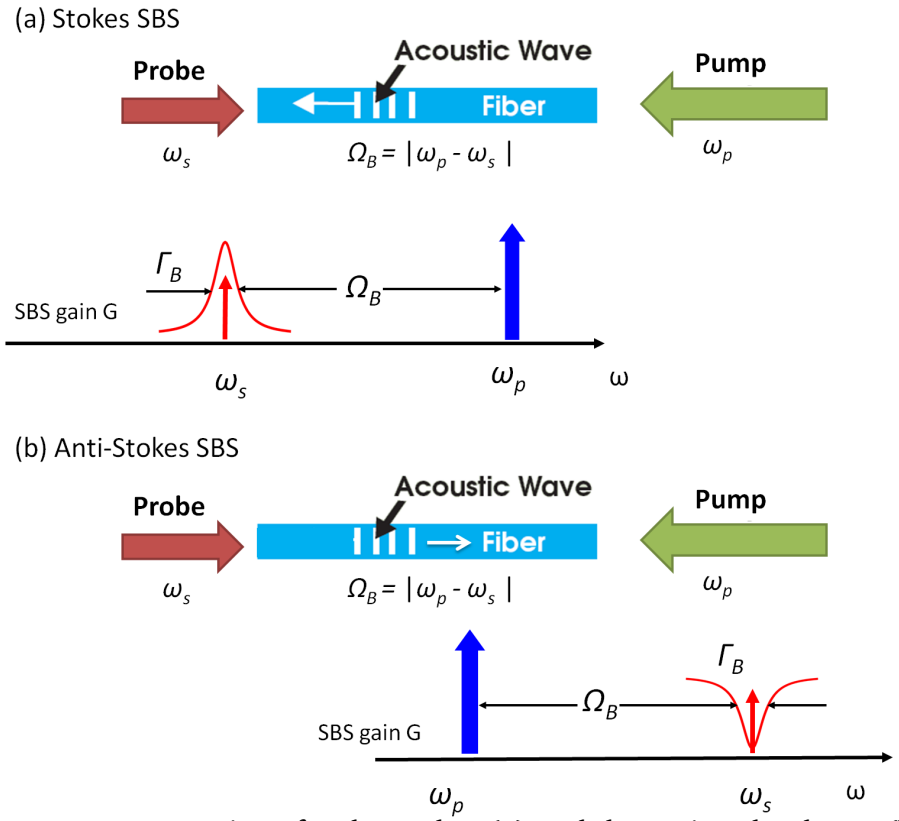

FIGURE 2.4: SBS gain G for the Stokes (a) and the anti-Stokes beam (b)

Inserting the expression of E into Eq. (2.8), and only keeping the beat term with the correct frequency Ω, the source term on the right side of Eq. (2.7) is thus given by

$$\nabla \cdot \overrightarrow{f} = \epsilon \gamma_e q^2 [A_p A_s^* e^{i(qz-\Omega t)} + c.c.]. \tag{2.14}$$

Inserting Eqs. (2.13) and (2.14) into the acoustic wave equation (2.7), we obtain

$$-2i\Omega \frac{\partial \rho}{\partial t} + (\Omega_B^2 - \Omega^2 - i\Omega\Gamma_B)\rho - 2iqv^2 \frac{\partial \rho}{\partial z} = \epsilon_0 \gamma_e q^2 A_p A_s^*, \tag{2.15}$$

where the acoustic amplitude is assumed to be slowly varying, $\Gamma_B = q^2\Gamma$ is the Brillouin linewidth, the inverse of the phonon lifetime.

This equation is greatly simplified when the propagation of phonons is ignored. In conventional optical fibers, the damping of acoustic phonons are indeed very strong and acoustic vibrations only affect optical fields locally [19]. Therefore it is legitimate

to drop terms with $\partial\rho/\partial z$. Furthermore, considering the steady-state situation by dropping term with $\partial\rho/\partial t$ as well, the acoustic field is obtained that

$$\rho(z,t) = \epsilon\gamma_e q^2 \frac{A_p A_s^*}{\Omega_B^2 - \Omega^2 - i\Omega\Gamma_B}. \tag{2.16}$$

We further use the slowly-varying assumption for the optical amplitude, i.e, the envelope of the optical wave A_p and A_s vary slowly in time and space compared to a period or wavelength. Inserting Eq. (2.16) into the right side of Eq. (2.10), we obtain coupled equations for the amplitudes of the optical beams

$$\frac{\partial A_p}{\partial z} + \frac{n}{c}\frac{\partial A_p}{\partial t} = \frac{i}{2}\tilde{g} I_s A_p, \tag{2.17}$$

$$-\frac{\partial A_s}{\partial z} + \frac{n}{c}\frac{\partial A_s}{\partial t} = \frac{i}{2}\tilde{g} I_p A_s, \tag{2.18}$$

where the beam intensity is defined as $I_i = 2n\epsilon_0 nc|A_i|^2$ $(i = s, p)$ and

$$\tilde{g} = \frac{-i\omega q^2\gamma_e^2}{2n^2c^2\rho_0}\frac{1}{\Omega_B^2 - \Omega^2 - i\Omega\Gamma_B} \tag{2.19}$$

is the SBS complex gain factor with $g_0 = \gamma_e^2\omega^2/nvc^3\rho_0\Gamma_B$. The expression is simplified to

$$\tilde{g} = \frac{g_0}{1 - 2i\delta\omega/\Gamma_B} \tag{2.20}$$

when the detuning, $\delta\omega = -\omega_s + \omega_p - \Omega_B$, is much smaller than the bandwidth Γ_B. A similar derivation is also applied to the anti-Stokes SBS at the detuning $\delta\omega = \omega_s - \omega_p - \Omega_B$. In this case

$$\tilde{g} = -\frac{g_0}{1 - 2i\delta\omega/\Gamma_B} \tag{2.21}$$

In the case where the pump beam is strong with little power transferred to the signal beam, I_p is considered as a constant. This is called the non-depleted pump assumption. The solution to Eq. (2.17) is given by

$$A_s(z) = A_s(0)e^{(ik_0+\tilde{g}I_p/2)z}, \tag{2.22}$$

where $k_0 = n\omega/c$ is the back ground wavevector. We can define the SBS wavevector $K = k_0 - i\tilde{g}I_p/2$ so that

$$A_s(z) = A_s(0)e^{iKz}, \tag{2.23}$$

where it is straightforward to see that the optical properties of the waveguide experienced by the probe beam is modified as a result of the SBS process. The physics interpretation of the SBS wavevector K will be discussed in detail in Section 2.3.

2.2.5 Coupled intensity equations

Note that the coupled equations Eq. (2.17) contains no explicit phase term. We can therefore separate the phase and intensity evolution. Most of the time, the intensity is the quantity being measured in the experiment and we can obtain the evolution of intensity alone. Substitute amplitude with intensity in Eq. (2.17), assuming slowly-varying quantities, the intensity coupled equations are given by

$$\frac{dI_p}{dz} = gI_pI_s \tag{2.24}$$

$$\frac{dI_s}{dz} = gI_pI_s, \tag{2.25}$$

where g is the real part of the SBS gain factor $\tilde{g}$ given by

$$g = g_0\frac{1}{1+(2\delta\omega/\Gamma_B)^2}. \tag{2.26}$$

Using the assumption of an undepleted pump beam, the intensity of the pump beam is considered constant and the solution for the probe beam is given by

$$I_s(z) = I_s(0)e^G, \tag{2.27}$$

where $G = gI_p z$ is the SBS intensity gain. This is a gain resonance with a Lorentzian profile, bandwidth of the resonance is Γ_B, which is full width at half maxima (FWHM). A probe Stokes beam injected at one end of the fiber will experience exponential intensity growth as it propagates through the waveguide, shown in Fig. 2.4(a).

The derivation is also valid for an anti-Stokes probe beam, if we flip ω_s with ω_p. In this case, the probe beam will experience exponential decay as it propagates through the waveguide

$$I_s(z) = I_s(0)e^G, \tag{2.28}$$

where $G = -gI_p z$. The probe beam is attenuated as it propagates through the fiber, shown in Fig. 2.4(b).

The intensity equations given by Eq. (2.24) and the real gain coefficient g are usually used to describe SBS processes where only the optical intensity is of interest. However, as discussed later in the thesis, it is sometimes also important to look into the phase evolution of the probe beam. It is therefore desired to use the amplitude evolution equations given by Eq. (2.17) and the SBS wavevector K with both real and imagery part for a full description of the SBS process.

2.2.6 SBS with multiple-line and distributed broadband pump beam

Now consider pump beams with more than one frequency components in the backward SBS process. Let's first consider two pump beams with frequency ω_{p1} and ω_{p2} coupled to a counter-propagating probe beam ω_s at the Stokes frequency, according to Eq. (2.16). The interaction gives rise to density variations with frequencies $\Omega_1 = \omega_{p1} - \omega_s$ and $\Omega_2 = \omega_{p2} - \omega_s$, which are generated due to beating between the pump and probe beams. However, since the two pump beams are propagating in the same direction, the fast propagating beat signal between the two pump beams does not match the phase for the acoustic wave, and thereby does not contribute to the SBS process. Note this is not true for the forward SBS case, as discussed in Ch. 7. The

amplitude evolution equation of the probe beam is therefore given by

$$-\frac{\partial A_s}{\partial z}+\frac{n}{c}\frac{\partial A_s}{\partial t}=\frac{i}{2}\tilde{g}_1 I_{p1}A_s+\frac{i}{2}\tilde{g}_2 I_{p2}A_s, \tag{2.29}$$

where

$$\tilde{g}_j=-\frac{g_0}{1-2i(\Omega_j-\Omega_B)/\Gamma_B},\ j=1,2. \tag{2.30}$$

The solution to Eq. (2.29) is

$$A_s(z)=A_s(0)e^{ik_0 z+(\tilde{g}_1 I_{p1}+\tilde{g}_2 I_{p2})z}. \tag{2.31}$$

This conclusion is easily extended to the situation of N pump beams with discrete different frequency $\omega_{p1},\omega_{p2}\cdots\omega_{pN}$, where

$$A_s(z)=A_s(0)e^{ik_0 z+\sum_j^N(\tilde{g}_j I_{pj})z}. \tag{2.32}$$

The SBS wavevector is given by $K=k_0-i\sum_j^N(\tilde{g}_j I_{pj})$.

We further extend this result to a broadband pump beam with continuous frequency distribution $I_p=\int \iota_p(\omega_p)d\omega_p$. In this case, the summation is substituted by an integral

$$A_s(z)=A_s(0)e^{i(k_0-i\tilde{g}\otimes i_p)z}, \tag{2.33}$$

where $\otimes$ is the convolution operator. The SBS wavevector is given by $K=k_0-i\tilde{g}\otimes\iota_p$. This allows us to engineer the SBS wavevector K by tailoring the spectrum of the pump beam. We will see this technique applied to SBS-based broadband slow light and group velocity dispersion in Chs. 3 and 4 and Ch. 5, respectively.

2.3 Physics interpretation of the SBS wavevector K

2.3.1 Imaginary and real part of wavevector K

The expression for the probe beam $E(z)$ given by Eq. (2.23) shows that we can interpret the effect of SBS as a change of optical properties experienced by the probe beam.

The result is a modified wavevector K, given by

$$K = k_0 + \frac{-ig_0 I_p/2}{1 - 2i\delta\omega/\Gamma_B}. \tag{2.34}$$

To study the optical properties of the SBS modified materials, we first separate the real and the imagery part of the wavevector as

$$\begin{aligned} K &= k_0 + k^r - ik^i \\ &= k_0 + \frac{g_0 I_p}{2}\left[\frac{2\delta\omega/\Gamma_B}{1 + (2\delta\omega/\Gamma_B)^2} + \frac{-i}{1 + (2\delta\omega/\Gamma_B)^2}\right] \end{aligned} \tag{2.35}$$

The imaginary part $k^i = gI_p/2$ is responsible for the intensity gain and/or absorption, as discussed in Sec. 2.2.5. It has a Lorentzian profile with resonance full-width at half-maxima Γ_B. The SBS intensity gain G is obtained by $G = gI_pL$. The profile of G for a single-lined SBS is shown in Fig 2.5(a).

The real part k^r modifies the refractive index of the optical fiber and is responsible for phase modulation of the probe beam. The modified refractive index n is given by $n = 1 + k^r/k_0$. The profile of n for a single-lined SBS is shown in Fig. 2.5(b).

The real and imaginary parts of the SBS wavevector K are interdependent on each other by the Kramers-Kronig relations [68]. As a result, the associated SBS refractive index and SBS gain profiles are also interdependent. While we make use of one part of K for desired optical functions, we should not forget to consider and minimize the side effect coming from the other part of K. A good engineering design of an SBS optical material must consider the optimization of both the real and imaginary parts of K.

2.3.2 Group velocity and group velocity dispersion

In the following chapters, I will discuss two interesting SBS materials. One has very large group refractive index and demonstrate slow light effect, while the other has

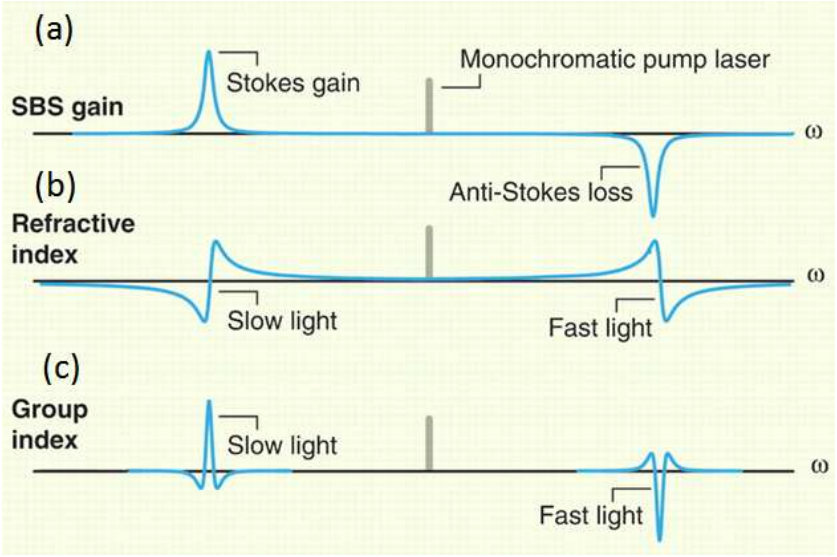

FIGURE 2.5: SBS resonance for a monochromatic pump laser in an optical fiber. Taken from Fig. 1 in [4]. (a) SBS gain G, (b) refractive index n and (c) group index n_g as functions of the frequency in SBS Stokes and anti-Stokes resonances. The spectral location of the pump beam is also shown.

very large group velocity dispersion. The concepts of group index and group velocity dispersion come from expanding the wavevector in term in a Taylor series about the central signal frequency ω_0 [19]:

$$K(\omega_s) = \beta_0 + \beta_1(\omega_s - \omega_0) + \frac{1}{2}\beta_2(\omega_s - \omega_0)^2 + \cdots, \tag{2.36}$$

where

$$\beta_i = \frac{d^j\beta}{d\omega_s^j}|_{\omega_s-\omega_0=0},\ (j = 0, 1, 2\ldots). \tag{2.37}$$

For materials that are essentially transparent so that K is pure real, the parameters β_1 is the inverse of group velocity v_g and is related to the group index n_g by

$$\begin{aligned}\beta_1 &= \frac{1}{v_g} = \frac{n_g}{c} \\ &= \frac{1}{c}(n + \omega\frac{dn}{d\omega}).\end{aligned} \tag{2.38}$$

The profile of the group index for a single-lined SBS resonance is seen in Fig. 2.5(c).

Similarly, the parameter β_2, is the group velocity dispersion (GVD) parameter. It represents the dispersion of the group velocity. The parameter β_3 is called the 3rd order dispersion parameter and so on.

The parameters β_1 and β_2 have important physical meanings. β_1 determines the group velocity at which the envelope of an optical pulse propagates. By manipulating β_1 through the SBS process, group velocities can be made very small, and hence the effect of slow-light can be obtained, to be discussed in Chs. 5 and 6. On the other hand, β_2 determines the group velocity dispersion, which broadens an optical pulse by relocating its frequency components linearly in the temporal domain. Similarly, by tailoring the SBS resonance, I can obtain very large β_2, resulting in large chirping of optical pulses, to be discussed in Ch. 5. The theoretic framework provided in this chapter lays foundations for the pursuit of extreme optical properties enabled by the SBS modified materials.

3

Broadband SBS slow light

From this chapter onward I move into the application of SBS in optical fibers. I use SBS resonances to modulate the refractive index of the optical fiber that enables applications such as slow light and large group velocity dispersion (GVD). Particularly, the novel technique of arbitrary SBS resonance tailoring is introduced and used to obtain an optimized performance under each particular circumstance.

In Chs. 3 and 4, I demonstrate a 5-GHz-bandwidth slow-light optical buffer based on stimulated Brillouin scattering. In particular, I present my arbitrary SBS resonance tailoring technique based on fast noise modulation. This novel method is compared with a previously used slow periodic modulation method. Using both methods, I obtain a flat-topped SBS gain profile with a bandwidth of 5 GHz. I use the broadband SBS slow light system to buffer a 2.5-GHz data sequence and demonstrate a tunable delay up to one pulse-width. The fast noise method is shown to substantially improve the signal date fidelity by generating a much more stable output. It should be noted that the SBS profile reshaping technique presented in these two chapters is not restricted to applications of broadband slow light, but can be easily extended to other

SBS applications such as broadband GVD (to be discussed in Ch. 5).

3.1 Introduction to broadband SBS

In SBS slow/fast light experiments, the bandwidth of the device is determined by the linewidth of the resonance. In Ch. 2, I discussed using a broadband pump beam to broaden the SBS linewidth. In addition to the broadening of the spectral linewidth of the SBS resonance, it is also found that a judicious choice of the SBS gain profile results in better delay performance for the broadband SBS slow light systems [8, 9, 18, 42]. The optimal gain profile, which improves the pulse delay under constraints of pulse distortion and pump power, is a flat-top gain spectrum with sharp edges [8, 9, 18, 42]. To obtain such an optimized gain profile, we need a technique to arbitrarily control the profile of the SBS resonance.

In this chapter, I use a periodic current modulation method to design a 5-GHz flat-topped SBS gain profile. The parameters of the modulation function are optimized by correcting for non-ideal features in the resulting spectrum based on an iterative method, which enables arbitrary control over the diode laser spectrum. The method is introduced by Dr. Edu Cabrera-Granado in reference [18]. Based on his method and experiment design, I set up the 5-GHz slow light experiment using a highly-nonlinear fiber. The data collection and analysis presented in this chapter have been conducted by me under Professor Gauthier's supervision. Professor Gauthier and I summarized the findings in reference [9].

The next section presents the theory for broadband SBS slow light with the optimized rectangular-shape gain profile. Section 3.3 gives details of the modulation function optimization. Section 3.4 shows the 5-GHz broadband SBS slow light experiment implemented in a standard highly-nonlinear optical fiber. A 200-ps-long super-Gaussian pulse is delayed with a fractional delay up with one pulse width. Conclusions

are given in Sec. 3.5

3.2 Theory of broadband SBS slowlight

3.2.1 Slow light with a single-lined SBS gain resonance

In a SBS slow light device, an optical pulse (the signal) is delayed by interacting with a counterpropagating broadband pump beam via the SBS process. The SBS interaction generates a gain resonance for the signal beam. This gives rise to a variation in the refractive index within a narrow frequency range around the resonance frequency, resulting in a small v_g for the signal beam.

As discussed in Chap 2, the complex refractive index of an optical fiber is changed by the SBS interaction. A weak signal laser beam (frequency ω_s) propagating in a SBS waveguide has an effective complex wavevector K given by

$$K(\omega_s) = k_0 + \frac{-ig_0 I_p/2}{1 - 2i\delta\omega/\Gamma_B}, \tag{3.1}$$

when interacting with a single frequency pump beam of intensity I_p. Here, $\delta\omega = -\omega_s + \omega_p - \Omega_B$ is the frequency detuning and g_0 is the line center SBS gain factor (a constant determined by the material). The refractive index is associated with the real part of the wavevector by $n = Re(K)/k_s$, and the imaginary part of the wavevector gives the SBS gain profile $g = -Im(K)$.

We use the group index n_g to characterize the propagation of temporal profiles of optical pulses, given by

$$n_g = n + \omega_s \frac{dn}{d\omega_s}, \tag{3.2}$$

where n is the refractive index, ω_s is the carrier frequency of the optical pulse (in rad/s) and c is the speed of light in vacuum. The group velocity at which the optical pulse propagates is related to the group index n_g by $v_g = c/n_g$.

The group index n_g is obtained by taking the derivative of the real part of wavevector K evaluated at $\delta\omega = 0$, given by [19]

$$n_g(\omega_s) = c\frac{dRe(K)}{d\omega_s}|_{\delta\omega=0}, \tag{3.3}$$

$$n_{g0}(\omega_s) = c\frac{dRe(k_0)}{d\omega_s}|_{\delta\omega=0},$$

where n_{g0} is the material group refractive index without the SBS process. For a single-frequency pump laser beam, inserting Eq. 3.1 into Eq. 3.3, the group refractive index is given by [17]

$$n_g(\omega_s) = n_{g0} + \frac{cg_0I_p}{\Gamma_B}\frac{1-4\delta\omega^2/\Gamma_B^2}{(1+4\delta\omega^2/\Gamma_B^2)^2}.$$

A maximum value of $n_g = n_{g0} + cg_0I_p/\Gamma_B$ is obtained on resonance ($\delta\omega = 0$), corresponding to a minimum group velocity $v_g = c/(n_{g0} + cg_0I_p/\Gamma_B)$ for the signal pulse propagation.

Consider a signal optical pulse propagating through a fiber of length L. The transit time, T_g is approximately given by [17, 70]

$$T_g = \frac{L}{v_g} = \frac{Ln_g}{c}. \tag{3.4}$$

The delay time, T_d in a slow light system is defined as the difference between the transit times through the medium with and without the slow light effect,

$$T_d = T_g - T_{g0} = \frac{L}{c}(n_g - n_{g0}), \tag{3.5}$$

where n_g and n_{g0} are the group indices with and without the slow light effect, respectively. The fractional delay τ_d is defined as the ratio of the delay time to the pulse width, given by $\tau_d = T_d/t_0$.

For a single-lined SBS gain resonance, the delay is given by

$$T_d = g_0 I_p L/\Gamma_B = G_0/\Gamma_B, \tag{3.6}$$

for an on-resonance signal pulse whose spectral width is narrower than Γ_B. Here G_0 is the center SBS intensity gain.

I next calculate the delay an optical pulse in the slow light system using an optimized rectangular-shaped SBS resonance profile.

3.2.2 Broadband slow light using a rectangular-shaped SBS resonance profile

In our broadband SBS slow light experiment, a current-modulated distributed feedback laser (DFB) is used to increase the linewidth of the pump beam spectrum. As discussed in Chap. 2, the broadened complex SBS wavevector $K(\omega_s)$ results from the convolution of the intrinsic complex SBS gain spectrum $\tilde{g}(\omega_s)$ with the intensity spectrum $\iota_p(\omega_p)$ of the pump beam, expressed by

$$K(\omega_s) = k_0 + \frac{-ig_0/2}{1 - 2i\delta\omega/\Gamma_B} \otimes \iota_p(\omega_p). \tag{3.7}$$

By designing the modulation function (to be discussed in detail in the next section), I obtain a rectangular-shaped pump beam spectrum $\iota_p(\omega_p)$ given by [18]

$$\iota_p(\omega_p) = \frac{I_p}{\Gamma}\text{rect}(\frac{\omega_p - \omega_{p0}}{\Gamma}), \tag{3.8}$$

where ω_{p0} is the pump center frequency, $\Gamma/2\pi = 5$ GHz is the bandwidth (FWHM) of the pump beam,

$$\text{rect}(x) = \begin{cases} 1 & |x| < 1/2 \quad (3.9a) \\ 0 & |x| > 1/2, \quad (3.9b) \end{cases}$$

and $I_p = \int i_p(\omega_p) d\omega_p$ is the intensity of the pump beam.

The complex SBS wavevector is therefore given by

$$K(\omega_s) = k_0 + i\int_{-\infty}^{\infty} \frac{(g_0 I_p/\Gamma)\cdot \mathrm{rect}[(\omega_p - \omega_{p0})/\Gamma]}{1 - i(\omega_s + \Omega_B - \omega_p)/(\Gamma_B/2)} d\omega_p. \tag{3.10}$$

The gain profile of the broadened SBS resonance is obtained from the imaginary part of the integral in Eq.(3.10) and is given by

$$g(\delta\omega) = \frac{\Gamma_B}{2\Gamma} g_0 I_p [\arctan(\frac{\delta\omega + \Gamma/2}{\Gamma_B/2}) - \arctan(\frac{\delta\omega - \Gamma/2}{\Gamma_B/2})], \tag{3.11}$$

where $\delta\omega = \omega_s + \Omega_B - \omega_{p0}$ is the signal beam detuning from the SBS resonance center. In our case $\Gamma \gg \Gamma_B$, and the profile is simplified as

$$g(\delta\omega) \approx \frac{\pi\Gamma_B}{2\Gamma} g_0 I_p \mathrm{rect}(\delta\omega/\Gamma). \tag{3.12}$$

The resonance profile is broadened to a rectangular shape with bandwidth Γ. Note that $g(\delta\omega)$ scales inversely proportional to the bandwidth Γ, so a larger input intensity I_p is required to sustain the SBS gain at larger bandwidth.

In an optical fiber of length L, the on-resonance SBS intensity gain G is given by

$$G_0 = 2g(0)L = 2\frac{\Gamma_B}{\Gamma} g_0 I_p L \arctan(\Gamma/\Gamma_B). \tag{3.13}$$

With the approximation $\Gamma \gg \Gamma_B$, the expression is simplified to

$$G_0 \approx \frac{\pi\Gamma_B}{\Gamma} g_0 I_p L. \tag{3.14}$$

The refractive index n associated with the SBS process is obtained by taking the real part of Eq. (3.10),

$$n(\delta\omega) = n_0 + \frac{c}{\omega_s}\frac{\Gamma_B}{2\Gamma} g_0 I_p \ln\frac{1 + [(\delta\omega + \Gamma/2)/(\Gamma_B/2)]^2}{1 + [(\delta\omega - \Gamma/2)/(\Gamma_B/2)]^2}, \tag{3.15}$$

where n_0 is the refractive index without the SBS process. The group index n_g at zero detuning ($\delta\omega = 0$) is then determined using Eq. (3.2) and Eq. (3.15)

$$n_g = n + \omega_s \frac{dn}{d\delta\omega}|_{\delta\omega=0} = n_{g0} + \frac{4c\Gamma_B}{\Gamma^2} g_0 I_p. \tag{3.16}$$

Assume that the pump intensity I_p does not change over the fiber length L. The delay time of an on-resonance signal pulse whose spectral bandwidth is much smaller than that of the broadband SBS resonance is given approximately by

$$T_d = (n_g - n)L/c = \frac{4\Gamma_B}{\pi\Gamma^2} g_0 I_p L = \frac{4}{\pi}\frac{G_0}{\Gamma}, \tag{3.17}$$

where the center SBS intensity gain G_0 in Eq. (3.14) is used.

The delay time T_d is proportional to the gain G_0 and inversely proportional to the pump spectral bandwidth Γ. As a result, we are able to control the delay time T_d by adjusting the SBS gain G_0, which is determined by the pump intensity I_p.

Note Eq. (3.17) is obtained assuming that the pump beam power I_p is constant along the fiber. There are two mechanisms that can cause a position-dependent pump intensity. One is scattering light from the pump into the signal beam, which I discuss below in the next section. The other is pump-beam absorption by the fiber or scatter of pump light out of the guided mode of the fiber. Both of these later effects can be accounted for by using the effective length $L_{\mathtt{eff}} = [1-\exp(-\alpha L)]/\alpha$ in place of length L in equations Eq. (3.13) and Eq. (3.17), where α is the attenuation coefficient.

The real and imaginary parts of the SBS wavevector are plotted in Fig 3.1, in which the rectangular-shaped SBS profile is compared with the single-line Lorentzain-shaped SBS profile. As shown in Ref. [42], the SBS gain profile that optimizes slow-light performance under various practical constraints is rectangular-shaped with sharp edges and a flat top. Such a gain profile produces longer delays and reduces pulse distortion. This is because the flat gain profile given in Eq. (3.11) enables uniform

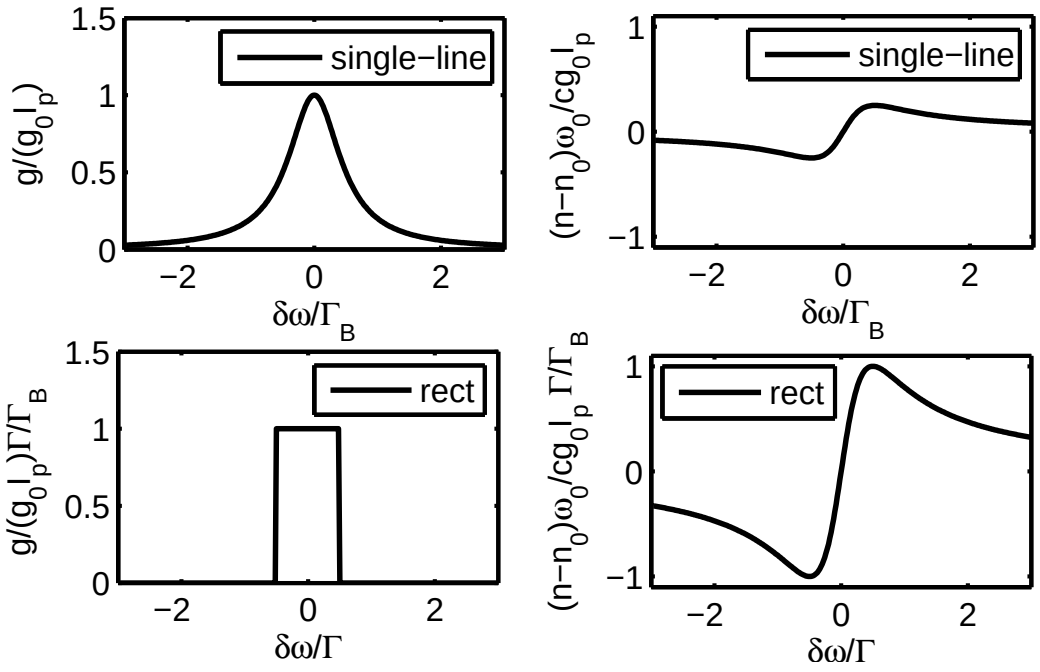

FIGURE 3.1: SBS gain profiles (right) and refractive index profiles (left) of the single-lined SBS resonance and rectangular-shaped broadband SBS resonance. The amplitude for the broadband SBS resonance is scaled by a factor of Γ/Γ_B to make an appropriate comparison between the profiles.

amplification over the different frequency components of the data stream, minimizing the filtering effect and thereby reducing pulse distortion [36]. The rectangular-shaped gain profile also improves the delay. Using the Kramers-Kronig relation, the abrupt-edged gain profile increases the phase shift, which leads to a larger group index and longer delays [40]. Indeed, this is shown in Fig 3.1 in that the slope of the refractive index profile is steeper in the rectangular shaped broadband case. By comparing the delay given in Eq. (3.6) and Eq. (3.17), we also see that the delay-bandwidth product is increased in the broadband case, enabling improved pulse delay performance.

3.2.3 Limitation due to SBS gain saturation

The delays given in Eq. (3.6) and Eq. (3.17) are proportional to SBS intensity gain G_0, which is in turn proportional to the pump intensity. Therefore, an SBS slow light

device can control the propagation delay time of the signal optical pulses by adjusting the pump intensity I_p. Larger I_p results in increased T_d. However, one cannot increase G_0 forever. One limitation of the SBS slow light delay is the SBS gain saturation caused by pump depletion. This occurs when the SBS gain is so large that most of the power contained in the pump is converted into the amplified Stokes beam, leaving the pump depleted. Two different saturation processes are involved in the pump depletion. One occurs when the initial probe beam is strong; the power of amplified probe beam grows quickly and depletes the pump beam even at moderate G. The other takes place when G approaches a threshold value G_{th}, found to be $\sim$11 in single-mode fibers [69]. In this case, spontaneous Brillouin scattering from thermal fluctuations and quantum noise is amplified and becomes sufficiently large, depleting the pump power even in the absence of a probe beam. When the pump beam is depleted, the undepleted pump assumption is no longer valid. As a result, G, and thus the delay time T_d, no longer grow with increasing pump power [68, 69]. Gain saturation and competing nonlinear processes in an SBS device are discussed in details in Ch. 5.

3.3 Broadband optimal SBS gain profile design with direct current modulation

In broadband SBS slow light systems, a spectrally broadened laser is used as the pump beam. As discussed in the previous section, a rectangular-shaped pump laser spectrum with a width much greater than the Lorentzian linewidth produces the desired optimal broadband SBS gain profile. In our experiment, a modulation voltage $V(t)$ is added to the DC injection current of the DFB laser via a bias-T (input impedance = 50 Ω) to broaden the laser spectrum. Broadening of the laser's spectrum with direct current modulation has been widely used and a quantitative, semi-empirical model for the instantaneous spectral shift of the DFB laser output due to direct current modulation $i(t)$ has been established in [71]. The spectral shift $\omega_p(t)$ as a function of time is

given by

$$\omega_p(t) = a_0 i(t) - i(t) \otimes h(t), \tag{3.18}$$

where the first term on the right-hand-side of Eq. (3.18) represents the linear adiabatic chirp induced by the almost instantaneous current-related changes of the equilibrium carrier density, and a_0 is a constant coefficient; the second term describes the slower thermal chirp, which changes the frequency as a result of temperature-related changes of the refractive index and physical length of the cavity. I start from only considering the first term, where DFB frequency follows the modulation current exactly. A triangular waveform spends an equal amount of time in each voltage value, in accordance with a rectangular-shaped distribution.

I start from a 400-kHz periodic triangular waveform and set the peak to peak amplitude to 2.73 V (Fig. 3.2(a)). The slow variation period and smooth waveform ensure that the variation of voltage is slow for the DFB laser to follow, with exceptions around the turning points. As shown in Fig. 3.2(b), a roughly rectangular-shaped spectrum is obtained. However, the pump spectrum shows a clear asymmetry, which is caused by response differences during the rising and falling of temperatures and is corrected by introducing a quadratic term in the triangular waveform (Fig. 3.2(c) and (d)). We also observe peaks at the edge of the spectral profile induced by the thermal chirp at the turning points of the waveform. As a result of the thermal chirp, the instantaneous laser frequency spends more time in these regions. These peaks are corrected by introducing a current "jump" at the turning points, as shown in Fig. 3.2(e) and (f). The final modulation waveform is expressed as

$$V(t) = \nu_{\max}/2 \times \begin{cases} at^2 + (4/T - aT/4)t & \text{if} \quad t < T/4 \\ at^2 - (4/T + a3T/4)t + 2 + (2aT^2)/4^2 & \text{if} \quad T/4 < t \leq 3T/4 \\ at^2 + (4/T - a9T/4)t + (5aT^2)/4 - 4 & \text{if} \quad 3T/4 < t \leq T. \end{cases}$$

I obtain the best parameter values for an optimal pump spectrum by applying

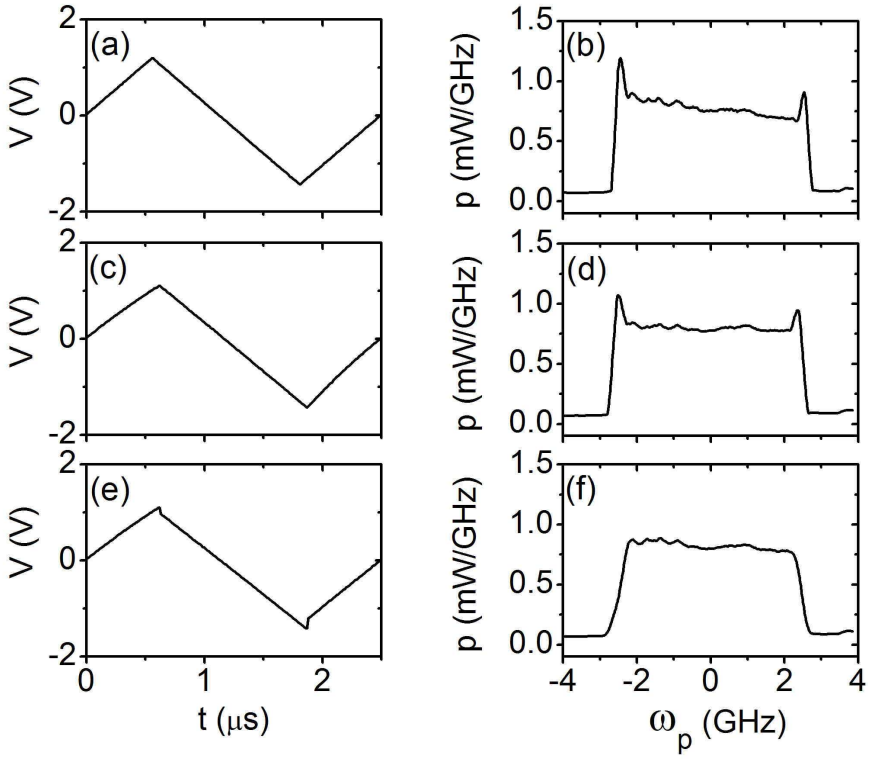

FIGURE 3.2: Pump spectral distribution optimization procedure for the case of slow modulation. Modulation waveform $V(t)$ (left column) and measured pump spectrum profile $p(\omega_p)$ (right column) are shown for triangular modulation (upper row), with the addition of a small quadratic term (middle row), and for the optimum waveform (lower row). The DC injection current is 110 mA.

an iterative scheme. As I change the parameters in small steps, the pump spectrum is recorded and compared to an optimal flat-top spectrum. The error (root mean square deviation RMSD) is calculated at each step. After a small number of iterations, I minimize the error using a steepest descent search procedure, which gives us the optimal values $v_{\max} = 2.73$ V, and $a = -30.4\ \mu s^{-2}$. The RMSD for the optimal spectral profile is 0.069 mW/GHz (Fig. 3.2(f)), compared to 0.083 mW/GHz for Fig. 3.2(b) and 0.081 mW/GHz for Fig. 3.2(d).

I then measure the SBS gain profiles produced by the spectral broadened pump beam using the current modulation waveforms depicted in Fig. 3.2(e). The experimental setup is shown in Fig. 3.3. To independently measure the SBS gain profile, I

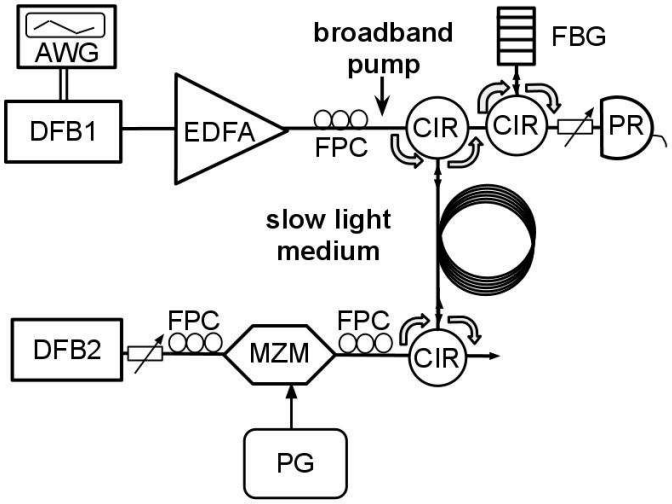

FIGURE 3.3: Experiment setup. Spectrally broadened pump and signal beams counter-propagate in the 2-km-long slow light medium (HNLF, OFS Inc.), where they interact via the SBS process. The SBS frequency shift in HNLF is 9.62 GHz. A fiber Bragg grating (FBG, bandwidth 0.1 nm) is used to filter out the Rayleigh backscattering of the pump beam from the amplified and delayed signal pulse sequence before detection. AWG: arbitrary function generator (Tektronix AFG3251), DFB1: 1550-nm DFB laser diode (Sumitomo Electric, STL4416), EDFA: erbium doped fiber amplifier (IPG Photonics EAD 1K), DFB2: 1550-n DFB laser diode (Fitel FOL15DCWC), MZM: Mach-Zehnder Modulator, PG: electronic signal pattern generator, PR: 12 GHz photo-receiver (New Focus 1544b), FPC: fiber polarization controllers, CIR: optical circulator.

use a weak unmodulated monochromatic signal beam (input power P_{s0}), and record the amplified signal beam power P_s at the photoreceiver as I slowly scan the frequency of the signal beam. The SBS intensity gain G is obtained by

$$G = \ln(P_s/P_{s0}). \tag{3.19}$$

The SBS intensity gain G is related to $g(\omega_s)$ by $G(\omega_s) = g(\omega_s)L_{\mathtt{eff}}$, where $L_{\mathtt{eff}} = (1 - e^{-\alpha L})/\alpha = 1.64$ km is the effective length of the fiber, L (= 2 km) is the physical length of the fiber and α (= 0.9 dB/km) is the attenuation coefficient. The pump beam is characterized by its power P_p instead of intensity I_p in the experiment. The power and intensity are related by $P_p = I_p A_{\mathtt{eff}}$, where $A_{\mathtt{eff}} = 11.7\ \mu\text{m}^2$ is the mode area of the highly nonlinear fiber.

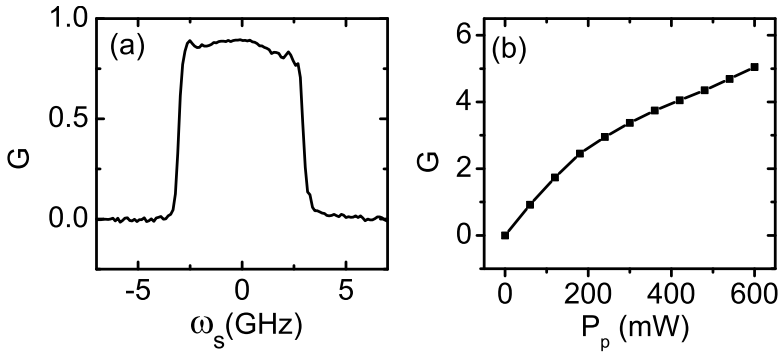

FIGURE 3.4: (a) SBS gain profile at $P_p = 70$ mW. (b) SBS gain saturation.

Figure 3.4(a) shows the measured SBS gain G profiles for the periodic modulation method. As discussed previously, the SBS gain profile is the convolution of the pump spectrum with the intrinsic narrow Lorentzian lineshape. In our case where the pump spectrum bandwidth (5 GHz) is much larger than the narrow Lorentzain linewidth ($\sim$52 MHz in HNLF), the resultant SBS gain profile is similar to the pump spectrum, as seen in Fig. 3.4(a).

I next measure the gain saturation behavior for the broadband SBS resonance. A continuous-wave signal beam ($P_{s0} = 48$ μW) is tuned to the SBS resonance to measure the line center SBS gain G at different pump powers. Again, G is obtained from Eq. (3.19). As shown in Fig. 3.4(b), G grows linearly with respect to the pump power P_p when P_p is low. Saturation takes place when the SBS gain G is large enough so that a great portion of the power in the pump beam is transferred into the signal beam, and the exponential amplification of the signal beam cannot be sustained [68]. As P_p increases, we see that gain starts to saturate around $G = 3$. This saturation threshold is significantly smaller than that of the single-lined SBS. In the next section I will discuss how irregularities in the slow periodic current modulation affect the saturation threshold.

3.4 Slow-light performance

I now measure the delay of a signal optical pulse in the broadband SBS slow light device. I use the 5-GHz broadband SBS slow light system to delay a single super-Gaussian shaped optical pulse (shown in Fig 3.5(b)). The pulse width is set to 200 ps to match the bandwidth of the device. The signal pulse is first generated electrically via a pattern generator and then encoded on the signal beam via the 10-GHz Mach-Zehnder Modulator (MZM). I use a weak signal seed laser beam (power $P_{s0} = 12\ \mu$W) and restrict $P_p < 500$ mW. After propagating through the fiber, the delayed and amplified signal beam is detected by a 12-GHz photoreceiver and recorded on an 8-GHz digital oscilloscope (Agilent DSO80804B). Slow light performance is characterized by measuring the delay and the temporal profile of the output signal at various pump power levels.

Figure 3.5(a) shows the measured pattern delay as a function of P_p. Because a weak signal beam is used in the measurement, the measured pattern delay goes linearly with P_p and no significant saturation is observed. The measurement result agrees well with the theoretical simulation the delay time for a rectangular-like optimized gain profile given in Eq. (3.17). A maximum delay of 199 ps is obtained at the pump power of 500 mW. In Fig. 3.5(b) we see that the delayed pulse shape is a little distorted compared with the undelayed pulse shape, which is a super-Gaussian. The re-shaped the signal pulse looks more Gaussian and we can also see small ripples behind the main pulse. This is because high frequency components beyond the 5-GHz bandwidth are suppressed by the filtering effect of the resonance profile. However, the distortions are small, with very little pulse broadening.

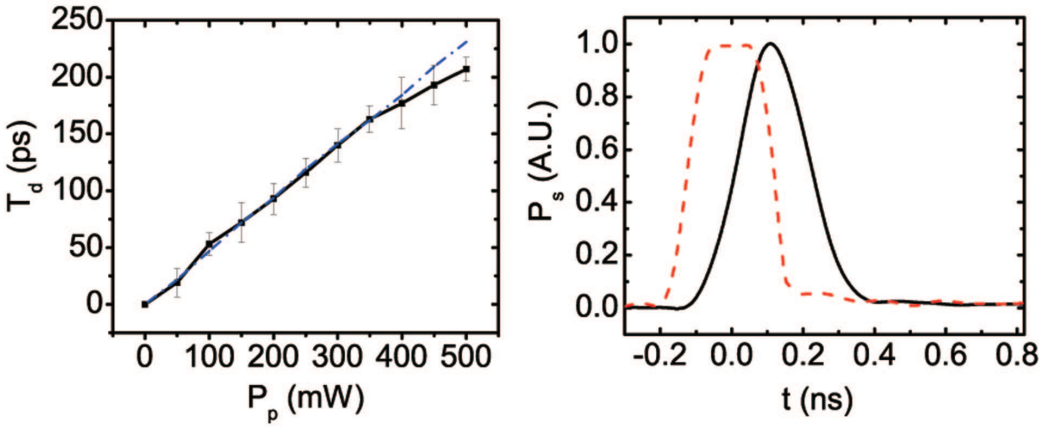

FIGURE 3.5: Slow light performance using periodic modulation method in HNLF. (a) Slow light delay as a function of P_p (black solid). The theoretically predicted delay for a rectangular-like optimized gain profile (blue dash-dot line) is also shown. SBS gain saturation is avoided using a signal data sequence with a small peak optical power $P_{s0} = 12$ μW; (b) Averaged output signal profiles at $P_p = 350$ mW for a single pulse (black solid line), together with the undelayed pulse profile at $P_p = 0$ mW (red dashed line) in HNLF. The delayed pulse is more Gaussian-shaped but without significant broadening. The amplitude of the pulses is normalized as a percentage of the peak pulse height.

3.5 Conclusion

I have presented the theory and experiment of a broadband SBS slow light device. A current modulation function is obtained using an iterative method to generate an optimized rectangular-shaped SBS gain profile. A 5-GHz broadband SBS slow light system is built and a 200-ps-long super-Gaussian signal pulse is delayed up to one pulse width. The results presented in this chapter are only of average measurements on a single pulse. In the next chapter, I will characterize a long sequence of data passing through the slow light material in real time, which shows that the slow modulation method has substantial excess noise. I will describe a new modulation method in the next chapter that addresses the problem.

4

Fast noise modulation method in high-fidelity broadband SBS slow light

In the previous chapter, we only looked at the delay for a single pulse. Here, I pass a stream of pseudo-random data through the slow light medium, which allows us to explore pattern dependence as well as noise in the system. From analysis of this data, I find that the slow modulation method presented in the previous chapter has more pattern dependence, meaning that different signal sequences result in different delay times and amplitudes. To solve this problem, I introduce a high-fidelity broadband slow-light device pumped by a noise-current-modulated laser beam. The novel SBS tailoring technique has been developed based on noise current modulation. By using the new tailoring technique and optimizing the buffering performance using a iterative method, I significantly improved the signal fidelity in a broadband SBS slow light system. This method can be applied with any DFB laser diode to generate stable laser beams with a desired spectral profile, thus sets no restrictions to the sources.

The arbitrary SBS tailoring technique that enables device performance optimization is my key contribution to this field, and can be generalized to optimize the optical

properties of SBS-modified functional materials. The application to broadband optical buffer presented in this chapter demonstrates the typical procedure for the method.

In the experiment, I use a noise-modulation waveform with an optimized pseudo-random distribution to obtain an optimal flat-topped gain profile. In comparison with the previous slow-modulation method presented in Ch. 3, eye-diagram and signal-to-noise ratio (SNR) analysis shows that this broadband slow-light technique significantly increases the fidelity of a delayed data sequence, while maintaining the delay performance. A fractional delay of 0.81 with an eye opening (EO) of 0.5 and an SNR of 5.2 is achieved at the pump power of 350 mW using a 2-km-long highly nonlinear fiber with the fast noise-modulation method. This results in a 50% increase in eye-opening and a 36% increase in SNR compared to the slow modulation technique.

The idea of noise modulation was conceived by me and Professor Gauthier. I set up the experiment and collected the data. In cooperation with Dr. Myungjun Lee, Dr. Michael Gehm and Prof. Mark Neifeld, we develop the theoretical model for the system and compared it with the data analysis. In particular, Professor Gauthier and Dr. Lee has developed the noise model and eye pattern simulation. The channel capacity analysis has been completed by Dr. Myungjun Lee and Prof. Neifeld. We summarize the results presented in this chapter in the paper[9]. A more detailed noise model and channel capacity performance analysis for a large range of parameters have been summarized in the paper [73].

4.1 Noise modulation method

Most previously reported broadband SBS slow light experiments control the spectral SBS gain profile by direct modulation of the pump laser using a periodic modulation waveform [8, 18, 40]. The frequency of the waveform is typically chosen to be in the sub-MHz range so that detailed features of the waveform can be reproduced faithfully

using an arbitrary waveform generator. However, such periodic modulation results in an intermittent interaction with the signal beam, which may induce signal fluctuations. Previous research that focused on averaged pulse delay was not affected by these fluctuations because they were averaged out. Nevertheless, these low-frequency fluctuations reduces the signal-to-noise ratio (SNR) of a delayed pseudo-random data sequence and degrades fidelity of the device.

To build an optimal high-fidelity broadband SBS slow light system, I develop a systematic procedure to generate a broadband flat-topped SBS gain profile with direct noise current modulation. I compare such a system to the slow periodic modulation method in Ch. 3 to experimentally demonstrate slow light performance improvement with increased modulation speed. Random noise current modulation has been used in previous research on broadband SBS slow light systems [16, 31, 41]. However, due to limited control of the spectral profile, these previous methods generally result in a Gaussian-shaped SBS gain profile. The frequency-dependent gain of a Gaussian profile causes pulse distortion at large delays. Although Yi *et al.* [41] have discussed shaping the pump spectrum by passing a noise waveform through a saturated electronic amplifier, the control over the SBS gain profile is still limited and highly sensitive to the detailed saturation characteristics of the high speed amplifier, which is often hard to characterize. Here, I present an extension of Yi's method in which the noise distribution is controlled arbitrarily. Compared to Yi's work, the method described here is superior because I have complete control over the noise waveform in a way that is easily generalized to any DFB laser used in broadband SBS slow light systems. It will be shown that, by controlling the distribution of the noise waveform, I am able to tune the shape of the SBS gain profile and obtain the best flat-topped profile that optimizes the slow light delay and reduces distortion. I also find that using a noise modulation function with a sampling rate ∼400 MHz (fast compared to the phonon lifetime (∼ 4 ns) in the fiber) substantially stabilizes the optical signal and improves

the data fidelity of the broadband SBS slow light system compared to previous slow modulation methods.

The rest of the chapter is organized as follows. Section 4.2 briefly reviews the dynamics of a distributed feedback (DFB) laser under direct current modulation and describes the procedure to obtain a flat-topped SBS gain profile with the noise modulation waveform. Section 4.3 describes and compares the delay performance for a 2.5-Gb/s return-to-zero (RZ) data sequence using these two methods (slow and fast). I also quantify transmission fidelity by eye-opening (EO) and signal-to-noise ratio measurements. Finally, our conclusions are summarized in Sec. 4.4.

4.2 Optimal SBS profile design using the fast noise modulation method

To obtain an optimized pump laser spectrum, I again start from the semi-empirical model for the frequency shift of a DFB laser with direct current modulation $i(t)$ described in Eq. (3.18)

$$\omega_p(t) = a_0 i(t) - i(t) \otimes h(t),$$

where a_0 is the instantaneous response parameter. In the previous chapter where the modulation function is slow, the thermal chirp term is not considered. However, they are important in the fast modulation method presented in this chapter. The thermal chirp is characterized by the convolution of $i(t)$ with the impulse response $h(t) = \sum a_n e^{-\tau/\tau_n}$, where the different time constants τ_n correspond to thermal conductivities of different layers in the DFB laser. Measurements of our DFB laser reveal that the dominant thermal term has a time constant as short as 7.5 ns [18]. As a result, an analysis of both the thermal and adiabatic chirp is necessary to obtain a precise design of the laser spectrum.

I start the design of the optimal SBS gain profile by only considering the linear adiabatic term in Eq. (3.18). In this case, the frequency distribution of the DFB

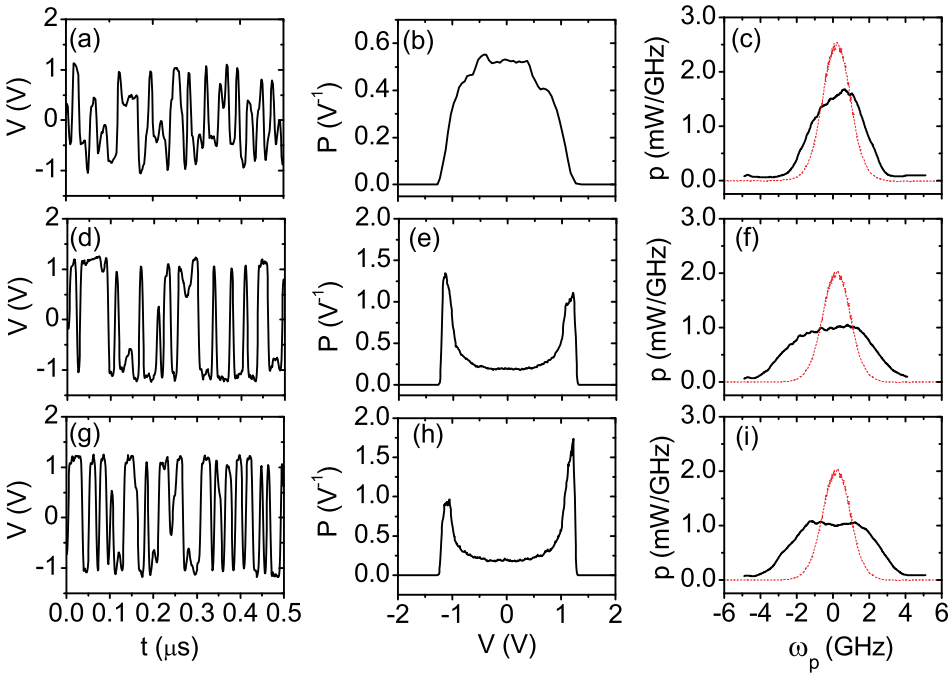

FIGURE 4.1: Pump spectral distribution optimization procedure of the fast noise modulation. Modulation voltage waveform $V(t)$ (left column), probability distribution P (bin size = 0.025 V) (middle column) and resultant pump beam spectrum $p(\omega_p)$ (right column) are shown for the flat-distributed white noise modulation $V(t) = 2.5\ \text{V}\times f(t)$, where $f(t)$ is a random variable that is approximate uniformly distributed between -0.5 and 0.5 (upper row), the bi-peak symmetric noise modulation $V(t) = 2.5\ \text{V}\times \tanh[10f(t)]$ (middle row) and the optimal noise modulation $V(t) = 2.5\ \text{V}\times \tanh[10(f(t)+0.06)]$ (bottom row). A Gaussian spectral profile resulted from a Gaussian noise modulation $V(t) = 2.5\ \text{V}\times g(t)$, where $g(t)$ is a random variable with standard normal distribution, is shown in Figs. c,f and i for comparison purposes. The DC injection current is 110 mA.

laser is the same as that of the current modulation waveform. This is true when the characteristic time scale of the modulation is faster than any of the time constants of the DFB laser. When the thermal chirp is present, the spectral distribution of the noise must be adjusted using an iterative method, as described below.

To generate the optimal rectangular-shaped pump spectrum, I use a noise waveform $V(t) = 2.5\ \text{V}\times f(t)$, in which $f(t)$ is a random variable approximately uniformly

distributed between -0.5 and 0.5 (Fig. 4.1(a)). The sampling time interval is set to 2.5 ns on an arbitrary wavefunction generator (Tektonix AFG3251). Figure 4.1(b) shows the probability distribution P of the modulation waveform as a function of the voltage V, which is determined from the histogram of the waveform. The spectrum of the pump beam $p(\omega_p)$ is measured by mixing it with a monochromatic reference beam (New Focus Vortex 6029) on a high-speed detector (New Focus Model 1544b), as shown in Fig. 4.1(c). We see that the generated pump beam spectrum shows a significant improvement compared to a Gaussian profile, but is slightly peaked in the center and shows some asymmetry.

The concentration of the spectrum in the center is due to thermal chirp. In particular, the current of the laser is fluctuating quickly, leading to fluctuations in the temperature about an equilibrium value. According to Eq. (3.18), a step change in the current $i(t)$ leads to a sudden adiabatic change in the optical frequency $\omega_p(t)$ followed by thermal induced multiple exponential decays to a stationary value. The fast noise-modulation waveform has a rise time of $\sim$ 2.5 ns, and has many abrupt changes that can be considered as instantaneous jumps (Fig.4.1(a)). After such an abrupt change, the laser spends some time returning towards the previous frequency due to the thermal chirp, which favors frequencies in the middle of the range and causes the center-concentration effect.

To compensate for this effect, I increase the probability distribution in the extrema of the noise distribution. This can be done using the nonlinear function 2.5 V$\times \tanh(bf(t))$, where b controls the distribution weights on the extrema. Figure 4.1(d)-(f) show the waveform $V(t)$, distribution probability P, and the resultant pump spectrum $p(\omega_p)$ for $b = 10$. We see that the center-concentration problem in the pump spectrum is solved, but there is still an asymmetry in the profile, as seen in Fig. 4.1(f). This asymmetric frequency response is induced by the nonlinear contribution to the adiabatic chirp (not accounted for in Eq. (3.18)) and the additional different thermal

time constants [18]. To solve this problem, an asymmetry is needed in the distribution of the modulation waveform. We use 2.5 V$\times$ tanh$[b(f(t)+c)]$, in which the parameter c controls the asymmetry of the distribution.

The best parameter values for an optimal pump spectrum are obtained by applying an iterative scheme. As I change the parameters in small steps, the pump spectrum is recorded and compared to an optimal flat-top spectrum. The error (root mean square deviation RMSD) is calculated at each step. After a small number of iterations, I minimize the error using a steepest descent search procedure, which gives us the optimal values $b = 10$ and $c = 0.06$. As shown in Fig. 4.1(i), modulation with the optimal parameters results in a flat-topped spectrum profile. The edge is smoothed due to the thermal chirp but is still reasonably steep. The RMSD of this spectral profile is 0.164 mW/GHz, compared to 0.25 mW/GHz in Fig. 4.1(c) and 0.173 mW/GHz in Fig. 4.1(f).

The generated broadband pump beam is then injected into the 2-km highly nonlinear fiber, and the SBS gain profile is measured by detecting the output of a frequency swept signal beam, as described in Sec. 3.3. The measured SBS gain profile is shown in Fig. 4.2(a), which is compared with the gain profile using the slow periodic modulation method. The fast noise-modulation waveform results in a less sharp edge in the SBS gain profile as a result of the temperature fluctuation in a nondeterministic manner. In the fast noise modulation, the temperature is affected by the previous history of the modulation and thus has wide fluctuations. On the other hand, the slow triangular-like waveform results in a deterministic value of the laser temperature at any moment. Therefore, the frequency of the laser is well-defined at the edge of the modulation waveform. Nevertheless, as shown next, the reduced slope of the edges with the fast noise modulation does not significantly affect its slow light delay.

Next, I repeat the measurement of the line center SBS gain using the fast modulation method in the 2-km highly nonlinear optical fiber. The results with the fast and

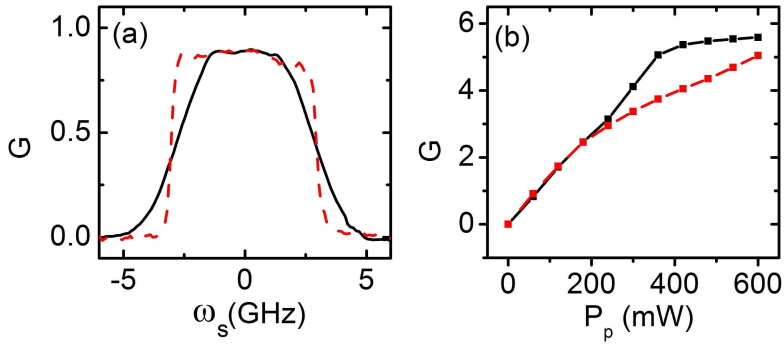

FIGURE 4.2: (a) SBS gain profiles using the fast noise modulation (black solid) and slow periodic modulation (red dashed) at $P_p = 70$ mW. Measurement taken using experimental setup in Fig. 3.3. The same cw signal beam is used in both measurements. (b) SBS gain saturation. The black solid line shows the SBS gain G using the fast noise modulation, which grows linearly with pump power P_p until saturated. The red dashed line shows the SBS gain G using the slow modulation, which starts to saturate gradually at a much smaller P_p compared to the fast modulation method.

the slow modulation methods are compared in Fig. 4.2(b). As P_p increases, we see that the slow modulation method results in an early saturation at $G \sim 3$. In contrast, fast modulation results in a hard stop of gain increase at $G \sim 5$.

While the saturation threshold is brought down significantly by the increased pump power required for broadband SBS resonances in both cases, gain saturates more quickly with slow modulation. The early saturation in the slow modulation case is likely due to fluctuations in G that are caused by the uneven frequency swept rate and the end effect. In the slow modulation method, the frequency of the pump beam is slowly swept. During the modulation period of 2.5 μs, a monochromatic signal beam is only intermittently amplified during the short time period when the pump-probe frequency difference is equal to the SBS frequency shift within the resonance linewidth. An estimate of the average interaction time period gives 52 MHz/5 GHz $\times$2.5 μs= 26 ns. On this time scale, thermal fluctuations associated with short characteristic temporal constants can significantly affect the length of the interaction time period and give rise to fluctuations in G. Moreover, since the SBS amplification pro-

cess in the slow modulation method is intermittent, there is an end effect that induces more fluctuations in G. In our experiment specifically, the frequency of the pump beam as seen by the signal beam goes through 7.76 periods of modulation during the whole propagation time ($\sim$9.7 μs). Since the number of modulation periods during the propagation time is not an integer, the signal beam can meet the resonant pump beam for either 7 or 8 times, depending on the relative time of measurement during the modulation period. As a result of both effects, the output signal beams measured at some particular times are amplified more than others, which can lead to gain saturation. Consequently, gain saturation is observed even when the average G is still small. This behavior results in the gradual early saturation seen in Fig. 4.2(b).

On the other hand, in the fast modulation experiment, a monochromatic signal is constantly amplified by the frequency-matching component in the broadband pump beam as it travels through the fiber. The pump beam frequency chirp rate potentially has jitters on a faster time scale beyond 400 MHz, but the SBS interaction cannot response to such fast processes. Moreover, the output signal amplification results from the accumulated SBS interaction through the whole fiber. Therefore, G is uniform and stable in this case. The fluctuations in G using the slow modulation method is the source of the low-frequency fluctuations that degrade the fidelity of a data waveform.

The small number of scanning periods in the 2-km-long HNLF can be increased by substantially increasing the fiber length while keeping the modulation rate fixed. By increasing the fiber length, I expect to see a reduction in fluctuations due to the end effect and more averaging along the fiber, which helps stabilize the output signal. To test this, a 20-km LEAF fiber is used in the slow light device and the signal fidelity is quantified and compared with that in the shorter HNLF. However, a much longer fiber induces increased noise from spontaneous Brillouin scattering [69, 72] and boosts SBS G saturation, because of the increased SBS gain coefficient. Moreover, the dispersion in an optical fiber increases with length, distorting the signal pulse waveform and

degrading the performance. The choice of fiber length is also limited by practical factors of cost and volume. Instead, increasing the modulation rate is much easier and more efficient.

4.3 Slow-light performance

I next compare the delay performances of the fast and slow modulation methods. I measure the delay and fidelity of the output signal when applying our 5-GHz broadband SBS slow light system to a 2^{12} bit-long return-to-zero (RZ) binary data sequence. This data sequence contains all 2^8 8-bit-long sequences separated by 8-bit 0s serving as a buffer. In this arrangement, the pattern-dependent delay is averaged. Compared to the non-RZ coding, the use of an RZ signal in our experiment is robust against pulse broadening, but takes twice as much bandwidth to achieve the same data rate. I use a signal data rate of 2.5 Gb/s to match the SBS slow light bandwidth of 5 GHz (FWHM); the width of a single pulse is equal to 200 ps. The data sequence by a pattern generator (HP70004A) and encoded on the signal beam via the 10-GHz Mach-Zehnder Modulator (MZM). I use a weak signal seed laser beam (power $P_{s0} = 12$ μW) and restrict $P_p < 500$ mW to avoid SBS gain saturation in HNLF ($P_p < 300$ mW in LEAF). After propagating through the fiber, I detect the delayed and amplified signal beam using a 12-GHz photoreceiver and recorded on an 8-GHz digital oscilloscope (Agilent DSO80804B). I evaluated the slow light performance from both fast and slow modulation methods in different fibers using the well-known fidelity metrics of EO and SNR based on the eye-diagram of the output signal at various pump power levels.

I first measure the slow light pattern delay by generating the output eye diagram [73, 74]. I determine the pattern delay by comparing the position of the maximum eye-opening with and without the pump beam. Figure 4.3(a) shows the measured pattern delay as a function of P_p with the slow and fast modulation formats respec-

tively. Because a weak signal beam is used in the measurement, the measured pattern delay scales linearly with P_p and I observe no significant saturation. Both modulation formats yield the same delay within the measurement error, which agrees well with the theoretical simulation of the delay time (Eq. (3.17)) using a rectangular-like optimized gain profile [8] (blue dotted-dash line) and using a super-Gaussian gain profile (cyan dash-double dot line). As shown in both experimental data and simulation, the reduced slope of the super-Gaussian gain profile in the fast modulation method does not significantly reduce the delay time. I also observe similar temporal profiles of the output signal pulses in Fig. 4.3(b). Shown in this figure are the averaged pulse profiles at $P_p = 350$ mW of the first "1" in the data sequence, which is an isolated pulse with many bits of "0"s before and after. We see that the delayed pulse shapes using both modulation methods are very close. Compared with the undelayed pulse shape, which is a super-Gaussian, we see that both fast and slow modulation SBS gain profiles reshape the signal pulse into a Gaussian profile. This is because high temporal frequency components beyond the 5-GHz bandwidth are cut out. Nevertheless, the distortion is small. We can also see that the fast modulation method results in a more symmetric pulse profile, while the slow modulation method produces small ripples behind the main pulse, making the overall profile asymmetric. This asymmetric pulse shape reduces the peak delay difference between the two methods. The better output pulse profile in the fast modulation method is a result of the smoother phase response with the super-Gaussian shaped gain profile. The asymmetric pulse shape associate with the slow modulation reduces the peak delay difference between the two methods, resulting in a very close delay performance observed in Fig. 4.3(a). Based on results shown in Figure 4.3(a) and (b), we see that both slow and fast modulations demonstrate similar delay and pulse distortion behaviors, allowing us a fair comparison of their fidelity performance.

Also shown in Fig. 4.3(a) is the pattern delay in the 20-km LEAF fiber using the

slow modulation method. We observe a steeper increase of delay time with P_p as a result of increased Brillouin gain coefficient in the longer fiber. The pump power, P_p, is restricted below 300 mW to avoid SBS self-oscillation.

Next, I study the signal fidelity of the slow light device. The slow light fidelity metrics are measured in terms of EO and SNR. The EO is measured by the maximum difference between the minimum value of the high level and the maximum value of the low level in the eye diagram (shown in Fig. 4.4 and Fig. 4.5). The SNR at the eye-center is defined as the ratio of the EO to the quadratic mean of the standard deviations (noise) of the high and low levels, shown in Fig. 4.4.

Figure 4.3(c) shows the EO and Fig. 4.3(d) shows the SNR as functions of P_p. Note that as I change P_p, the power of the signal beam goes through 3-4 orders of magnitude, which is beyond the dynamic range of most photoreceivers. To avoid detection saturation at $P_p = 500$ mW in HNLF ($P_p = 300$ mW in LEAF), I place an attenuator before our photoreciever. As the output signal beam is amplified with increasing P_p, the signal fidelity first increases as the signal overtakes the detector dark noise, then decreases when the SBS gain approaches saturation at high pump power, where amplified spontaneous Brillouin scattering begins to dominate [69].

Comparing the slow light performances using the fast and slow modulation methods in the HNLF fiber, we see that while both modulation methods result in similar trends for signal quality at different pump power levels, the fast noise-modulation method results in better data fidelity over all pump power levels. In particular, Fig. 4.5 shows an example of the output eye diagrams using both modulation methods at $P_p = 350$ mW, where 50% more EO is obtained using the fast modulation method. I achieve a fractional delay (ratio of the delay to the width of a single pulse) of 0.81 and an SNR of 5.2 at $P_p = 350$ mW using the fast modulation method. Compared to the slow modulation method, the fast modulation method increases the EO by 50% and SNR by 36%, demonstrating significant enhancement of data fidelity while maintain-

ing the same delay.

The SNR and EO in the 20-km LEAF fiber using the slow modulation method are also shown in Fig. 4.3 (c) and (d). We see that the trend of the fidelity curves as a function of P_p in LEAF has the similar shape to the fidelity curves in the HNLF, but the P_p level corresponding to the high fidelity peak is lower due to a larger Brillouin gain coefficient. In the small P_p ($<$ 200 mW) region, the LEAF fiber has improved fidelity compared to the HNLF fiber with the same slow modulation. In the high P_p ($>$ 200 mW) region, as a result of larger spontaneous Brillouin amplification noise, the fidelity of the signal drops down in the LEAF fiber. Overall, although the slow light performance can be improved in the small P_p region using the long LEAF fiber, a much better performance is obtained using the fast modulation method in HNLF at all P_p levels.

4.4 Conclusion

I show in this chapter the original work of designing the optical properties for an optimized broadband SBS optical buffer. The spectrum of a diode laser is controlled arbitrarily using a noise current modulation. By applying the fast noise modulation method, I tailor the SBS gain profile by controlling the distribution of the noise-modulation waveform. I obtain an optimal flat-topped gain profile using an asymmetric bi-peak-distributed noise-modulation waveform. Using this broadband SBS slow light technique, I significantly improve the signal fidelity compared to the previous slow modulation method. I obtain pattern delays up to one pulse width for a RZ data rate of 2.5 Gb/s. The high data fidelity (SNR up to 7) is the best of the time. Moreover, the experiment has demonstrated a typical procedure using the novel arbitrary SBS tailoring technique to engineer the optical prosperities of the material for optimized device performance. The iterative method used to shape the SBS resonance to

obtain best delay-bandwidth product can be applied to any SBS modified functional material design. This piece of original work has been summarized in [9].

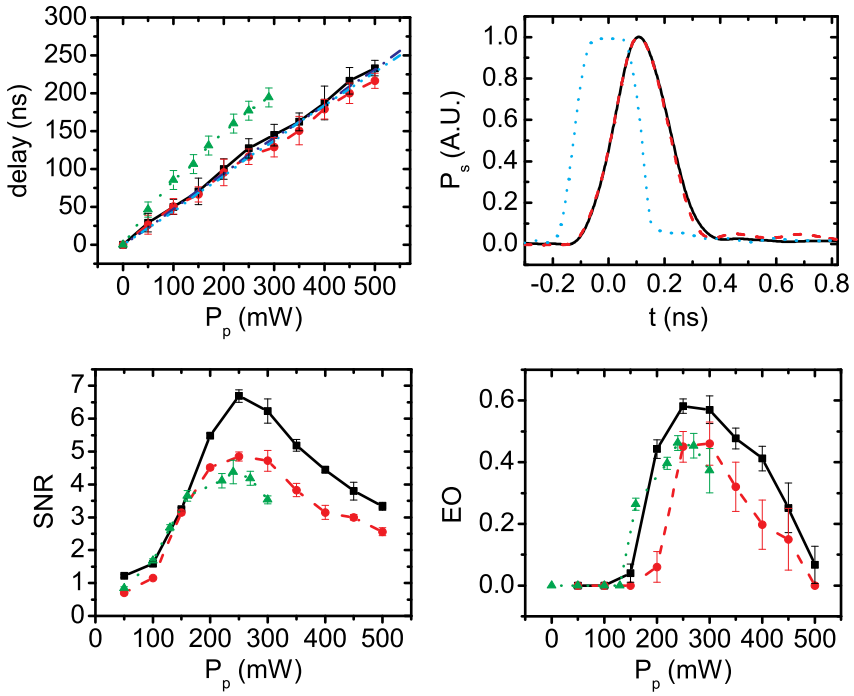

FIGURE 4.3: Slow light performance using fast (solid black line) and slow (dashed red line) modulation waveforms in HNLF, and slow modulation waveform in LEAF (dotted green line). (a) Slow light delay as a function of P_p. The theoretically predicted delay with a rectangular-like optimized gain profile (blue dash-dot line) and with a super-Gaussian gain profile (cyan dash-double dot line) in the HNLF fiber are also shown. SBS gain saturation is avoided using a signal data sequence with a small peak optical power $P_{s0} = 12$ μW; (b) Averaged output signal profiles at $P_p = 350$ mW of the first single pulse in the data sequence, together with the undelayed pulse profile at $P_p = 0$ mW (blue dotted line) in HNLF. Both fast and slow modulation methods result in very similar pulse profile modification without significant broadening. The amplitude of the pulses is normalized as a percentage of the peak pulse height; Fidelity metrics are shown in (c) EO and (d) SNR as functions of P_p, demonstrating better performance with the fast modulation.

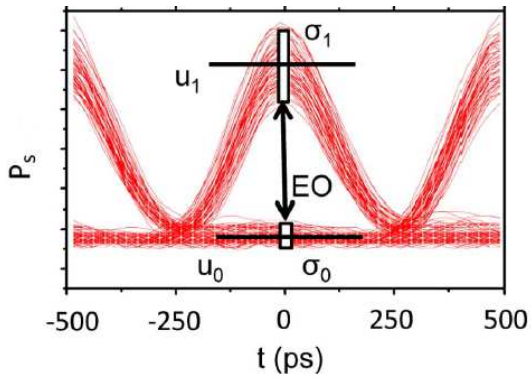

FIGURE 4.4: Example of eye diagram measured by an oscilloscope. The vertical box indicates the region of the eye diagram used to measure the standard deviation of "1s" and "0s" at the eye-center, u_1 and u_0 denote the mean level for the "1s" and "0s". EO shows the eye opening.

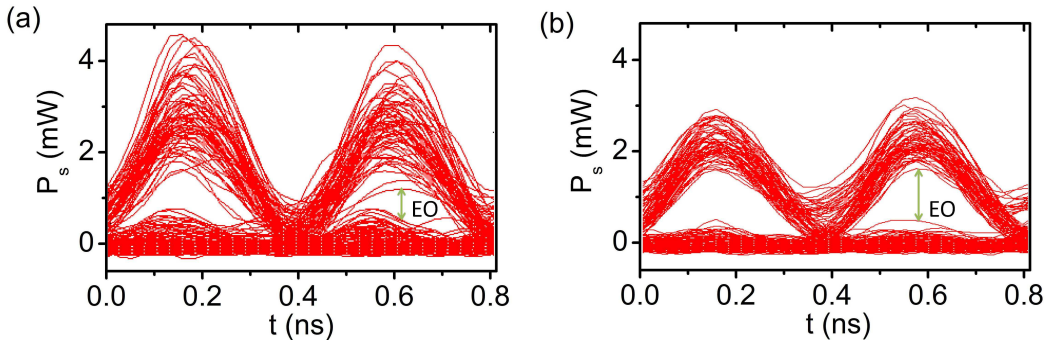

FIGURE 4.5: Eye diagrams of delayed and amplified data sequences for (a) slow and (b) fast modulation waveforms at $P_p = 350$ mW in HNLF. The arrows in the figure show the EO for each case.

5

Competing effects in a broadband SBS slow light system

In this chapter, I discuss several competing nonlinear optical processes commonly found in broadband SBS slow light systems: they are spontaneous Brillouin scattering, Rayleigh backscattering, stimulated Raman scattering and Kerr-induced modulation instability. Here, I discuss how these processes degrade the performance of SBS slow light and various ways to avoid them or reduce their negative effects.

In the past several years, many advances have been made in slow light technology that aim to improve the maximum achievable fractional delay (i.e. equivalent to the delay-bandwidth product) while broadening the bandwidth up to GHz range [9, 16, 36, 40–42, 75, 76], including the high-fidelity fast noise modulation method introduced in Ch. 4. [9, 18]. In all the broadband SBS slow light experiments, pump power requirements scale up with the bandwidth. As a result, the performance of broadband SBS slow light devices are prone to competing nonlinear optical effects. High input pump power is concentrated in the optical fiber, giving rise to high intensities, which can trigger a number of competing nonlinear effects. These nonlinear

optical effects take power away from the pump beam, and thus limit the SBS gain, effectively restricting the delay. Moreover, some competing processes generate additional optical beams that propagate along with the SBS signal. These beams contribute to un-correlated noise for the slow light system and must be filtered out to avoid degradation of the true signal.

Particularly, I find that modulation instability (MI) is the dominant competing process in an SBS medium with a background anomalous group velocity dispersion ($\beta_{20} < 0$), which has not been reported before. This finding demonstrates that sign of the dispersion of an optical fiber is crucial for its broadband SBS slow light performance. I find that the MI process depletes most of the pump power for the SBS process in a 9.2-GHz broadband SBS slow light device using a standard 20-km-long single-mode LEAF fiber as the SBS medium. This result was obtained when the central wavelength of the pump laser was set to 1.55 microns, where the LEAF fiber has a anomalous group velocity dispersion. The dominance of MI in the LEAF-fiber-based system suppresses the SBS gain, degrading the SBS slow light delay and limiting the SBS performance in terms of gain-bandwidth. I find an improvement in the SBS slow light delay in a dispersion-shifted optical fiber, where MI is suppressed by the normal dispersion. I obtain a gain-bandwidth product of 344 dB·GHz, much increased compared to 126 dB·GHz in the LEAF system. The new gain-bandwidth is limited only by our available pump power of 0.82 W.

In this experiment, I set up a broadband slow light system described in Dr. Cabrera-Granado's paper [18]. Dr. Cabrera-Granado, Dr. Calderon and Dr. Melle have contributed in the experiment setup. The interference from MI has been identified by me and Prof. Gauthier. We collected data and performed data analysis. Dr. Okawachi and Professor Gaeta have characterized the dispersion of the optical fibres used in the experiment. We summarize the results in reference [8], in which Professor Gauthier and I have been primarily responsible for drafting the manuscript.

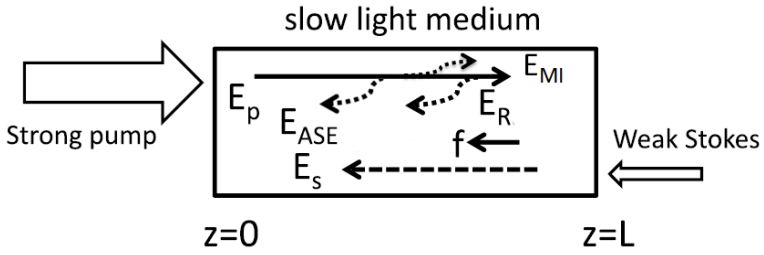

FIGURE 5.1: Geometry of the SBS interaction and competing nonlinear optical processes. The complex field amplitudes for the signal, pump, Rayleigh back scattered wave and modulation instability generated waves are denoted by E_s, E_p, E_R and E_{ASE}, respectively, and the Langevin noise source is denoted by f.

In Sec. 5.1, I describe the mechanism and protection measures for four competing nonlinear processes that can possibly suppress the SBS process in our broadband SBS slow light experiment. In Sec. 5.2 I experimentally study the suppression of SBS caused by the modulation instability in a broadband SBS device, where a standard single-mode LEAF fiber is used as the SBS medium. As a solution to the problem, I show that the MI and the associated SBS slow light degradation are eliminated by using a dispersion shifted fiber that has normal dispersion at the 1.55 μm wavelength window. In Sec. 5.3, I compare the SBS gain-bandwidth-product limit imposed by the MI with the limit imposed by SRS following the approach of Olsson *et al.*[39] in the LEAF-based system. Conclusions are given in Sec. 5.4.

5.1 Competing processes in a broadband SBS slow light system

5.1.1 Stimulated Brillouin scattering

The geometry of the SBS interaction is shown in Fig. 5. Two beams (weak Stokes and pump) counterpropagate through the slow-light medium (optical fiber) in the z direction. The interference beating between the two beams generates a density wave via electrostriction. The opto-acoustic coupling between the three waves becomes

strong when the frequency of the signal beam is tuned to the Stokes line. In this case, the Stokes beam experiences amplification due to the SBS gain resonance, which also gives rise to the slow light effect. For slow light buffer applications, the data sequence is encoded on the Stoke signal beam via a Mach-Zehnder modulator.

In our slow light device described below, we generate a nearly ideal flat-topped SBS gain proifle with a spectral width (FWHM) $\Gamma/2\pi = 9.2$ GHz, by broadening the spectrum of the pump laser diode using the periodic modulation method introduced in Ch. 3 [8, 18].

As discussed in Ch. 3, even without competing effects, a strong initial signal beam can cause pump depletion and SBS gain saturation. This is because the signal beam is amplified exponentially as the pump power increases linearly. So the growth of the signal power can eventually catch up with the pump power. If the input signal beam has a power of P_{s0}, the output power of a on-resonance signal beam, whose spectral width is narrower than Γ, is given approximately by

$$P_s = P_{s0}^{G_0}, \tag{5.1}$$

where G_0 is the SBS line center intensity gain, given in Eq. (3.14). The depletion takes place when the Stokes beam becomes so strong that its magnitude is comparable to the pump beam, i.e. $P_s \sim P_p$. We therefore conclude that the SBS gain saturates around the threshold value,

$$G_{th0} \approx \ln(P_p/P_{s0}). \tag{5.2}$$

As discussed in Chs. 3 and 4, we use a weak signal beam that does not deplete the pump wave to avoid signal beam-induced gain saturation. In this case, the output of the signal power spectrum $p_s(\delta\omega)$ is correctly described by the transfer function H_{SBS},

$$p_s(\delta\omega) = \exp(-\alpha L)p_{s0}(\delta\omega)\exp[2g(\delta\omega)L_{\mathtt{eff}}] = H_{\mathtt{SBS}}P_{s0}, \tag{5.3}$$

where $\delta\omega$ is the signal detuning from the center resonance, α is the material intensity absorption coefficient, L and $L_{\mathtt{eff}}$ are the natural fiber length and effective fiber length,

respectively, and $g(\delta\omega)$ is the gain profile given in Eq. (3.11). In this case, the SBS gain threshold is determined by the amplified spontaneous Brillouin scattering.

5.1.2 Amplified spontaneous Brillouin scattering

The pump wave also generates scattered light in the absence of a coherent signal due to amplified spontaneous Brilloiun scattering. Spontaneous Brillouin scattering arises from thermal fluctuations in the fiber, which are subsequently amplified by the SBS process. The amplification of the spontaneous Brillouin scattering also deplete the power in the pump beam, setting a SBS gain threshold to $G_{th} \sim 10$ in single mode fibers [44, 69] for single-line SBS resonances. In addition, this noisy wave counterpropagates with respect to the pump wave and has a similar spectral content to the the input data stream. As a result, amplified spontaneous Brillouin scattering cannot be removed from the signal beam and degrades the signal fidelity.

Following Boyd *et al.* [45], we account for amplified spontaneous Brillouin scattering by assuming that the spontaneous scattering is a Langevin process described by a δ-correlated Gaussian random variable with zero mean and correlation amplitude $Q_{th} = (2k_B T\rho_0\Gamma_B)/(v^2 A_{\mathtt{eff}})$, where k_B is Boltzmann's constant, T is the temperature, ρ_0 is the average material density, v is the speed of sound in the fiber, and $A_{\mathtt{eff}}$ is the effective cross-sectional mode area of the beams in the fiber [43–45]. The power spectral density for amplified spontaneous emission (ASE) is then given by [73]

$$p_A(\delta\omega) = K_A[H_{\mathtt{SBS}}(\exp(-\alpha L) + \frac{\alpha}{2g(\delta\omega)}) - (1 + \frac{\alpha}{2g(\delta\omega)})], \tag{5.4}$$

where $K_A = 2\pi k_B Tc/n\Omega_B$. The ASE noise power is denoted by P_A and is approximately equal to $p_A\Gamma$ for a flat-top gain profile. This noisy optical field gives rise to current fluctuations in the detector due to two effects. One effect is the beating of the signal wave with the ASE wave, while the other source is the beating of the noisy ASE wave with itself. This amplified SBS is the major competing process and the one that causes

the most error.

5.1.3 Rayleigh backscattering

The pump wave also induces Rayleigh back scattering that co-propagates with the signal, as illustrated in Fig. 5. Rayleigh scattering is the scattering of light beam from the stationary non-uniform density variations in the material [68]. In the optical fiber, although Rayleigh scattering is generally uniform in all directions, only the scattered waves in the forward and backward directions stay confined in the waveguide and propagate along the fiber. Due to Rayleigh backscattering (RB), a small portion of the pump beam is backscattered and couples into the back propagating mode in the optical fiber. The noisy backscattered wave [46] then travels in the same direction as the signal beam, and mixes with the signal, causing additional noise. The power of the RB wave is proportional to the pump beam and is expressed as

$$P_{RB} = a_{RB} P_p, \tag{5.5}$$

where a_{RB} is the RB parameter.

The RB process is weak and only detracts a small portion of the pump beam in the fiber, typically on the order of $a_{RB} \sim 10^{-5}$ [77, 78]. Therefore, the pump depletion due to RB is negligible. On the other hand, the high pump power required for broadband SBS slow-light techniques makes P_{RB} an excess noise comparable to the signal power, especially in the low gain region. Fortunately, Rayleigh scattering has an identical spectrum to the pump wave spectrum and hence can be removed using a narrow-band spectral filter that is centered at ω_s. In our experiments, we use a fiber Bragg grating to eliminate this potential noise source.

5.1.4 Stimulated Raman scattering

Stimulated Raman scattering (SRS) is another competing nonlinear effect in which a pump beam is scattered by high-frequency optical phonons [68]. In optical fibers,

the SRS gain resonance has a broadband spectrum with a central frequency down-shifted by ∼13 THz from the frequency of the pump beam. Similar to the amplified spontaneous Brillouin scattering, amplified spontaneous Raman scattering occurs in the presence of a strong pump beam. Spontaneous Raman scattering initiated from the quantum fluctuations is amplified by the pump beam. When the SRS gain reaches a threshold value of ∼10 in single-mode fibers [19, 68], most of the pump power is transferred to the Stokes beam and the pump beam is depleted. Unlike SBS, SRS has a broad resonant spectrum as a result of the fast response time of SRS in single-mode fibers (<1 ps) [79].

The SRS gain associated with a monochromatic pump is typically two orders-of-magnitude smaller than the SBS gain, and therefore has little effect on the SBS process. However, SBS gain is inversely proportional to the pump bandwidth, as shown in Eq. (3.19). On the other hand, Raman resonance has a bandwidth on the order of THz, a spectral broadened pump beam up to tens of GHz is considered monochromatic in the Raman scattering process. As a result, the Raman gain is not affect in broadband SBS slow light systems. As bandwidth increases, the SBS gain will eventually match the SRS gain, setting the scale for competition between these processes.

5.1.5 Modulation instability

The modulation instability (MI) is yet another process that can compete with the broadband SBS process. MI results from the interplay between the nonlinear Kerr effect and material dispersion. It is a four-wave-mixing process where two co-propagating photons of the same frequency are converted into a frequency up-shifted and down-shifted photon pair [19, 80, 81]. As a result, the MI broadens the spectrum of continuous wave (cw) or quasi-cw beams, and can even turn a continuous wave beam into a train of pulses [80, 82, 83] or generate a supercontinuum [84]. In the presence of a strong cw or quasi-cw beam propagating through the optical fiber, noise components

in the vicinity of the MI gain peaks experience exponential amplification. This leads to the creation of two symmetric spectral side lobes [19, 80]. The gain profile of the MI is given by [19]

$$G_{MI}(\omega_{MI}) = 4\pi^2|\beta_{20}\omega_{MI}|\sqrt{2\Omega_{peak}^2 - \omega_{MI}^2}L, \tag{5.6}$$

where ω_{MI} is the detuning from the pump frequency, Ω_{peak} (in cycles/s) is the frequency shift at which the maximum gain is obtained, and β_{20} is the group velocity dispersion (GVD) parameter, introduced in Ch. 2. Here [19],

$$\Omega_{peak} = \pm\frac{1}{2\pi}\sqrt{\frac{2\gamma P_p}{|\beta_{20}|}}, \tag{5.7}$$

where γ is the Kerr nonlinear parameter. Similar to SRS, the MI is not affected by the 9.2 GHz pump broadening due to its fast response time (<10 fs)[19]. The generated waves propagate in the same direction as the pump beam, so MI waves do not mix with the signal beam. Instead, the MI can deplete the pump power in broadband SBS slow light devices, as we show in the next section.

5.2 Experimental study of competition between MI and SBS in a 10-GHz SBS slow light system

We study the competition between SBS and MI in a broadband SBS slow light system shown in Fig. 7.2. We use a distributed feedback (DFB) laser operating at ∼1.55 μm as the pump source. I modulate the injecting current of the DFB laser with a modified triangle function so that the output beam of the DFB laser has a square-shaped spectrum with a bandwidth of 9.2 GHz [18]. The output of the DFB laser is then amplified using an erbium-doped fiber amplifier (EDFA) to provide enough pump power for the broadband SBS process. The EDFA also controls the input pump power thereby controlling the SBS gain. I use another DFB laser to generate the

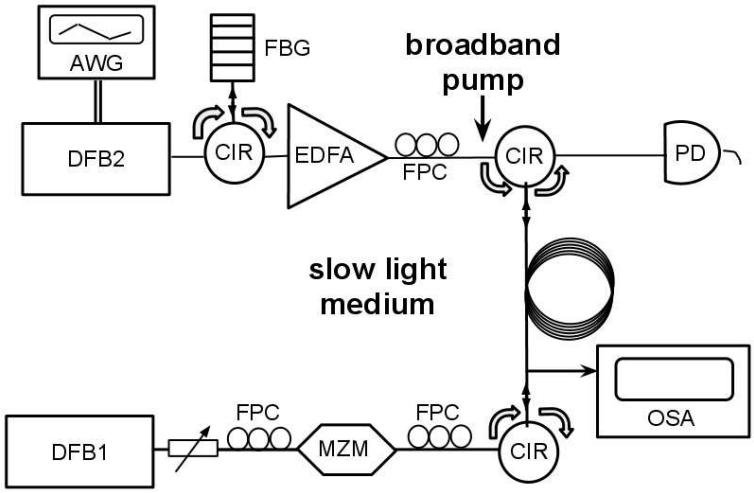

FIGURE 5.2: Experimental Setup. The injection current of the pump laser (DFB2) is modulated by an arbitrary wavefunction generator (AWG). The current modulation function is tailored to produce a flat-topped broadened gain profile [18]. A Fiber Bragg Grating (FBG) (bandwidth $\Delta\nu = 24$ GHz, central wavelength $\sim$1.55 μm) is used to filter out unwanted frequency sidebands from the DFB laser. An EDFA amplifies the pump beam before it is injected into the fiber via a circulator. The signal beam (DFB1) is modulated with a Mach-Zehnder modulator (MZM) and is injected from the other end of the fiber via a circulator. Fiber polarization controllers (FPC) are used to match the polarization orientations of the pump and signal beams. A photodiode (PD) measures the output power of the signal beam and an optical spectrum analyzer (OSA) measures the spectrum of the output pump beam.

signal beam, which is tuned to the SBS resonance. To avoid probe-induced SBS gain saturation, I attenuated the signal beam to a power of 2 μW before injecting it into the SBS medium, where the signal beam counterpropagates and interacts with the pump beam via the SBS process. The amplified and delayed signal is detected at the output of the fiber. The gain G is obtained by measuring the output powers of the signal beam with the pump beam on and off.

I use two different fibers as the SBS medium in the experiment, a 20-km-long LEAF fiber from Corning and a 2-km-long HNLF fiber from OFS. I focus here on the LEAF fiber because it is a readily available, relatively inexpensive fiber used in long-haul

communication systems and hence is likely to be selected for SBS slow light devices. The parameters of the fibers are shown in Table 7.1. I measure the background GVD parameter β_{20} by the time-of-flight method [85]. In this method, I measure the group velocity as a function of the wavelength by recording the transit time for optical pulses to propagate through the fiber with different central wavelengths. I obtain the GVD by dividing the group velocity differences by the wavelength shift. I then determine the nonlinear parameter γ using $\gamma = 2\pi n_2/\lambda A_{\mathtt{eff}}$, where the nonlinear-index coefficient $n_2 \sim 2.5 \times 10^{-20} \mathrm{m}^2/\mathrm{W}$ is used for silica [68].

Table 5.1: Parameters of the fibers used in the experiment.

	$A_{\mathtt{eff}}$	$L_{\mathtt{eff}}$	G/P_p(linear region)	γ	β_{20}
LEAF	72 μm^2	12.8 km	10.5 W^{-1}	1.4 W^{-1}km^{-1}	-5.29 ps^2/km
HNLF	11.7 μm^2	1.64 km	11.1 W^{-1}	8.7 W^{-1}km^{-1}	0.08 ps^2/km

As one of the most used, low-cost, standard, single-mode fibers, the LEAF fiber offers great compatibility and would substantially lower the cost of SBS slow light devices, which is why I used it in our experiment. However, the zero-dispersion wavelength for the LEAF is shifted to ~ 1.6 μm, resulting in a large anomalous background dispersion β_{20} at $\sim$1.55 μm. The anomalous dispersion degrades the SBS slow light performance, as shown below.

I measure the SBS gain as a function of P_p for the LEAF fiber and the result is shown in Fig. 5.2(a). As P_p is increased from zero to 0.8 W, G first scales linearly with P_p, with a slope of 10.5 W^{-1}, and then starts to saturate and deviate from linear growth at $G \sim$4, corresponding to an input power $P_p \sim$0.4 W (Fig. 5.2(a)). The early saturation of the SBS gain limits the slow light delay.

The saturation behavior shown in Fig. 5.2(a) could be the result of pump depletion due to the SBS process, but additional observations rule out this possibility. First, the saturated value of the gain is $\sim$4, which is much smaller than the threshold gain $G_{th} =$ 10, indicating that saturation is not induced by spontaneous Brillouin amplification.

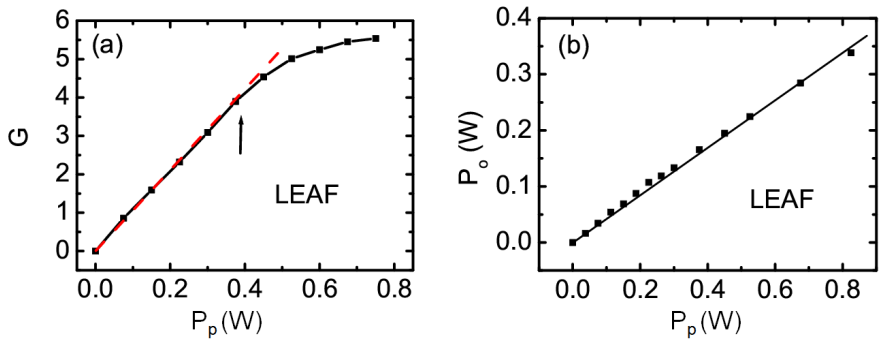

FIGURE 5.3: Early saturation of the SBS gain. (a) The SBS gain G as a function of input pump power P_p. Saturation is observed around $G \approx 4$ (vertical arrow), corresponding to an input pump power of ∼0.4 W; (b) Total power P_o transmitted through the fiber in the pump beam direction (not spectrally resolved) as a function of the input pump power P_p, indicating high fiber transparency. In the experiment, a weak continuous-wave beam with an input power of 2 μW is used as the signal beam.

Second, the amplified signal power, P_s, is only 0.5 mW, which is small in comparison to the input pump power 0.75 W, and is hence insufficient to deplete the pump. Moreover, the total power, P_o, transmitted through the fiber in the direction of the pump beam grows linearly as P_p is increased from 0 to 0.8 W (Fig. 5.2(b)). This is a direct evidence that the total transmitted pump power is not depleted.

To explain the early SBS gain saturation at G ∼4, I examine the transmitted pump spectrum p_o passing through the 20-km-long LEAF fiber (Anritsu model MS9710B optical spectrum analyzer). As P_p is increased from zero to 0.8 W, no significant Raman gain is observed (Fig. 5.2(a)). On the other hand, in a spectral span of 10 nm, symmetric side lobe structures emerge and grow quickly as P_p increases (Fig. 5.2(b)). At high P_p, the spectrum of the pump is flattened as a result of the emergence of secondary sidebands, and the power is spread into a broad frequency span of ∼200 GHz. Notice that the pump power transferred to the side lobes is no longer on resonance with the signal beam in the SBS interaction and therefore does not contribute to the SBS gain process.

To determine the amount of power loss, I integrate the power spectral density p_o

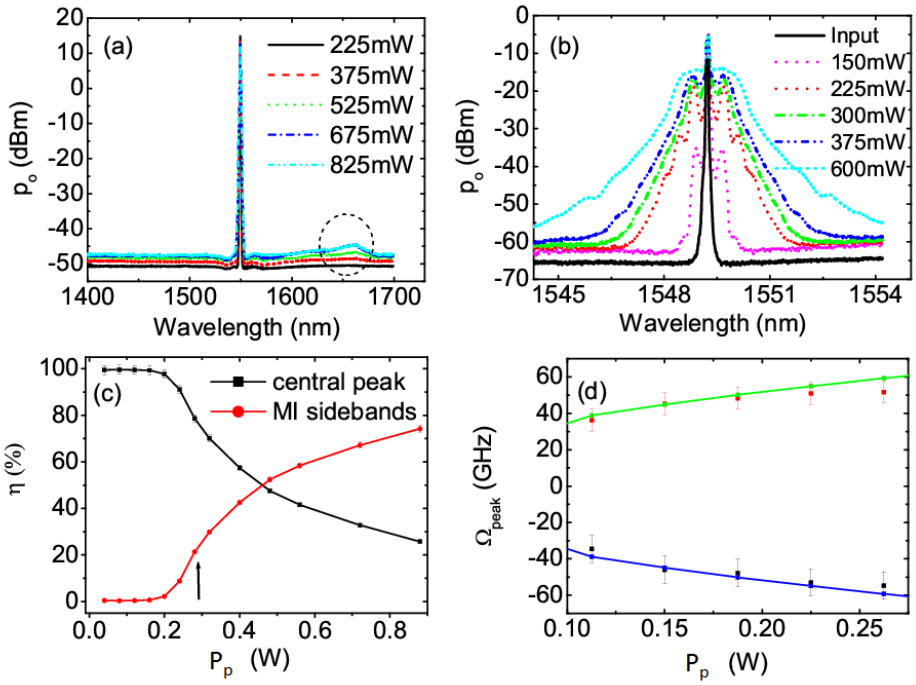

FIGURE 5.4: Modulation instability in the LEAF fiber. (a) Output power spectral density p_o of the pump laser (span of 300 nm) with increasing input power P_p. The circle indicates the Raman peak. (b) Output power density spectra p_o of the pump laser (a span of 10 nm) with increased input power P_p. The input spectrum of the pump laser (at 40 mW) is also shown. (c) Percentage (η) of power distributed in the central peak (black square) and in the MI sidebands (red circle) for the output pump beam, as functions of the input power P_p. The arrow indicates a threshold at ∼0.3 W. (d) Experimental data (point) and theoretical prediction (line) of the frequency shift Ω_{peak} of the MI side lobe peaks as a function of input power P_p.

in the side lobes. The results are shown as percentages of the total power P_p in Fig. 5.2(c). We see that a considerable portion ($> 20\%$) of the pump power is transferred to the sidebands when the input power exceeds P_p ∼0.3 W. I define this point as the threshold for the MI process, and the corresponding input pump power as the threshold power P_{th}^{MI} in the LEAF fiber. I obtain the threshold gain G_{th}^{MI} by Eq. (5.6) to be ∼10. Note that P_{th}^{MI} is close to the location where the early saturation of SBS gain occurs. I also compare the measured frequency shifts Ω_{peak} of the MI sidelobe peaks with the theoretical prediction using equation Eq. (5.7) and obtain good agreement, as

shown in Fig. 5.2(d). These observations lead us to conclude that the strong saturation of the SBS gain is caused by the MI-induced pump broadening. In conclusion, we find that MI dominates over SBS beyond a threshold pump power of $P_{th}^{MI} = 0.3$ W in the LEAF fiber. In a broadband system where $\Gamma = 9.2$ GHz, the threshold pump power corresponds to an SBS gain $G \sim 3.2$, which leads to a limit of 29 GHz or 126 dB·GHz on the SBS gain-bandwidth product.

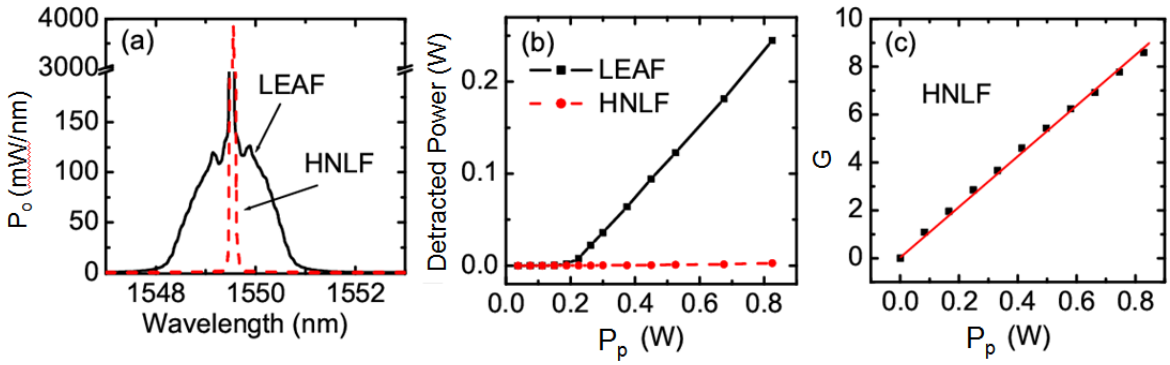

FIGURE 5.5: Suppression of modulation instability in HNLF. (a) Output power spectrum p_o of HNLF (red dash) and LEAF (black solid) at an input power of 0.8 W; (b) MI detracted pump power as a function of input power P_p in HNLF (red dot) and LEAF (black square).(c) SBS gain G in HNLF as a function of the input power P_p.

I next turn to the dispersion-shifted HNLF fiber, which has a small and normal dispersion at 1.55 μm. Because it is widely known that the MI is suppressed due to phase matching constraints in normally dispersive materials [19, 80, 86], I expect to see suppression of the MI and improvement in the gain-bandwidth product for the broadband SBS slow light with the HNLF fiber. Fig. 5.2 shows that the MI-induced limit on the SBS gain-bandwidth product is indeed removed. With the same 9.2 GHz broadband pump input, the transmitted pump spectrum through the HNLF shows no significant MI peaks (Fig. 5.2(a)). The power converted into off-resonant frequencies is negligible (Fig. 5.2(b)). As expected, early saturation of the SBS gain in the HNLF does not appear (Fig. 5.2(c)), resulting in a larger SBS gain-bandwidth product of 344 dB·GHz, limited by our available pump power of 0.82 W. The result further confirms

that MI induced pump broadening is the origin of the early saturation of SBS gain in the LEAF fiber.

5.3 Comparison of MI with SRS

In this section, I compare the relative importance of the two effects that compete with SBS in our broadband SBS slow light system. Following Olsson *et al.*'s approach [87], I compare the pump power P_p requirements for the broadband SBS, SRS, and MI processes in the LEAF fiber. Figure 5.3 shows the input pump power P_p required to obtain a threshold gain of 10 as a function of the bandwidth Γ. The threshold pump power for the SBS process is obtained from equation Eq. (3.19) taking G =10 and $g_0 = 1.06 \times 10^{-11}$ m/W (obtained from Fig. 5.2(a)),

$$P_p = G\frac{\Gamma}{2\Gamma_B}\frac{A_{\mathtt{eff}}}{g_0 L_{\mathtt{eff}}}\arctan^{-1}(\Gamma/\Gamma_B). \tag{5.8}$$

Note that I assume that a weak probe beam is used so that the probe-induced SBS saturation does not appear.

The SRS gain is given by [19]

$$G_{SRS} = 2g_R P_p L_{\mathtt{eff}}/A_{\mathtt{eff}}, \tag{5.9}$$

where $g_R = 1.26 \times 10^{-14}$ m/W [19]. The threshold power required for an SRS gain of 10 is obtained by $P_p = 10A_{\mathtt{eff}}/(2g_R L_{\mathtt{eff}}) = 2.23$ W. The pump power required for a MI gain G_{MI} ∼10 is found to be ∼0.3 W, as mentioned previously.

As shown in Fig. 5.3, beyond a bandwidth of ∼3.2 GHz, the LEAF-fiber system hits the MI threshold before it saturates the SBS gain. As a result, MI sets a limit on the SBS gain-bandwidth product. The gain-bandwidth product limit is 29 GHz, or 126 dB·GHz using G=10 in the LEAF fiber. Figure 5.3 also shows that the SRS becomes more efficient than SBS when the bandwidth goes beyond ∼22 GHz, and limits the

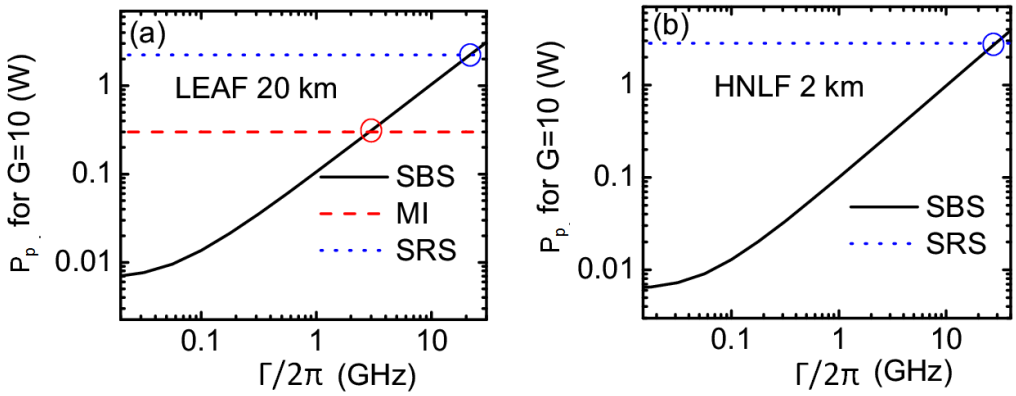

FIGURE 5.6: Pump power P_p required for a G of 10 versus the bandwidth Γ.

SBS gain-bandwidth product up to 220 GHz or 955 dB·GHz. The result is consistent with what Olsson *et al.* predicts [87]. In the LEAF fiber, the SBS gain-bandwidth product is restricted by the tighter MI-induced limit. However, in normally dispersive fibers where the MI is suppressed, SRS becomes the main limitation on the SBS gain-bandwidth product.

5.4 Conclusion

In conclusion, I summarize four common competing nonlinear effects in optical fibers in a broadband SBS slow light system. I calculate the noise power for the amplified spontaneous Brilloun scattering and Rayleigh backscattering, while the pump depletion effect is compared between SRS and MI. I also find that while Rayleigh backscattering can be filtered out, ASE noise has the same spectrum as the signal beam and thus cannot be removed. the quantitative analysis of noise for broadband SBS slow light is present in [73], which was the first analysis of the field.

Moreover, in a 9.2 GHz SBS slow light system, I find for the first time that MI dominates in the high pump power region and sets a limit on the SBS gain bandwidth product, which is 126 dB·GHz in the LEAF fiber. However, in normally dispersive materials, the SBS performance improves and there is little to no pump depletion. Our

findings shows that fiber dispersion is a crucial criterion for the selection of broadband SBS slow light medium. The results have been summarized in [8]

6

SBS group velocity dispersion

In this chapter, I demonstrate the creation of a strongly dispersive material with large chirp and small group delay using stimulated-Brillouin-scattering (SBS) based fast and slow light in a phontonic crystal fiber. This is in contrast to previous SBS slow light experiments, which have typically focused on the creation of a slow light material with minimal dispersion and chirp. However, the same method of optimizing desired optical properties with the tailoring of SBS resonance is applied here. The design of large GVD parameter in optical fiber is an extension of slow light SBS into general optical material design.

In the experiment, I demonstrate giant and adjustable GVD over the range ± 7.5 ns^2/m, appropriate for nanosecond-duration pulse, realized using an optical fiber pumped by an auxiliary laser beam. The dispersion is $\sim 10^9$ times larger than that obtained in standard single-mode fiber. This is the first demonstration of all-optical GVD control using SBS in optical fibers, which greatly reduces the experiment complexity compared to previous experiments using atom gases. Following this work, the dispersion profile can be optimized for specific applications by tailoring the pump-laser

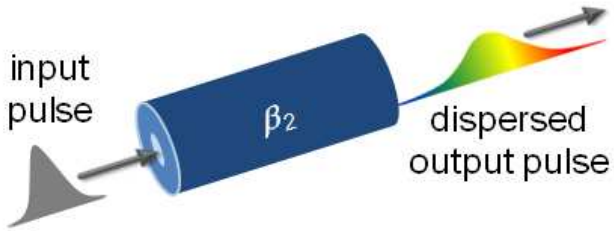

FIGURE 6.1: An input transform-limited optical pulse broadens temporally and develops a linear frequency chirp as it propagates through a material with group velocity dispersion parameter β_2 (illustrated here for the case when $\beta_2 > 0$).

spectral profile.

The results in this chapter is summarized in a manuscript [10]. In this project, I took the leading role in developing the experimental setup, collecting and analyzing the data. I also wrote the manuscript. Dr. Joel Greenberg has developed the experimental setup, collected and analyzed the data, and wrote the manuscript. Nor Ain Husein has developed the experimental setup and collected preliminary data. Professor Gauthier has conceived the experiment, collected and analyzed the data, wrote the manuscript, and supervised the overall project.

6.1 Group velocity dispersion in materials

Group velocity dispersion refers to the frequency-dependent group velocity of an optical waveguide. Upon propagation in a GVD waveguide, a short optical pulse will be broadened and will obtain a temporal frequency chirp as a result of the separation of different frequency components in the temporal domain (Fig. 6.1). GVD materials are widely used in various applications and crucial elements in recent research on temporal domain Fourier optics [49, 50, 53]. Motivated by recent research [1, 88, 89] that has demonstrated extreme values of group index n_g using resonances to enhance the material dispersion, I find that giant values of the GVD parameter β_2 can be ob-

tained when an amplifying resonance is placed next to an absorbing resonance. In general terms, our approach can be understood by considering one-dimensional pulse propagation along the z-direction in a linear dispersive material characterized by a frequency-dependent refractive index $n(\omega)$. In this case, electromagnetic theory predicts that the spectral amplitude of the output field is related to its input through the relation

$$A(z,\omega) = e^{ik(\omega)z}A(0,\omega) \tag{6.1}$$

where $k(\omega) = n(\omega)\omega/c$ is the pulse wavevector in the dispersive material and c is the speed of light in vacuum [19]. For pulses with a narrow band spectrum centered at the carrier frequency ω_0 and slow variation of $n(\omega)$ over the pulse spectrum, a Taylor series expansion of the complex wavevector magnitude

$$k(\omega) = \beta_0(\omega_0) + \beta_1(\omega-\omega_0) + \beta_2(\omega-\omega_0)^2/2! + \beta_3(\omega-\omega_0)^3/3! + \cdots \tag{6.2}$$

leads to approximate analytic solutions to the problem when the series is truncated, where the complex dispersion parameters are defined by

$$\beta_i = \frac{d^i k}{d\omega^i}|_{\omega=\omega_0}. \tag{6.3}$$

For the case when k is essentially real, as appropriate for transparent glasses, the phase velocity of the pulse is given by

$$v_p = \frac{c}{n(\omega_0)} = \frac{\omega_0}{\beta_0}, \tag{6.4}$$

and the group velocity is given by

$$v_g = \frac{c}{n_g(\omega_0)} = \frac{1}{\beta_1}. \tag{6.5}$$

An incident optical pulse will travel at the speed of v_g with a stable profile in a non-dispersive material where $\beta_2 = 0$. On the other hand, as illustrated in Fig. 6.1, an

incident transformed-limited pulse broadens and develops a linear frequency chirp due to GVD. The characteristic distance over which these effects develop is known as the dispersion length

$$L_D = \frac{t_0^2}{|\beta_2|}, \tag{6.6}$$

where t_0 is the a measure of the pulse width. The substantial dispersion needed for the applications mentioned above requires that the length of the material $L > L_D$. The quadratic scaling of L_D with pulse width is the reason why it is difficult to observe GVD effects for nanosecond-duration pulses for values of β_2 characteristic of typical dispersive materials and devices. For example, single-mode silica optical fibers has a GVD value of $\beta_2 \sim 20$ ps^2/km at the wavelength of 1.55 μm, which is restricted to dispersion applications for ps optical pulses.

As an example, consider a transform-limited Gaussian pulse without initial chirp. The amplitude profile is given in the form

$$A(0,t) = A_0 \exp(-\frac{t^2}{2t_0^2}) \tag{6.7}$$

where A_0 is the magnitude, t_0 is the half-width (at 1/e-intensity magnitude), related to the full width at half magnitude (T_0) by $T_0 = 2\sqrt{\ln 2}t_0 = 1.665t_0$.

The effect of GVD on optical pulse propagation in a linear dispersive material is described by solving the paraxial wave equation [19]. In a transparent material where k is real, the parameter β_1 describing the group velocity does not affect the pulse profile. The solution of the output pulse amplitude profile is given by

$$A(z,t) = \frac{1}{2\pi}\int_{-\infty}^{\infty} \tilde{A}(0,\omega)\exp(\frac{i}{2}\beta_2\omega^2 z - i\omega T)d\omega, \tag{6.8}$$

where $\tilde{A}$ is the Fourier transform of the amplitude at $z = 0$. For the Gaussian pulse

described by Eq. (6.7), the dispersed pulse is described by

$$A(z,t) = \frac{A_0}{\sqrt{t_0^2 - i\beta_2 z}} \exp[-\frac{t^2}{2(t_0^2 - i\beta_2 z)}] \tag{6.9}$$

where a phase term can be extracted that

$$\phi(z,t) = -\frac{\mathrm{sgn}(\beta_2)(z/L_D)}{1+(z/L_D)^2}\frac{t^2}{2t_0^2} + \frac{1}{2}\arctan(z/L_D). \tag{6.10}$$

Clearly, a quadratic phase term is obtained due to frequency chirp. This expression can be simplified when $\beta_2 z << L_D$,

$$\phi(z,t) \approx -\frac{\mathrm{sgn}(\beta_2)(z/L_D)}{2t_0^2} t^2 = a_2 t^2, \tag{6.11}$$

where the quadratic coefficient is given by

$$a_2 = -\frac{\beta_2 z}{2t_0^4}. \tag{6.12}$$

I will show next how to generate large β_2 using a double-line resonance.

6.2 Theory of SBS-based group velocity dispersion

In the SBS-base group velocity dispersion system, I use a pump wave with two frequency components, separated by roughly twice the Brillouin frequency. The resonant properties are explored at the center region between the two pump lines. The group velocity dispersion properties of the SBS system is derived base on theory in Ch. 2. According to Eq. (2.23), in the presence of an SBS resonance, the property of the waveguide is modified so that the signal beam traveling in the z direction $A_s(z,\omega_s)$ is given by

$$A_s(z,\omega_s) = A_s(0,\omega_s)e^{iKz}, \tag{6.13}$$

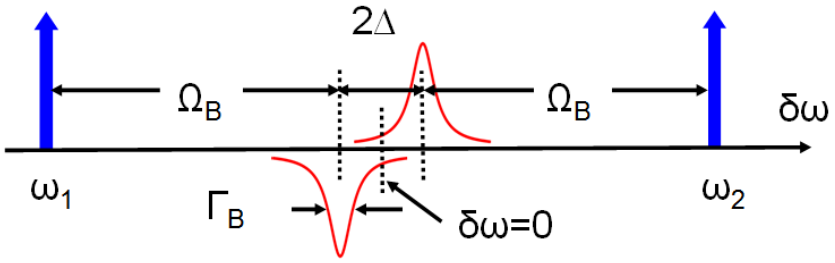

FIGURE 6.2: Illustration of the SBS resonances with dual pump beams. A counterpropagating pump beam of frequency $\omega_1(\omega_2)$ induces an anti-Stokes absorption (Stokes gain) line (shown in red) at frequency $\omega_1 + \Omega_B(\omega_2 - \Omega_B)$ and full-width at half-maximum width Γ_B. The spacing between the gain and absorption lines is 2Δ, shown here for the case when $\Delta < 0$

where the SBS wavevector is given by

$$K = k_0 - i\tilde{g}I_p/2. \tag{6.14}$$

Here $k_0 = n\omega/c$ is the background wavevector, $\tilde{g}$ is the complex SBS resonance factor and I_p is the intensity of the pump beam. In a single-line SBS resonance, $\tilde{g}$ is given in Eq. (2.20) and Eq. (2.21) by

$$\tilde{g}_+ = \frac{-ig_0}{1 - 2i(-\omega_s + \omega_p - \Omega_B)/\Gamma_B} \tag{6.15}$$

for the Stokes gain and

$$\tilde{g}_- = \frac{ig_0}{1 - 2i(\omega_s - \omega_p - \Omega_B)/\Gamma_B} \tag{6.16}$$

for the anti-Stokes absorption. Here g_0 is the SBS gain coefficient, ω_p is the frequency of the pump beam, Ω_B is the Brillouin frequency and Γ_B is the resonance linewidth (half width at half magnitude).

As shown in Fig. 6.2, in our SBS system, I use two pump beams whose frequencies are placed symmetrically across the central frequency of the signal beam ω_0. The

frequency separation is set to $|\omega_1 - \omega_2| = 2\Omega_B + 2\Delta$, where Δ is a small detuning. At the vicinity of ω_0, the SBS gain resonance of one pump beam overlaps with the SBS absorption resonance of the other pump beam. The strength of the resonances are identical in magnitude and the complex profiles are given by $\tilde{g}_\pm I_j/2$, where $\tilde{g}_\pm$ is the SBS gain/absorption factor and I_j is the pump intensity of the pump beam at frequency ω_j, $(j = 1, 2)$. The center of the composite SBS resonance is at frequency ω_0 and the signal frequency relative to this value is denoted by $\delta\omega = \omega_s - \omega_0$.

The evolution of a weak signal beam in a dual-frequency pump system is given by Eq. (2.31), and the effective wavevector for our experiment setting is given by

$$K(\delta\omega) = k_0 - i\tilde{g}_- I_1/2 - 2i\tilde{g}_+ I_2 \tag{6.17}$$

$$= k_0 + \frac{ig_0 I_1/2}{1 - 2i(\delta\omega - \Delta)/\Gamma_B} - \frac{ig_0 I_2/2}{1 - i(\delta\omega + \Delta)/\Gamma_B}. \tag{6.18}$$

Figure 6.3 (a) shows the real and imaginary magnitudes for complex wavevector given by Eq. (6.17) assuming $I_1 = I_2 = I_p$. It is seen that the real part of K is symmetric about $\delta\omega = 0$ (as opposed to anti-symmetric for a single Lorentzian resonance) and is approximately quadratic, which results in large positive GVD. The profiles are inverted by changing the sign of Δ, which allows easy control over the sign of the GVD.

The dispersion parameter β_2 is obtained by taking the second derivative of the wavevector, shown in Fig. 6.3(b). Evaluating the derivative at the center frequency ω_0 yields the center dispersion

$$\beta_2(\omega_0) = \frac{d^2k}{d\delta\omega^2}|_{\delta\omega=0} = \frac{8g_0 I_p}{\Gamma_B^2}\frac{\Delta(\Delta^2 - 3\Gamma_B^2/4)}{\Gamma_B(\Gamma_B^2/4 + \Delta^2)^3} = \frac{8G}{\Gamma_B^2 L}\frac{\Delta(\Delta^2 - 3\Gamma_B^2/4)}{\Gamma_B(\Gamma_B^2/4 + \Delta^2)^3}, \tag{6.19}$$

where $G = g_0 I_p L$ is the SBS central intensity gain, L is the length of the optical fiber.

For the case when $\delta\omega = 0$, $\beta_2 L$ is purely real and is proportional to $g_0 I_p/\Gamma_B^2$. Thus, large GVD can be obtained for modest values of G and narrow-linewidth resonances

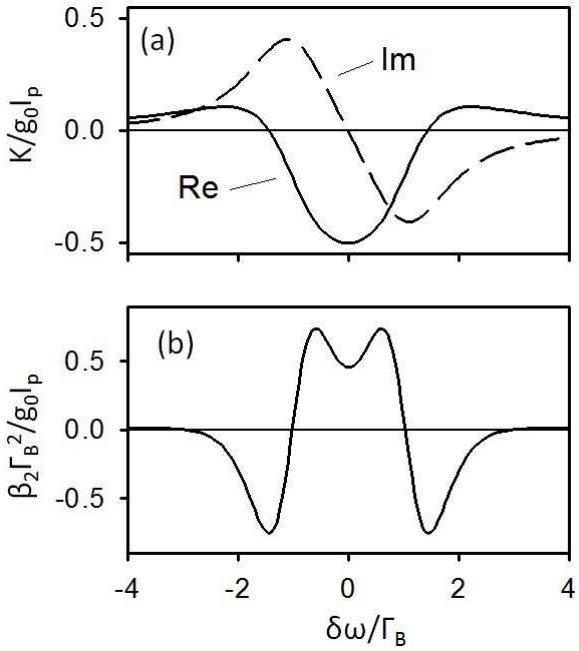

FIGURE 6.3: (a) Wavevector magnitude for a medium containing oscillators with a double resonance described by the wavevector given by Eq. (6.17) with $\Delta/\Gamma_B = -1.03$. (b) Group velocity dispersion parameter for the double-resonance medium for the same conditions as in (a).

that can be obtained, for example, in atomic gases [52] and via stimulated Brillouin scattering resonances induced in optical fibers [48, 56]. Figure 6.3(b) shows that β_2 is approximately constant over a bandwidth of Γ_B.

6.3 Experiment of SBS-based group velocity control

6.3.1 Dispersive SBS gain profile

To realize this dispersion profile experimentally, I induce stimulated Brillouin scattering (SBS) resonances in a commercially-available photonic crystal fiber (PCF). The expreiemnt setup is shown in Fig. 6.4. In the typical SBS process, a weak input beam interacts with a strong counterpropagating pump beam through wave mixing with an induced acoustic field [68], creating narrow Stokes (amplifying) and anti-Stokes (absorbing) resonances whose strength is proportional to the pump beam intensity.

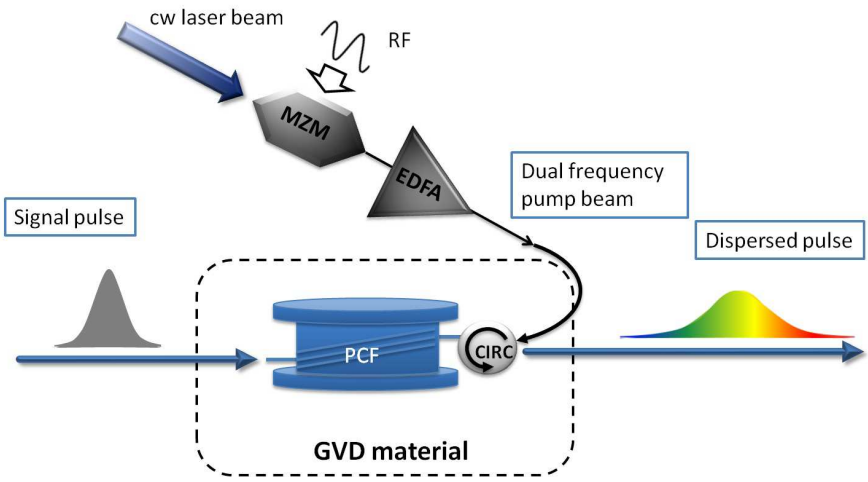

FIGURE 6.4: Experiment setup. MZM, Mach-Zehnder modulator. RF, radio frequency signal. EDFA, Erbium Doped Fibre Amplifier. PCF, photonic crystal fiber. Giant GVD is achieved using a 10-m-long PCF (NKT Photonics Inc., NL-1550-NEG-1, $\Gamma_B/2 = 24.2$ MHz) that is pumped by a 1.55-μm-wavelength bichromatic pump beam. The pump beam is created by modulating the output of a telecommunications laser (Fitel 47X97A04) with a Mach-Zehnder modulator (EOSpace AX-0K1-12-PFAP-PFA-R3-UL) operating in carrier-suppression mode and driven by a sinusoidal waveform produced by a microwave frequency source (Agilent E8267D). The modulated pump beam is passed through an erbium-doped fiber amplifier (IPG Photonics EAD-1K) and a Faraday circulator before injection into the PCF so that it counterpropagates with respect to the signal beam.

SBS resonances can be induced at any frequency where the material is transparent by adjusting the pump laser frequency, thus making this approach broadly tunable. To obtain adjacent amplifying and absorbing resonances as required by Eq. (6.17), I pump the PCF using a two-frequency pump beam, which allows us to place the anti-Stokes resonance arising from one of the pump frequency components close to the Stokes resonance arising from the other component as illustrated in Fig. 6.2.

As a first step in characterizing the dispersive material, I inject a weak continuous-wave signal beam into the bichromatically-driven PCF and measure the gain spectrum of the composite SBS resonances as shown in Fig. 6.5. To measure the gain spectra, I use an auxiliary signal laser beam (Agilent HP81862A, power 5 mW), whose frequency is scanned via current tuning. This beam is passed through a circulator before injection

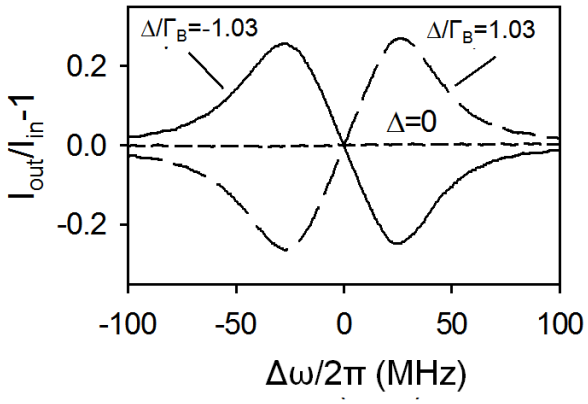

FIGURE 6.5: Experimentally observed probe beam transmission profile for different values of Δ, showing the output probe beam intensity divided by the input intensity. Here, $\Gamma_B/2\pi = 24.2 \pm 0.6$ MHz and $G = 0.28 \pm 0.03$.

into the PCF. The signal beam is passed to a photoreceiver (New Focus 1611) via the other circulator and measured with an oscilloscope.

As shown in Fig. 6.5, when $\Delta = 0$, there is essentially no change in the transmitted signal beam, demonstrating that the Stokes and anti-Stokes resonances do not depend on the relative phases of the pump beam frequency components and hence the wavevector given by Eq. (6.17) is appropriate. When $\Delta < 0$, I obtain a gain profile corresponding to the imaginary part of K shown in Fig. 6.3(a) and the profile inverts as discussed above when $\Delta > 0$.

6.3.2 Dispersion of a 28-ns Gaussian pulse

I next inject nanosecond-scale-duration, chirp-free Gaussian-shaped signal pulses with $\omega_s = \omega_0$ into the PCF and measure the frequency chirp using a homodyne detection technique (illustrated in Fig. 6.5). For the pulsed experiments, I generate the signal beam by splitting a small fraction of the power from the pump beam, thereby assuring that the frequency is locked to the pump beam. This beam is passed through a Mach-Zehnder modulator (OTI 10 Gb/s) driven by an arbitrary waveform generator (Tektronix AFG 3251).

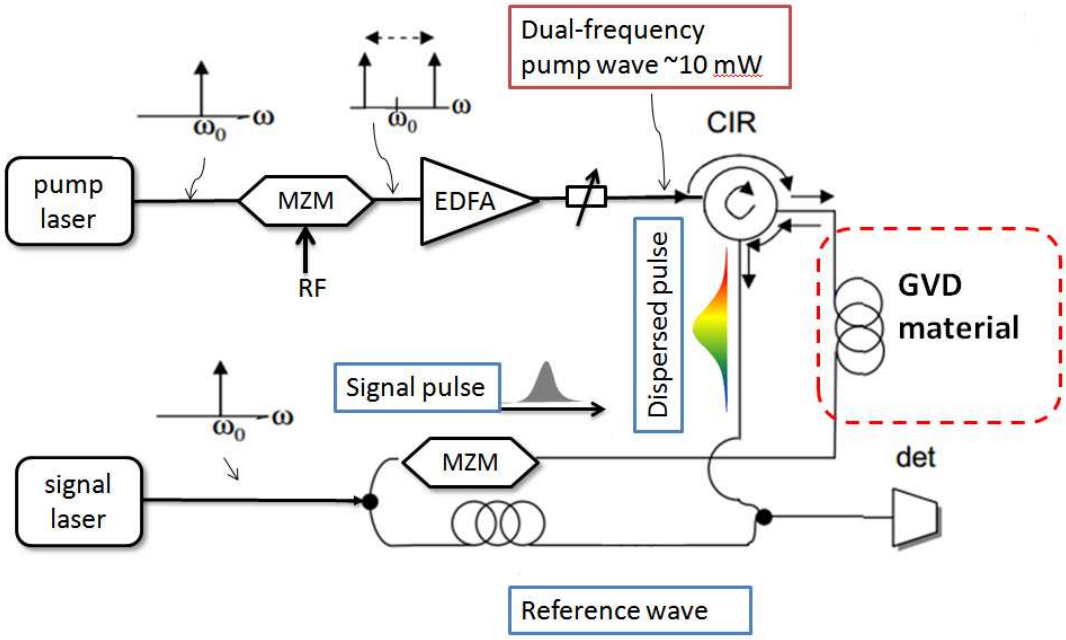

FIGURE 6.6: Experiment setup for the homondyne measurement. A reference arm splits part of the signal beam and mixes it with the dispersive pulse at the detector. The optical path lengths are balanced by matching the fiber lengths in the two arms.

To measure the chirp of the signal beam output pulse, I use a homodyne detector that mixes a small fraction of the signal source light with the output pulse and detected with the photoreceiver. Fig. 6.6 shows the experiment setup for the homodyne measurement. The interference waveform is captured with an 8-GHz-analog-bandwidth, 40 Gsample/s oscilloscope (Agilent DSO80804B) and downloaded to a computer for offline analysis. I fit the resulting waveform that assumes that the signal beam has a Gaussian envelope and a phase that is a second-order polynomial. The quadratic coefficient a_2 is directly related to β_2 by Eq. (6.12), where $t_0 = 16.94 \pm 0.1$ ns is the half width at 1/e magnitude of the Gaussian pulse, obtained by fitting the input pulse profile to a Gaussian in Fig. 6.7(b). A quadratic phase fitting to the interference profile is shown in Fig. 6.7(a) for $G = 0$.

Figure 6.8(a) shows that β_2 increases linearly with G (proportional to P_p) as ex-

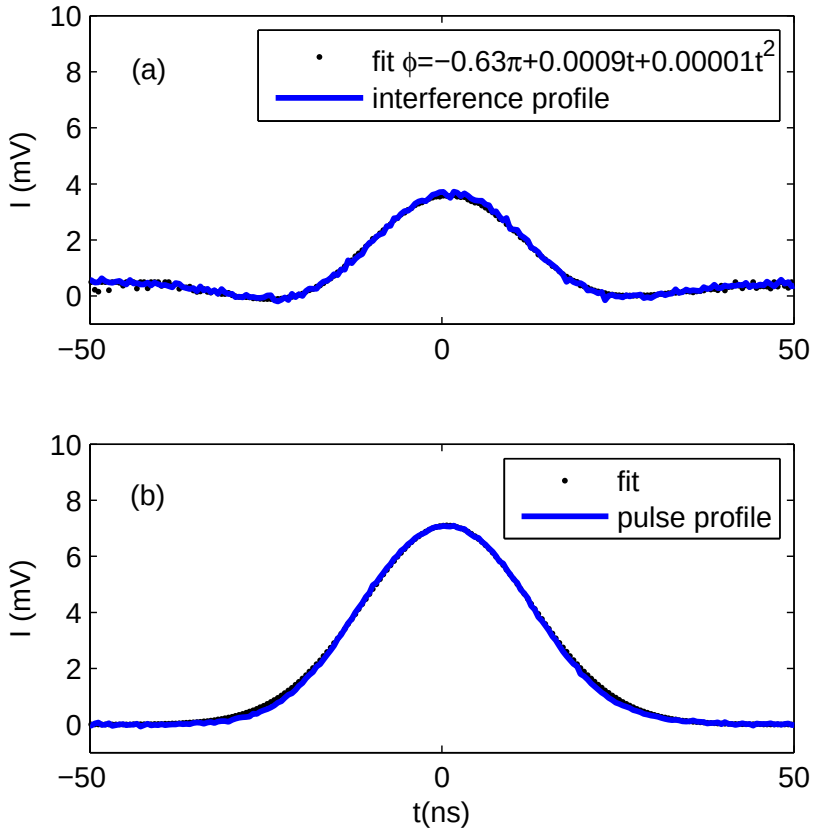

FIGURE 6.7: (a) Interference profile with quadratic phase fitting for $G = 0$, ϕ is the relative phase with the reference beam. (b) Input pulse profile with a Gaussian fit. The vertical axis shows the measured optical intensity via the voltage of the photoreceiver.

pected, demonstrating all-optical control of the GVD. I obtain a maximum value of $|\beta_2| = 7.5$ ns^2/m. Given that $\beta_2 \approx 20$ ps^2/km in a single-mode optical fiber, this value demonstrate a $\sim 10^9$ times increasement at the 1.55 μm. Negative GVD can be obtained by inverting Δ (see Fig. 6.5). Our observations are in good agreement with the solution to Eq. (6.19), which predicts that $\beta_2 L = -20.9\ \mathrm{Sgn}(\Delta) G$ (ns^2) for $|\Delta/\Gamma_B| = 1.03$, where Sgn is the sign function.

I also measure the output pulse intensity for different values of G, and hence β_2, as shown in Fig. 6.8(b). As expected, the pulse broadens and approximately maintains its Gaussian shape, also in good agreement with simulated predictions, which are

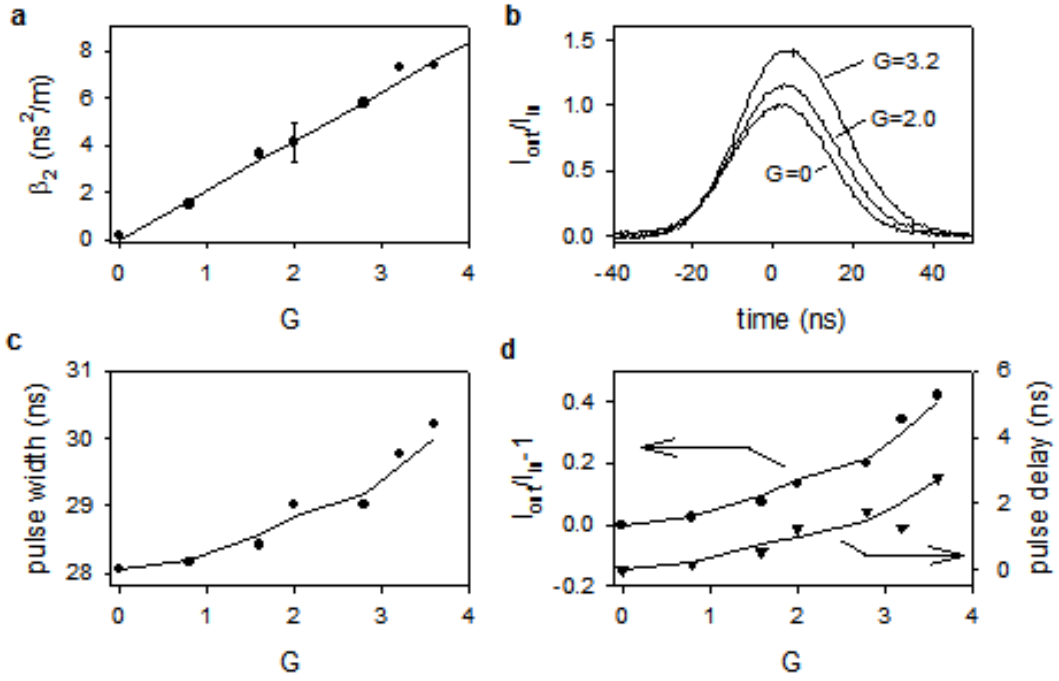

FIGURE 6.8: Observation of giant GVD in a laser-pumped optical fiber. a Linear variation of the GVD parameter with SBS gain, which is proportional to the intensity of the pump laser. b Temporal variation of the output pulse after passing through the GVD material for different values of the SBS gain. c Change in the width and d output peak intensity I_{out} as a ratio of the input peak intensity I_{in} and delay of the pulse after passing through the GVD material as functions of the SBS gain. The bars on the data points indicate typical errors.

based on the exact profile of wavevector given in Eq. (6.17). Figure 6.8(c) shows the observed and predicted increase in pulse width as a function of the SBS gain, where the agreement between the two is good.

In addition, I observe that the pulse amplitude increases somewhat and the pulse is delayed (Fig. 6.8(d)), which is not expected based on our discussion above that assumes an idea transparent dispersive medium. These non-ideal effects are due predominately to frequency-dependent gain and absorption arising from the imaginary part of K (see Fig. 6.3), which is unavoidable for a material satisfying the Kramers-Kronig relation [67]. For $\beta_2 > 0$, the high- (low-) frequency components of the pulse

spectrum are absorbed (amplified) in an approximately linear-in-frequency fashion, giving rise to a slight shift of the spectrum to lower frequency. Nevertheless, this small non-ideal behavior does not disrupt the GVD-induced linear frequency chirp and pulse broadening.

6.4 Conclusion

I have obtained a large GVD in a commercial photonic crystal fiber by using a double-line SBS resonance. The resultant GVD parameter is as high as $\beta_2 = 7.5$ ns^2/m, 10^9 larger than the that of silica optical fibers. The GVD work presented is very recent and I believe it's the first experiment in the world to use the SBS process to realize such large GVD. In this work, I have used two pump lines and only one detuning parameter Δ in the optimization procedure. However, the principle of the arbitrary SBS resonance tailoring technique is applied in the procedure and finer tailoring with more tuning parameters can readily applied. I expect a lot of following work to come, for example, by using the readily available SBS resonance tailoring techniques to obtain a broadband GVD.

The result can also be extended to applications in the even longer temporal region by using resonances with narrow bandwidth that matches the temporal scale. For example, recoil resonances in laser-pumped ultra-cold gases [90] should display large GVD for millisecond-scale pulses. The GVD control is also easily extended to applications requiring larger bandwidth by using the broadband SBS technique, introduced in the previous chapters. Fano-type resonances in photonic crystal [91], plasmonic [92] and metamaterial [93] devices are also promising avenues to explore for high-bandwidth GVD engineering.

7

Forward SBS scattering in optical fiber

In this chapter, I return to the physics of the SBS process in optical fiber and report the observation of strong forward stimulated Brillouin scattering (FSBS) in a standard 2-km-long highly nonlinear fiber [94]. The interaction of two co-propagating optical beams arises from the coupling to the acoustic vibrations in the transverse direction, in contrast with the longitudinal acoustic waves in conventional backwards SBS. The strong FSBS coupling was previously considered inefficient due to the different confinement areas of the optical and acoustic waves. However, an especially large gain coefficient of 34.7 W^{-1} is observed at the resonance frequency of 933.8 MHz, which is explained by theoretical work as well. The forward SBS is an extension to the SBS theory presented in Ch. 2.

In this project, I am the leading contributor in design and setting up the experiment, deriving the theory and analyzing the data. Jing Wang has contributed equally in the experiment setup, data collection and analyzing. Dr. Rui Zhang has also contributed in the experiment setup and data collection. Professor Gauthier has conceived the experiment and supervised the overall project. We have summarized the results in

this chapter in reference [94].

An overview of forward SBS is presented in Sec. 7.1. The theory describing interaction of the light and radial acoustic fields are discussed in Section 7.2, where a model including optical Kerr effect is also presented. The experiment and measured FSBS resonance profiles are shown in Sec. 7.3. Additional discussion on FSBS linewidth trend are given in Sec. 7.4, and Sec. 7.5 is the conclusion.

7.1 Introduction of forward stimulated Brillouin scattering

Interactions between tightly confined optical and acoustic waves have attracted much research interest over the past few years [2, 8, 43]. As discussed in Ch. 2, stimulated Brillouin scattering is an efficient nonlinear light scattering process that has stimulated research interest. In the previous chapter, I emphasis on discussions on the backward SBS where the pump and the probe beams counter-propagate with each other so that phase-matching conditions can be fulfilled for the slowly-propagating acoustic wave. However, the acoustic dispersion relation Eq. 2.4 is true only for longitudinal waves in the waveguide [68]. When I include consideration of the transverse acoustic waves trapped in the cylindric optical fiber, new types of optical-acoustic coupling emerge [58, 64]. Such coupling enables the forward stimulated Brillouin scattering (FSBS) process, which involves the coupling between two co-propagating optical beams (signal beam with frequency ω_s and pump beam with frequency ω_p) with the so-called guided acoustic modes vibrating (with frequency Ω) in the radial direction, as shown in Fig. 7.1.

7.1.1 Guided acoustic mode in an optical fiber

The structure of an optical fiber, as shown in Fig. 2.1, consists of a small core, a larger cladding area, and an outer buffer layer [65]. In conventional optical fibers, the same material (silica) is used for both the core and the cladding. Slight doping in

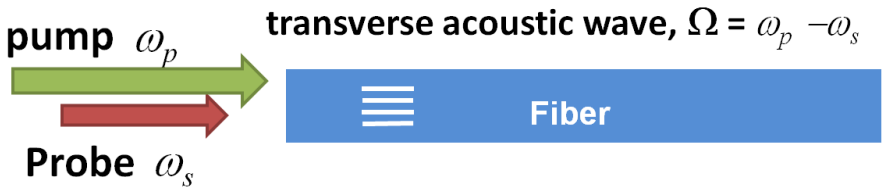

FIGURE 7.1: Forward stimulated Brillouin scattering in an optical fiber. The co-propagating optical beams are coupled to transverse vibrational modes in the optical fiber. The picture shows the signal beam on the Stokes side.

the core area induces refractive index difference to confine the optical field, but such doping does not substantially affect the mechanical properties of the core material. As a result, for acoustic waves, optical fiber is considered as an isotropic cylindrical bar throughout the core and the cladding area. Outside the cladding however, the buffer material (usually plastic) often strongly dumps acoustic waves, causing them to vanish very soon into this region. Thus, the buffer is usually treated as a hard boundary for the the acoustic waves.

Many possible acoustic vibrational modes exist in a cylindrical bar [95]. Figure 7.2 shows the density distribution of a longitudinal acoustic wave and a radial acoustic wave in a cylindrical structure. As shown in the figure, the longitudinal wave has a density distribution that varies only along the fiber axis, which I take as the z direction. The radial wave has a density variation along the r direction, which is confined inside the core and cladding area of the fiber with typical diameter of 125 μm. Due to this confinement, the radial acoustic wave has multiple discrete vibrational modes corresponding to different characteristic dispersion relations and density variation distributions. These radial modes are denoted as $R_{0(m)}$ where m is the mode number.

Note that the longitudinal mode and the radial modes are just two kinds of acoustic waves out of many possible vibrations for a cylindric structure. More complicated vibrations include 2-dimensional torsional modes and 3-dimensional flexural modes, usually having dispersion curves similar to those of the radial modes. There are re-

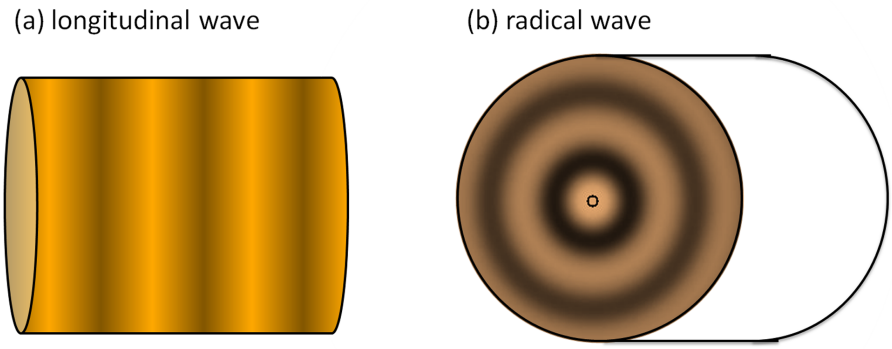

FIGURE 7.2: Acoustic longitudinal wave (a) and radial wave (b) in an optical fiber

ports on the observations of acoustic-optical coupling due to these higher dimensional modes [58, 59]. However, the coupling to the higher-dimensional modes in our experiment is much weaker than the radial modes. This is due to the fact that higher-order radial modes tend to concentrate into the center part of the cylindrical bar, and overlap with the optical field efficiently, and thus enhance the coupling strength.

7.1.2 Cascaded Forward SBS

In Sec. 2.2.2, I derive resonant frequency and wavevector using the energy and phase-matching conditions for the backward SBS process. In the FSBS process, the dispersion relation for a radial guided acoustic mode in an optical fiber is given by [64],

$$\Omega = \sqrt{(qv)^2 + \Omega_a^2}, \tag{7.1}$$

where $q(\Omega)$ is the wavevector (frequency) of the radial guided acoustic wave, Ω_a is a characteristic cutoff frequency at zero axial wavevector [64]. Combined with the optical dispersion relation given in Eq. (2.4), I solve for the energy and phase matching conditions in Eq. (2.3) and obtain the resonant frequency

$$\Omega \approx \Omega_a. \tag{7.2}$$

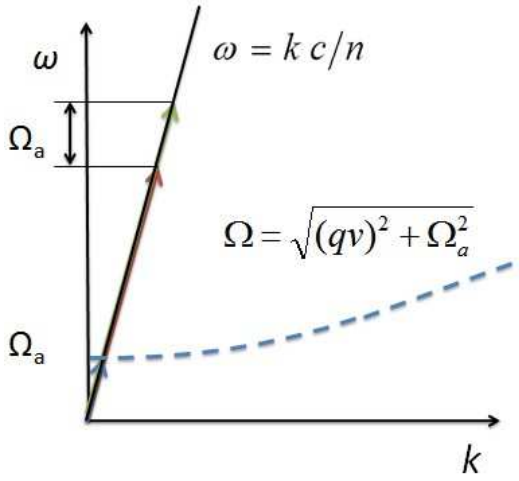

FIGURE 7.3: Energy and phase matching for forward SBS. The solid curve is the optical dispersion relation and the dashed curve is the radially guided acoustic wave dispersion relation. There is always an intersection between the two curves near the cutoff frequency Ω_a.

As shown in Fig. 7.3, the radial guided acoustic modes in an optical fiber typically have a flat dispersion curve starting from a characteristic cutoff frequency Ω_a at zero axial wavevector. The radial guided acoustic dispersion curve (dashed) intersects with the linear optical dispersion curve (solid) near the cutoff frequency Ω_a. I find that this dispersion relation allows automatic phase matching between the beat of the two co-propagating optical beams (frequency ω_p, ω_s) and the transverse acoustic excitation (Ω_a).

Since the resonant frequency is independent on the optical frequencies of the coupled beams, an acoustic wave with frequency Ω_a can be coupled to any co-propagating optical beam pairs with a frequency difference of Ω_a. As a result, cascaded generation of multiple Stokes and anti-Stokes beams with frequency-spacing of Ω_a [58, 63] is enabled. This is in contrast with the backward SBS, where the resonant frequency Ω_B is linearly dependent on the optical frequency of the pump beam ω_p. Moreover, the direction of the wavevector for the resonate longitudinal acoustic wave alternates between adjacent cascaded beam pairs in backward SBS processes. As a result, cascaded

backward SBS is not observed in optical fibers.

In addition to cascaded frequency generation, multiple transverse acoustic modes exist in typical optical fibers, corresponding to distinct modes of vibration, yielding a rich FSBS spectrum [57]. The rich spectrum of the FSBS process provide many interesting research topics such as high-speed optical delay using co-propagating pump beams [96].

7.1.3 Acoustic-optical overlap

In previous research on FSBS, Kang's work shows that the $R_{(0(m))}$ acoustic resonance enhances cascaded Stokes and anti-Stokes scattering [58, 63] in a phontonic crystal fiber, where the cladding is made of air so that the sounds is also confined in a small region. The claim is that the tight confinement of both light and sound waves in the small core of the PCF enables a large overlap between the fundamental transverse radial acoustic and optical modes, thereby enhancing the acousto-optical coupling efficiency and simultaneously increasing the FSBS resonance frequency up to the application-suitable gigahertz frequency range [59, 63]. On the other hand, because the radial acoustic waves $R_{0(m)}$ in standard single mode fibers (SMFs) are mainly confined in the fiber cladding (typical diameter 125 μm), these guided acoustic modes in SMFs tend to have a much wider spatial distribution than the core-confined optical field. For this reason, it is believed that coupling between guided acoustic waves and optical waves in SMFs is weak due to their partial spatial overlap [57, 58]. Likely for this reason, there has been little research on FSBS in standard single-mode fibers.

However, I observer strong FSBS in a standard 2-km-long highly-nonlinear fiber (HNLF, OFS Inc.) with a core/cladding diameter of 125 μm and an effective optical mode area of 11.5 μm^2. I observe multiple radially-guided acoustic resonances $R_{0(m)}$, with frequencies ranging from 80 MHz ($R_{0(2)}$) to 1.1 GHz ($R_{0(23)}$) limited by the frequency response of our detection scheme. Even though the acoustic waves are only

loosely confined in the larger cladding area, I find that good overlap between acoustic and optical modes is possible because the peak acoustic power is concentrated near the fiber core for larger m. For our 2-km-long HNLF, the gain coefficient is observed to be 34.7 W^{-1} at a frequency of 933.8 MHz (corresponding to $R_{0(20)}$) when pumped by a 1550-nm-wavelength continuous-wave pump beam with a power of 8 mW. This value is more than two times larger than that obtained by Kang *et al.* [58] for the $R_{0(1)}$ mode in a 10-m-long PCF. The pump power is limited in our case by the threshold for backward SBS, which could be suppressed using a pulsed pump beam. The line-shape of the FSBS resonances is studied for both the Stokes and anti-Stokes scattering processes.

I observe asymmetric gain profiles, especially for the anti-Stokes side, which is explained by interference between the optical Kerr effect and the FSBS process and agrees with the prediction of the analytic solution to the coupled equations. I also find a linearly increasing trend for the measured linewidth of the FSBS resonances from 425 MHz to 1.1 GHz for Stokes scattering.

7.2 Theoretical description of the FSBS and Kerr effect

In this section, I derive the coupled amplitude equations for the evolution of optical waves in an optical fiber where both FSBS and the Kerr effect are important.

7.2.1 Acoustic-optical coupling equation for the radial guided acoustic modes

In the cylindric coordinates z,r and φ, the interactions of the acoustic density variation $\rho(r,\varphi,z,t)$ and the optical field $E(r,\varphi,z,t)$ are described by the coupled equations Eq.

2.6 and Eq. 2.7 [68]

$$\frac{\partial^2 E}{\partial z^2} - \frac{n^2}{c^2}\frac{\partial^2 E}{\partial t^2} = \frac{1}{\epsilon_0 c^2}\frac{\partial^2 P^{NL}}{\partial t^2} \tag{7.3}$$

$$\frac{\partial^2 \rho}{\partial t^2} - (V_L^2 + \Gamma\frac{\partial}{\partial t})\nabla^2\rho = \nabla\cdot\overrightarrow{f} = -\frac{1}{2}\epsilon_0\gamma_e\nabla^2\overline{E^2}, \tag{7.4}$$

where the speed of sound v in Eq. 2.7 is the longitudinal acoustic velocity V_L. Here, we assume the optical wave propagates along the z-direction with slow variation along the polar coordinates r,φ.

Consider the interaction between a strong pump beam ω_p and a weak signal beam frequency downshifted by $\omega_s = \omega_p - \Omega$ with respect to the pump beam. In the FSBS process, it necessary to consider all possible cascaded Stokes and anti-Stokes fields with an equal frequency interval Ω generation via acoustic-optical coupling. A general form of the optical field in the fiber is thus given by

$$E(r,\varphi,z,t) = E_o(r,\varphi)\sum_j a_j(z,t)e^{i[(k-jq)z-(\omega_0-j\Omega)t]} + c.c., \tag{7.5}$$

where $E_p(r,\varphi)$ is the normalized transverse distribution of the optical fundamental (HE_{11}) mode, j is an integral representing the order of the cascaded optical fields in the fiber (negative j's refer to the Stokes fields, positive j's refer to the anti-Stokes fields, and $j=0$ refers to the pump beam), a_j is the slowly varying field amplitude of j^{th} order optical beam, $q(\Omega)$ is the propagation constant (frequency) of the acoustic phonon and $k - jq(\omega_0 - j\Omega)$ is the propagation constant (frequency) of the j^{th} order optical field.

We now consider the acoustic waves and the associated nonlinear polarization. In describing the acoustic wave, the nearly azimuthally symmetric radial profile of the HE_{11} mode is considered neglecting the small azimuthal dependence. Including a series of guided acoustic resonances generated over a broad frequency range for fibers

with a large cladding diameter [57], the density variation of the m^{th}-order acoustic phonons is given in the form of

$$\rho_m(r,\varphi,z,t) = \rho_{0(m)}(r) b_m(z,t) e^{i(q_m z - \Omega_m t)} + c.c., \tag{7.6}$$

where $q_m(\Omega_m)$ is the propagation constant (frequency) of the m^{th}-order acoustic phonons, and b_m is the slowly-varying acoustic amplitude and $\rho_{0(m)}$ is the normalized radial profile of the acoustic density variation of the m^{th} mode $\mathrm{R}_{0((m)}$, which is obtained by solving Eq. 2.7 without the source term

$$\nabla^2_{r,\varphi}\rho_0 - \omega^2\rho_0 = 0. \tag{7.7}$$

The solution is expressed by the Bessel Functions $\rho_{0(m)} \propto J_m(q_m r)$, with the dispersion relation given in Eq. (7.1) [97]. The mode number m represents the number of ripples in the cladding area.

The nonlinear polarization produced by the acoustic vibrations is given by Eq. (2.9) as $P_m = (\epsilon_0 \gamma_e/\rho_0)\rho_m$ [68]. Inserting Eqs. (7.5), (7.6) and the nonlinear polarization P_m into Eq. (7.3) and considering all acoustic modes, we find that the amplitude evolution of the j^{th}-order optical field a_j is described by

$$\frac{da_j}{dz} = \sum_m i(\gamma_{Am} a_{j-1} \sum_h a^*_{h-1} a_h + \gamma^*_{Am} a_{i+1} \sum_h a_{h-1} a^*_h), \tag{7.8}$$

where h is an integer representing the order of the optical fields. The FSBS coupling coefficient γ_{Am} is given by

$$\gamma_{Am} = \frac{\epsilon_0 \omega_0 \gamma_e^2 Q_{0(m)} Q_{1(m)}}{2nc\rho_0} \frac{1}{\Omega_m^2 - \Omega_{Am}^2 + i\Omega_m \Gamma_{Bm}}, \tag{7.9}$$

where $\Gamma_{Bm} = \Gamma\Omega^2_{Am}$ is the resonance linewidth, Ω_{Am} is the cutoff frequency for the m^{th}

radial mode, and the factors $Q_{0(m)}$ and $Q_{1(m)}$ take the form

$$Q_{0(m)} = \langle E_o^2, \rho_{0m} \rangle \equiv \int_0^{2\pi} \int_0^a E_o^2 \rho_{0m} r dr d\varphi, \tag{7.10}$$

$$Q_{1(m)} = \langle \nabla_\perp^2 E_o^2, \rho_{0m} \rangle \equiv \int_0^{2\pi} \int_0^a \nabla_\perp^2 E_o^2 \rho_{0m} r dr d\varphi. \tag{7.11}$$

The coupled equations (7.8) are solved for the case of a strong pump beam and a weak single Stokes sideband of the m^{th}-order. The output field amplitude is given by

$$a_m(L) = a_m(0) e^{g_{(m)} I_p/2} \approx a_m(0)(1 + g_{(m)} I_p/2), \tag{7.12}$$

where L is the length of the optical fiber. The line-center gain parameter of the m^{th}-order FSBS Stokes resonance is given by

$$g_{0(m)} = \frac{\omega_0 \gamma_e^2 |Q_{0(m)} Q_{1(m)}|}{2n^2 c^2 \rho_0 \Gamma_{Bm} \Omega_{Am}}, \tag{7.13}$$

and the gain coefficient $g_{(m)}$ is given by $g_{(m)} = g_{0(m)} L$. The approximation is valid for small gain $g_{(m)} I_p/2 \ll 1$.

We see that the magnitude of $g_{0(m)}$ in Eq. (7.13) is determined by the factors $Q_{0(m)}, Q_{1(m)}$ and linewdith Γ_{Bm}. I will discuss acoustic damping mechanisms and linewidth Γ_{Bm} in greater detail in Sec. 7.4. Now first take a look at the factors $Q_{0(m)}, Q_{1(m)}$, which represent the ability of the optical field to generate the acoustic excitation and for the acoustic excitation to scatter the incident field, respectively. The profiles of the acoustic density variation $\rho_{0(m)}(r, \varphi)$ for different modes overlap with the optical field quite differently. As a result, the values of the corresponding $Q_{0(m)}$ and $Q_{1(m)}$ vary substantial for different modes.

We plot in Fig. 7.4 the spatial distribution in the r direction of the acoustic modes and optical mode in a HNLF fiber. The optical field $E(r, \varphi)$ is determined by solving the boundary condition problem for the optical fundamental mode distribution [65].

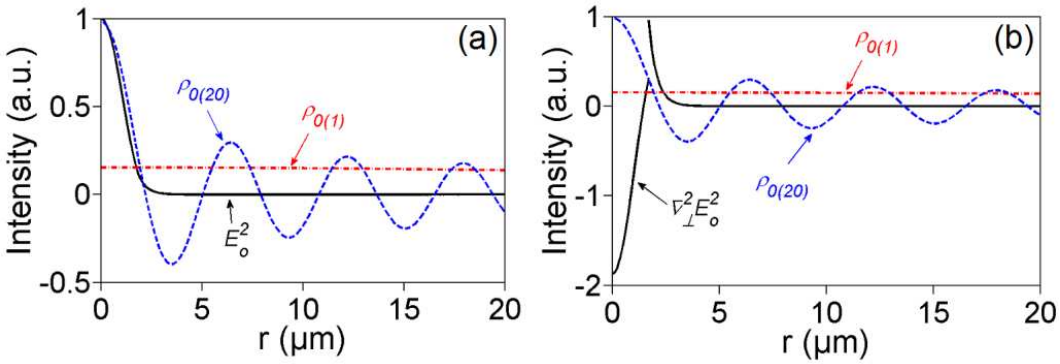

FIGURE 7.4: (a) Intensity of the fundamental optical HE_{11} mode (black line) and the density variation of the acoustic mode $R_{0(1)}$ (red dash and dot line) and $R_{0(20)}$ (blue dash line). (b) The transverse second derivative of the intensity of the fundamental optical mode (black line) and the density of acoustic mode $R_{0(1)}$ (red dashed and dotted line) and $R_{0(20)}$ mode (blue dashed line). The parameters for silica fibers are [19, 97]: $\gamma_e = 1.17$,$\rho_0 = 2.20 \times 10^3$ kg/m^{-3} , $V_L = 5590$ m/s. Also, we use $\epsilon_0 = 8.85 \times 10^{-12}$ F/m and $\omega_0 = 2\pi \times 193.5$ THz for 1550 nm laser beam. As I will discuss in Sec. 7.2, Γ_{Bm} is a slowly increasing function of Ω_{Am} and is approximately equal to $2\pi \times 7.5$ MHz over the range of our experiment

The acoustic field $\rho_{0(m)}(r, \varphi)$ is plotted for the fundamental mode $m = 1$ mode and for $m = 20$. As clearly shown in the figure, the fundamental radial acoustic mode extends over all the cladding area, and thus poorly overlaps with the core-concentrated optical field. However, as the mode number increases, the acoustic density variations get more and more concentrated into the first ripple around the core area. The overlap between the optical field and the acoustic field is substantially increased for $m = 20$, where the first ripple of the acoustic wave overlaps with the core area.

As expected, the calculated value for $Q_{0(m)}$,$Q_{1(m)}$ is substantially larger for mode $R_{0(20)}$ (with resonant frequency $\Omega_{A(20)}$ =933.8 MHz) than for mode $R_{0(1)}$ (with resonant frequency $\Omega_{A(1)}$ =30 MHz) in the HNLF. In fact, $Q_{0(20)} \sim 4Q_{0(1)}$ and $Q_{1(20)} \sim 150Q_{1(1)}$ according to calculation. The FSBS gain parameters induced by these two modes are given by $g_{0(1)} = 2.1 \times 10^{-3}$ W^{-1}m^{-1} and $g_{0(20)} = 2.4 \times 10^{-2}$ W^{-1}m^{-1}. And the gain coefficient g_m is found to be 48 W^{-1} for $m = 20$ in a 2-km HNLF. This prediction is three times larger than the experimentally observed value obtained in a 10-m-long

small-core PCF (15 W^{-1}) previous reported by Kang *et al.* [58].

7.2.2 Including Kerr nonlinearity

In the experiment of FSBS, I also observe the interplay with Kerr effect. This is because the HNLF used in the FSBS experiment has a high nonlinear coefficient γ_l and a flat dispersion curve that phase matches any nonlinear process for wavelengths around 1550 nm. As a result, strong Kerr nonlinearity occurs in the HNLF and it is necessary to include the interference from the Kerr effect in the model for the evolution of optical waves. The Kerr effect couples Stokes and anti-Stokes sidebands via parametric amplification (also known as four-wave mixing, as discussed in Ch. 2.1.2). Considering only the nonlinear process due to the Kerr effect, I find that the evolution of the slowly varying field amplitude is described by [68]

$$\frac{da_j}{dz} = i\gamma_K[(|a_j|^2 + 2\sum_{p\neq j}|a_p|^2)a_j + (2\sum_{p,q,l\neq i;p+q-l=j} a_p a_q a_l^* e^{i\theta_{pql}} + \sum_{p,q\neq i;2p-q=j} a_p^2 a_q^* e^{i\theta_{pq}})] \tag{7.14}$$

where p, q, l, j are integers representing the order of the optical fields. The Kerr coefficient γ_K is denoted by $\gamma_K = (2n\epsilon_0 c)\gamma_I$ with nonlinear coeffecient $\gamma_I = 11.7$ $km^{-1}W^{-1}$ for the HNLF. Because of the small frequency difference between the pump and the sidebands (on the order of 1 GHz) and the near-zero dispersion of our HNLF at 1550 nm, the parametric processes are phase matched. Thus, we take $\theta_{pql}, \theta_{pq} \approx 0$.

Now consider both the FSBS and Kerr effect in the HNLF and describe the evolution of the optical field amplitudes by combining both Eq. (7.8) and (7.14). We have a set of coupled evolution equations for the optical field, where each of the cascaded Stokes/anti-Stokes beams are coupled to every other order in the series.

Solutions can be find for the case where the Stokes and anti-Stokes beams are weak compared to the pump beam. In the non-depleted-pump condition, energy transferred out of the pump beam is small. In this case, the higher-order Stokes and anti-Stokes

beams are much weaker than the first-order beams and thus can be ignored. The nonlinear coupled equations are simplified to a set of equations governing only the amplitudes of the first-order Stokes wave a_{-1} and the anti-Stokes wave a_1. The coupled equations are given by

$$\frac{da_{-1}}{dz} + \frac{\alpha}{2}a_{-1} = i\sum_m(\xi_m a_{-1} + \kappa_m a_1^*), \tag{7.15}$$

$$\frac{da_1}{dz} + \frac{\alpha}{2}a_1 = i\sum_m(\xi_m^* a_1 + \kappa_m^* a_{-1}), \tag{7.16}$$

where $\xi_m = |a_0|(\gamma_{Am}^* + 2\gamma_K)$ and $\kappa_m = a_0^2(\gamma_{Am}^* + \gamma_K)$ are coupling coefficients for each acoustic mode m,α is the fiber loss and a_0 is the amplitude of pump, which I take as a real constant without loss of generality.

Equation (7.15) is a pair of coupled equations that describe comprehensively the evolution of the optical waves inside the HNLF. When considering the initial condition $a_{-1}|_{t=0} = a_{-1}(0)$ and $a_1|_{t=0} = 0$, and ignoring the fiber loss ($\alpha = 0$) the solution to Eqs. (7.15)and (3.15) are given by

$$a_{-1}(z) = a_{-1}(0)[\cosh(s_m z) + i\frac{\xi_m}{s_m}\sinh(s_m z)], \tag{7.17}$$

$$a_1(z) = i\frac{\xi_m^*}{s_m^*}a_{-1}^*(0)\sinh(s_m^* z), \tag{7.18}$$

where $s_m = \sqrt{\kappa_m^2 - \xi_m^2}$.

The result is used to describe FSBS without the Kerr effect by setting $\gamma_K = 0$, where

$$a_{-1}(z) = a_{-1}(0)(1 + i\xi_m z), \tag{7.19}$$

$$a_1(z) = ia_{-1}^*(0)\kappa_m^* z. \tag{7.20}$$

The power of each frequency component is given by $P_k = 2n_{\mathtt{eff}}\epsilon_0 c|a_k|^2$. Using this definition and Eq. (7.19), the optical powers are $P_{-1(z)} = P_{-1(0)}[1 + 2a_0^2\,\mathtt{Im}(\gamma_{Am})z +$

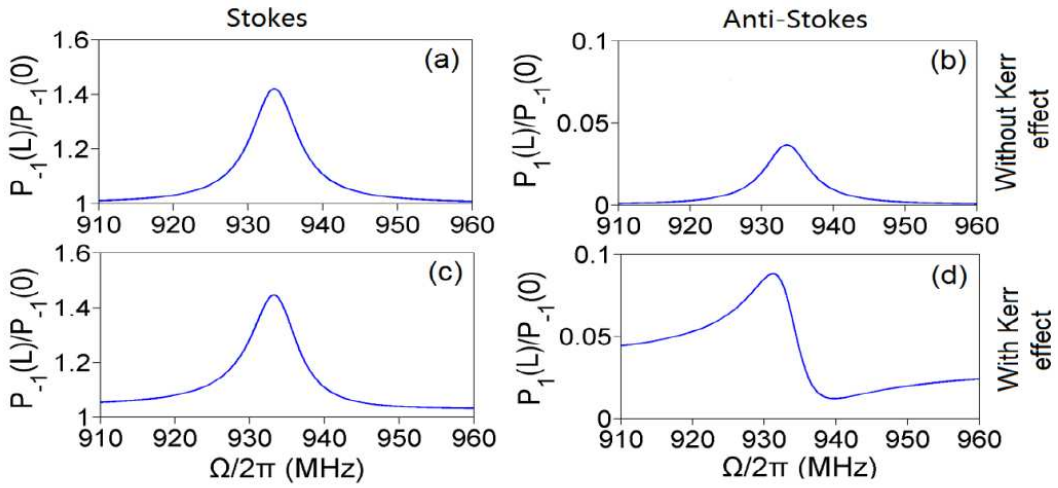

FIGURE 7.5: Frequency dependence of the Stokes/anti-Stokes gain near the $R_{0((20)}$ resonance at 933.8 MHz. Stokes beam gain without (a) and with (c) the Kerr effect. Anti-Stokes gain without (b) and with (d) the Kerr effect.

$a_0^4|\gamma_{Am}^2|z^2]$ and $P_{1(z)} = P_{1(0)}a_0^4|\gamma_{Am}^2|z^2$. We notice that the FSBS coefficient is a function of frequency Ω_m in Eq. (7.9), so that both $P_{-1(L)}$ and $P_{1(L)}$ have Lorentzian shapes owing to the term $(\Gamma_{Bm}/2)^2/[\Delta\Omega^2 + (\Gamma_{Bm}/2)^2]$ in $\mathrm{Im}(\gamma_{Am})$ and $|\gamma_{Am}|^2$ of Eq. (7.17) with $\Delta\Omega = \Omega_m - \Omega_{Am}$.

We determine the output gain spectrum of the Stokes and anti-Stokes beams with and without the Kerr effect using Eqs. (7.17) and (7.19), as shown in Fig. 7.5. The power of the Stokes and anti-Stokes beams are normalized to the input power of the Stokes beam $P_{-1}(0)$. The lineshapes at both the Stokes and anti-Stokes frequencies are Lorentzian without the Kerr effect, as discussed above. However, the lineshapes become asymmetric due to the contribution of the Kerr effect to the coupling coefficients. The Kerr coefficient γ_K is pure real and its contribution to ξ_m is 2 times larger than to $\varkappa_m$, explained by the nonlinear phase evolution along the fiber. It is also observed that the Kerr nonlinearity distorts the anti-Stokes resonance more than the Stokes resonance, which is due to the absence of an initial anti-Stokes beam. The experiment results shown in the next section are consistent with these theoretic expectations.

7.3 Experiment and results

In the experiment, I use a dual-module Mach-Zender Modulator (DMZM) to generate both the pump and the probe beams. A electrical sinusoid wave and its 90 degree phase-shifted version are feed into the two modules of the DMZM respectively. In this way, a single-frequency optical sideband is generated with a frequency shift equal to the modulation wave frequency. The frequency difference of the carrier and sideband stays stable even if the source DFB laser experience a frequency drift, and enables accurate measurement of the FSBS bandwidth.

To spectrally resolve the probe beam and the pump beam separately, we generate a reference beam from the same laser source using a single-module Mach-Zender modulator (SMZM) and measured the beat signal arising from their interference. By shifting the frequency of the reference beam away from the pump beam, I am able to measure the Stokes and anti-Stokes signals separately. The setup is shown in Fig. 7.6.

In the experiment, I scan the probe beam frequency by changing the modulating electric wave frequency and measure the magnitude of the beat signal between the probe and the reference beam. In this way, we are able to resolve the FSBS resonance spectrum. It is desirable to increase the pump power as high as possible for large FSBS gain. However, once the input power reaches the backward SBS threshold, the intensity of the pump beam becomes depleted, thus causing the FSBS gain to saturate [44]. As a result, I launched a maximum pump power of 8 mW into the fiber, which is the measured backward SBS threshold for our HNLF. This limitation can be avoided using a pulsed pump beam with pulse duration <10 μs. In doing that, the spatial pulse width is smaller than the fiber length. As a result, the spatial overlap between the pump beam and the backward SBS signal beam is reduced.

The gain spectra of the first-order Stokes and anti-Stokes beams are shown in Fig. 7.7, with the theoretical prediction of Eq. (7.15) considering the fiber loss (0.76

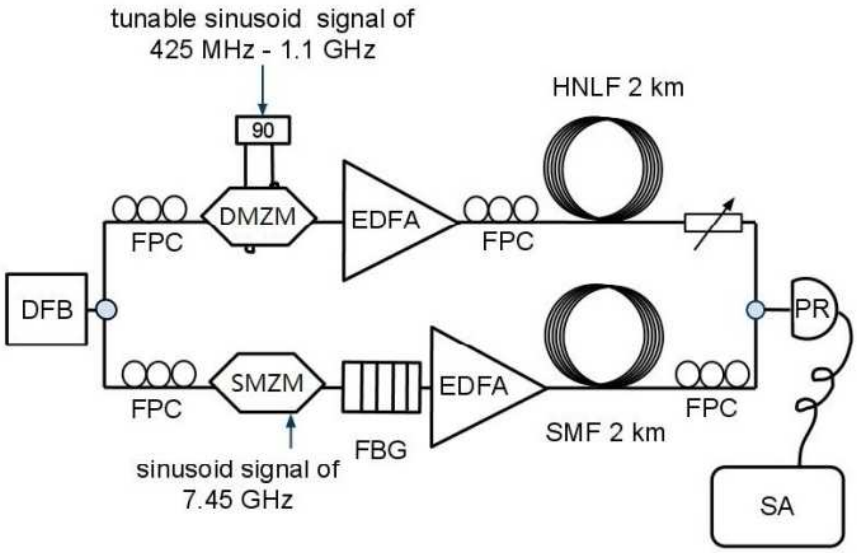

FIGURE 7.6: The experiment setup of FSBS in HNLF. DMZM, dual-module Mach-Zender modulator; SMZM, single-module Mach-Zender modulator; EDFA, erbium-doped fiber amplifier; FBG, fiber Bragg grating; FPC; fiber polarization controllers; PR, photoreceiver; SA, electronics spectrum analyzer. Seed beam from a DFB laser is modulated by a DMZM (FTM7921ER, Fujitsu, Inc). Sinusoid signals from an electric signal generator are split into two sine waves with a 90° phase difference. Modulation of the two optical paths in the DMZM with these electrical signals results in the generation of a single sideband beam whose frequency is shifted from the carrier beam by the sine-wave frequency. Because both the probe and the pump beams are generated from a same laser, their relative frequency does not jitter. The pump and the probe beams are then injected into the 2-km HNLF and interact via the FSBS process. Another part of the beam from the DFB laser is modulated by a SMZM (EO SPACE Inc.). The bias voltage of the SMZM is set to suppress the carrier frequency and I filter out one of the sidebands using a fiber Bragg grating (bandwidth 0.19 nm). The other sideband is then amplified and goes through a 2-km-long single mode fiber (SMF) for optical path balancing, and then it is mixed with the pump beam and the probe beam. A 12-GHz fast photoreceiver is used detect the interference and an electric spectrum analyzer resolves the beat signal.

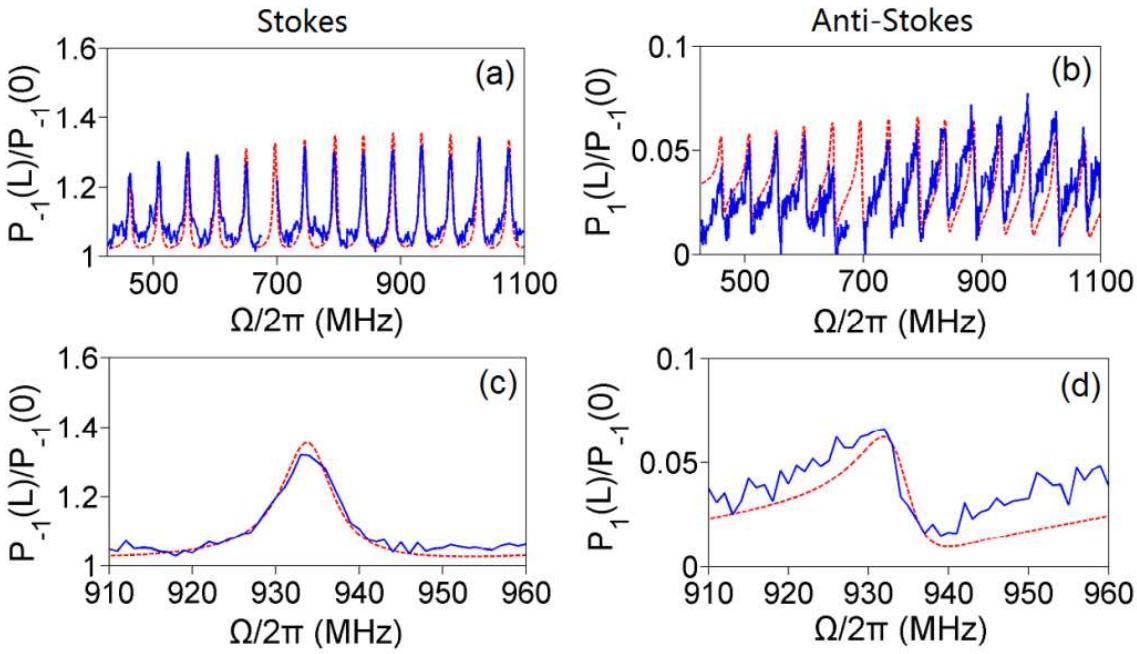

FIGURE 7.7: FSBS Stokes and anti-Stokes gain spectra with a pump power of 8 mW. Blue solid line is experimental results and red dashed line is theoretical simulation.

dB/km at 1550 nm) in solving the coupled amplitude equations. I observe a series of resonance peaks corresponding to the acoustic frequencies in the experiment from 425 MHz to 1.1 GHz (the discontinuity at 700 MHz is due to the operation gap for the two 90° phase shifters). The measured resonance frequencies show good agreement (root-mean-square error=0.36 MHz) with the numerical predictions, as shown in Table 7.1, where I adjust the fiber diameter to 127 μm to find the best agreement.

The FSBS Stokes gain $G = P_{\mathrm{out}}/P_{\mathrm{in}}$ (signal output power $P_{\mathrm{out}} = P_{-1}(L)$ for Stokes beam and $P_1(L)$ for anti-Stokes beam, signal input power $P_{\mathrm{in}} = P_{-1}(0)$) is found to be 1.32 at the resonant frequency of 933.8 MHz with a pump power of 8 mW, giving a gain coefficient of 34.7 W^{-1}, which agrees with the simulated prediction in Fig. 7.7(c). The spectra in Fig. 7.7(a) also clearly shows that G for the Stokes beam is a function of the acoustic mode number, taking on its largest value in the gigahertz range where the acousto-optical coupling is maximized. The linewidth is also different

Table 7.1: Measured and calculated FSBS resonant frequencies in the NHLF. A cladding diameter of 127 μm is used in the calculation.

Mode number m	11	12	13	14	15	16	17	18
Experiment $\Omega_{Am}/2\pi$ (MHz)	462.2	508.2	555	602.8	650	745	792.1	839.5
Theory $\Omega_{Am}/2\pi$ (MHz)	460.7	508.1	555.4	602.7	650	744.6	791.9	839.2
Mode number m	19	20	21	22	23	24	25	26
Experiment $\Omega_{Am}/2\pi$ (MHz)	886.5	933.8	980.3	1026.5	1074.3	1121.3	1169.5	1216.4
Theory $\Omega_{Am}/2\pi$ (MHz)	886.5	933.8	981.1	1028.4	1075.6	1122.9	1170.2	1217.5

for each resonances, showing that the mode number also affects the FSBS resonance bandwidth, as discussed below. The measured largest gain appears at the frequency of 933.8 MHz (corresponding to mode $R_{0(20)}$), agreeing with theoretical prediction. A separate calculation corresponding to the parameters for standard single mode fiber (SMF-28) reveals that the largest gain occurs for the $R_{0(8)}$ mode at 275 MHz with a much smaller gain ($\gamma_{0(8)} = 8\times10^{-3}$ m^{-1}W^{-1}) [58], demonstrating that a small change in core size as in our HNLF gives rise to a large increase in G. The fact that I observe good agreement between theory and experiment indicates that ignoring the difference in acoustic velocities in the core and cladding is a reasonable assumption.

7.4 Linewidth discussion

Figure 7.8(a) shows the measured Stokes beam resonance around the acoustic frequency 933.8 MHz. A Lorentzian fit yields a linewidth of 7.5 MHz (full width at half maximum or FWHM). In this way, I measure the linewidth of the FSBS resonances in the frequency range from 425 MHz to 1.1 GHz. Figure 7.8(b) shows the dependence of Γ_{Bm} on the acoustic frequency. The results are fit to a linear model given by

$$\Gamma_{Bm} = 2\pi \times [0.004(\Omega_m/2\pi) + 4.2\ (\mathrm{MHz})], \tag{7.21}$$

with a reduced chi-square value of 0.35 MHz.

The linewidth of the FSBS resonances depend on the various acoustic damping mechanisms in the HNLF, mainly depend on the material, structure and deformations.

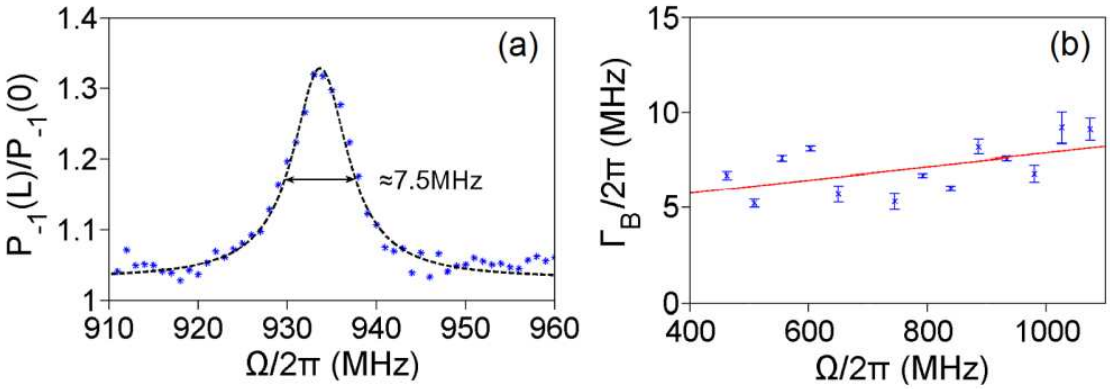

FIGURE 7.8: (a) The spectrum of the Stokes resonance for FSBS at 933.8 MHz. Experiment data are shown as blue dot and black dash line is the Lorentzian fitting. The linewidth is $\sim$ 7.5 MHz at frequency 933.8 MHz. (b) Measured linewidth (blue dot) of the FSBS resonances from 425 MHz to 1.1 GHz, linear fitting is shown in red line.

I classify the contributions to the linewidth by an inhomogeneous term, a viscosity damping term, and a surface damping term [98]

$$\Gamma_{Bm} = \Gamma_{\mathtt{inhomo}} + \Gamma_{\mathtt{viscosity}} + \Gamma_{\mathtt{surface}}, \tag{7.22}$$

respectively. The inhomogeneous term comes from structural non-uniformities along the fiber length, which plays an important role in the 2-km HNLF. The variation of the fiber diameter $\delta\phi$ causes a change in the acoustic mode frequency and hence broadens the resonance linewidth. As shown in Ref. [58], $\Gamma_{\mathtt{inhomo}} = (\delta\phi/\phi)\Omega_m$. The first term in Eq. (7.21) accounts for this effect. The coefficient of the linear parameter is consistent with the specified variation in the fiber cladding diameter of ± 0.5 μm.

The bulk viscosity damping term $\Gamma_{\mathtt{viscosity}}$ is inversely related to the viscosity lifetime $\tau_{\mathtt{viscosity}}$ of acoustic phonons [99]. This term is likely to be a small contribution to the total linewidth in HNLFs. Previous estimation of the viscosity damping contribution is on the order of 100 kHz [58, 98], much smaller than the non-uniformity term. Therefore, I neglect this term for the HNLF.

Damping due to acoustic absorption at the surface between the cladding and the plastic fiber jacket is another important contribution in our HNLF. For protecting the

fiber, there is a soft polymer coating between the cladding and air, which strongly damps acoustic vibrations [58]. Damping of the acoustic radiation as it passes into the polymer coating only depends on the radial displacement, which is nearly constant for higher-frequency modes [95, 98]. As a result, $\Gamma_{\texttt{surface}}$ is nearly a constant, and is determined to be $2\pi \times 4.4 \pm 0.3$ MHz from the experimental fit. Based on this scaling, I conclude that the dominant contribution to the linewidth is structural non-uniformities along the fiber and surface damping due to the fiber jacket.

7.5 Conclusion

I observe strong FSBS in a 2-km-long HNLF pumped by a monochromatic pump beam with a power of 8 mW. Although the coupling efficiency of the optical and acoustic fields was considered low due to poor spacial overlapping, I verify both experimentally and theoretically that the spacial overlapping improves for higher order acoustic vibration modes, which leads to strong FSBS resonances at gigahertz range. A large FSBS gain coefficient of 34.7 W^{-1} is obtained at the frequency of 933.8 MHz. Other than that, multiple acousto-optical resonant peaks are observed for both the first-order Stokes and the anti-Stokes beams. The resonant frequencies of the FSBS process for the Stokes beams extend from 80 MHz (corresponding to $R_{0(2)}$ to 1.1 GHz (corresponding to $R_{0(23)}$), limited by the bandwidth of our detection method. Our results agree well with the predicted frequencies of the guided acoustic modes trapped in the fiber. The observed FSBS gain profile is well explained by the theory of the field evolution in the HNLF, where both FSBS and the Kerr effect are considered. The analytical solutions for the coupled equations are obtained, which explains the observed asymmetric resonances and is especially pronounced for the anti-Stokes resonances. I also find a linear increasing trend of the linewidth for the FSBS resonances, which is accounted for by contributions from the structural non-uniformities along the fiber

and surface damping. The results open up new possibilities for FSBS in standard fibers for applications such as slow and fast light [96].

8

Conclusions and outlook

8.1 Conclusions

In this thesis, we introduce the all-optical control of the group velocity in optical fibers using the nonlinear process of stimulated Brillouin scattering. We include both the fundamental theory of the nonlinear coupling between acoustic and optical waves in a cylindrical waveguide (optical fiber) and the applications of group velocity control in a slow-light optical buffer and a large group velocity disperser. The most salient results in this thesis can be summarized as follows:

- Backward SBS and application in group velocity control.

  In the fundamental theory part, we derive an equation for the wavevector experienced by the signal beam under the modulation of SBS resonances, and demonstrate the tailoring of the wavevector profile using multi-line and broadband pump beams. As one of the earliest groups to demonstrate the fundamental principles for spectrally tailored SBS-based group velocity control, our work has made SBS slow light a very popular research topic in the recent years, giving rise to many interesting applications.

Among the SBS slow light applications, one of the most important is the broadband optical buffer. We are among the groups that first demonstrate broadband optical buffer with 10's of GHz bandwidth. In addition, we design the profile of the SBS and obtain an optimized shape for optical buffer performance. In the broadband optical buffer, we use a broadband pump beam with tailored spectrum profile to generate a flat-topped SBS gain profile, which minimizes the pulse distortion and improves the delay. Particularly, we develop a novel method of noise current modulation that jitters the frequency of the pump beam on a fast temporal scale of sub-ns, making the pump beam truly broadband even for fast decaying phonons on the ns scale. The fast noise modulation method significantly stabilizes the SBS gain and improves the signal fidelity. Using this method, we obtain a tunable fractional pulse delay up to 1 and a peak signal to noise ratio of 5.2.

We also find in a broadband SBS slow light buffer that modulation instability is the dominate competing effect in an anomalously dispersive LEAF fiber. The modulation instability depletes the power from the pump beam and limits the SBS gain-bandwidth product to 126 dB·GHz. This is the first report of the modulation instability competing in a broadband SBS system.

We demonstrate the generation of a giant group velocity dispersion using SBS in optical fibers. This is the first demonstration of all-optical control of group velocity dispersion using SBS and a series of future work is expected to follow. In the GVD experiment, we place a gain resonance next to an absorption resonance to produce a slope for the group velocity. The SBS profile is tailored so that the GVD parameter is roughly constant over the spectrum range of Γ_B. We obtain a large GVD parameter of 7.5 ns^2/m, which is 10^9 larger than the value of a single-mode fiber. The large GVD enables dispersion of a ns optical pulse, which

is far beyond the scope of other GVD techniques. The technique of GVD control can be applied to any wavelength that is transparent in optical fibers and offers a wide range of tunability.

- Forward SBS observation and characterization.

  Based on the derivation of backward SBS, we extend the basic SBS theory to describe the observed efficient forward SBS resonances in a highly nonlinear fiber, where Kerr nonlinearity plays an important role. We find in a highly nonlinear optical fiber that a strong resonance occurs at 933 MHz with a large gain coefficient of 34.7 W^{-1}. This is due to a good overlap between the guided radial acoustic and optical waves in the single mode fiber, despite the fact that the acoustic wave is only loosely confined in the cladding area while the optical wave is tightly confined in the central core. We also find that the Kerr effect induces asymmetry to the SBS resonance profiles and enhances the anti-Stokes beam via 4WM. This finding revokes the previous ideal that FSBS is inefficient due to lack of overlap between acoustic and optical fields in single mode fibers, and opens up possibility for FSBS applications in inexpensive commercial optical fibers.

8.2 Outlook

There are many possible future directions for the work presented here. For example, group velocity can also be controlled using FSBS. In FSBS, since the pump beam travels with the signal beam, changes in the pump beam power will immediately be reflected onto the signal beam, enabling faster controlling. A pulsed pump beam can also be used to modulate the pulsed signal beam to lower the power requirement. Moreover, by utilizing the depletion of the pump pulse, logic operations can be built based on the interplay between the pump pulse and the signal pulse.

Moreover, the noise current modulation techniques applied to the broadband SBS optical buffer in Chs. 5 and 6 can be immediately applied to SBS-based GVD control described in Ch. 4. This technique will allow for complete control of GVD in optical materials over a wide range of pulse parameters. For the SBS-based GVD investigated here, the resonances can be broadened to the 10's of GHz range by tailoring the pump spectrum [9, 16, 42], thereby realizing large GVD for pulses from the nanosecond to the sub-100-ps range. It will also be interesting to characterize the pulse distortion and data fidelity for such a tunable GVD system.

Finally, there is sustained progress in realizing chip-scale SBS-based devices [100–102] which will allow compact slow light and dispersive devices. In the quantum regime, it will be possible to delay and disperse single-photon wavepackets without adding excess noise if the SBS device is cooled to its quantum mechanical ground state, which is now within reach [103].

Appendix A

Operation principles of a Mach-Zehnder modulator

Mach-Zehnder modulator is a electro-optic modulator that converts electric signals into optical intensity variations. Mach-Zehnder modulators use nonlinear materials that exhibit electro-optic effect to modulate optical waves. A commonly used nonlinear material in Mach-Zehnder modulators is the $LiNbBO_3$ crystal, which demonstrates Pockles effect and changes its refractive index with the applying of an electric field. In the operation range, the refractive index change is proportional to the applied electric voltage. As a result, the phase of the optical waves transmitted through the crystal can be modulated by the electric voltage applied. This phase modulation transmission path is duplicated with the applied voltage sign flipped, and these two optical paths are combined to form a Mach-Zehnder interferometer, as shown in Fig. A.1.

An input optical field E_0 is first split into two waves with amplitude $E_0/2$. After propagation in the crystals, the split waves pick up a phase φ with opposite signs. The phase modulated waves are then combined at the output. The output wave E is given by

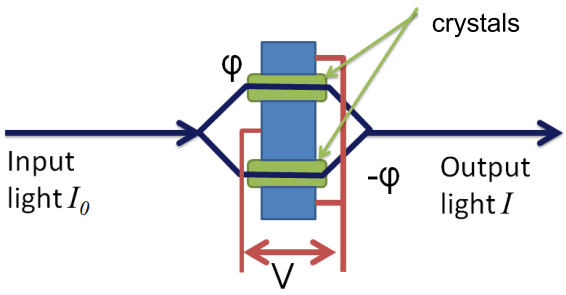

FIGURE A.1: Configuration of a zero-chirp Mach Zenhder modulation

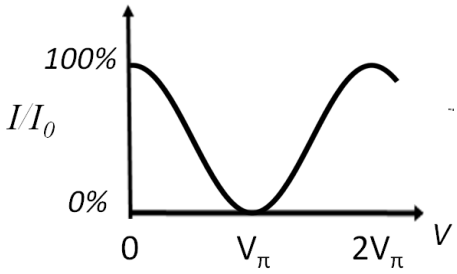

FIGURE A.2: Transmission of a MZM as a function of applied voltage

$$E = E_0/2\exp(i\varphi) + E_0/2\exp(i\varphi) = E_0\cos(\varphi). \tag{A.1}$$

And the output intensity I is given by

$$I = I_0\cos^2(\varphi). \tag{A.2}$$

The transmission of a MZM oscillates with φ. Because the phase modulation φ is proportional to the applied electric voltage, the intensity of the MZM output optical beam is controlled by the applied voltage. The proportionality is expressed by $\varphi = \pi V/(2V_\pi)$, where V_π is the characteristic voltage for the MZM to go from full open to full close, as shown in Fig. A.2.

An electric signal sequence is encoded onto the optical beam with high fidelity if the voltage levels corresponding to the "0" and "1" are set to the close and open points of the MZM. In this case, small fluctuations of voltage barely change the transmission of the MZM. This encoding scheme is used in the generation of signal pattern sequence in Chap. 5 and 6.

Bibliography

[1] L.V. Hau, S.E. Harris, Z. Dutton, and C.H. Behroozi. Light speed reduction to 17 metres per second in an ultracold atomic gas. *Nature*, 397:594–598, 1999.

[2] Z. Zhu, D.J. Gauthier, and R.W. Boyd. Stored light in an optical fiber via stimulated Brillouin scattering. *Science*, 318(5857):1748–1750, 2007.

[3] L. Thévenaz. Slow and fast light in optical fibres. *Nature Photonics*, 2(8):474–481, 2008.

[4] R.W. Boyd and D.J. Gauthier. Controlling the velocity of light pulses. *Science*, 326(5956):1074–1077, 2009.

[5] D.J. Gauthier, A.L. Gaeta, and R.W. Boyd. Slow Light: From Basics to Future Prospects - How can the speed of light be reduced a millionfold, and why does this matter? The answers to these questions are intriguing and important. *Photonics Spectra*, 40(3):44–51, 2006.

[6] D.R. Smith and N. Kroll. Negative refractive index in left-handed materials. *Physical Review Letters*, 85(14):2933, 2000.

[7] M.D. Stenner, D.J. Gauthier, and M.A. Neifeld. The speed of information in a fast-light optical medium. *Nature*, 425(6959):695–698, 2003.

[8] Y. Zhu, E. Cabrera-Granado, O.G. Calderon, S. Melle., Y. Okawachi, A.L. Gaeta, and D.J. Gauthier. Competition between the modulation instability and stimulated Brillouin scattering in a broadband slow light device. *Journal of Optics*, 12(10):104019, 2010.

[9] Y. Zhu, M. Lee, M. Neifeld, and D.J. Gauthier. High-fidelity, broadband stimulated-brillouin-scattering-based slow light using fast noise modulation. *Optics Express*, 19(2):687–697, 2011.

[10] Y. Zhu, J.A. Greenberg, N.A. Husein, and D.J. Gauthier. Giant all-optical tunable group velocity dispersion in an optical fiber. in preparation.

[11] V.R. Almeida, C.A. Barrios, R.R. Panepucci, and M. Lipson. All-optical control of light on a silicon chip. *Nature*, 431(7012):1081–1084, 2004.

[12] S.R. Friberg, Y. Silberberg, M.K. Oliver, M.J. Andrejco, and M.A. Saifi. Ultrafast all-optical switching in a dual-core fiber nonlinear coupler. *Applied Physics Letters*, 51:1135–1137, 1987.

[13] R.S. Tucker, P.C. Ku, and C.J. Chang-Hasnain. Slow-light optical buffers: Capabilities and fundamental limitations. *Journal of Lightwave Technology*, 23(12):4046, 2005.

[14] L. Xing, L. Zhan, L. Yi, and Y. Xia. Storage capacity of slow-light tunable optical buffers based on fiber Brillouin amplifiers for real signal bit streams. *Optics Express*, 15(16):10189–10195, 2007.

[15] H.J. Caulfield and S. Dolev. Why future supercomputing requires optics. *Nature Photonics*, 4(5):261–263, 2010.

[16] Z. Zhu, A.M.C. Dawes, D.J. Gauthier, L. Zhang, and A.E. Willner. Broadband SBS slow light in an optical fiber. *Journal of Lightwave Technology*, 25(1):201–206, 2007.

[17] Z. Zhu, D.J. Gauthier, Y. Okawachi, J.E. Sharping, A.L. Gaeta, R.W. Boyd, and A.E. Willner. Numerical study of all-optical slow-light delays via stimulated Brillouin scattering in an optical fiber. *Journal of the Optical Society of America B*, 22(11):2378–2384, 2005.

[18] E. Cabrera-Granado, O.G. Calderon, S. Melle, and D.J. Gauthier. Observation of large 10-Gb/s SBS slow light delay with low distortion using an optimized gain profile. *Optics Express*, 16(20):16032–16042, 2008.

[19] G.P. Agrawal. *Nonlinear fiber optics*. Academic Press, 4th edition, 2009.

[20] R.Y. Chiao, C.H. Townes, and B.P. Stoicheff. Stimulated Brillouin scattering and coherent generation of intense hypersonic waves. *Physical Review Letters*, 12:592–595, 1964.

[21] E. Garmire and C.H. Townes. Stimulated Brillouin scattering in liquid. *Applied Physics Letters*, 5(4):84–86, 1964.

[22] Y. Aoki, K. Tajima, and I. Mito. Input power limits of single-mode optical fibers due to stimulated Brillouin scattering in optical communication systems. *Lightwave Technology, Journal of*, 6(5):710–719, 1988.

[23] A. Kobyakov, M. Sauer, and D. Chowdhury. Stimulated Brillouin scattering in optical fibers. *Advances in Optics and Photonics*, 2(1):1–59, 2010.

[24] Z. Bo, L.S. Yan, J.Y. Yang, I. Fazal, and A.E. Willner. A single slow-light element for independent delay control and synchronization on multiple Gb/s data channels. *IEEE Photonics Technology Letters*, 19(14):1081–1083, 2007.

[25] R. Zhang, Y. Zhu, J. Wang, and D.J. Gauthier. Slow light with a swept-frequency source. *Optics Express*, 18, 2010.

[26] Z. Shi and R.W. Boyd. Slow-light interferometry: Practical limitations to spectroscopic performance. *Journal of the Optical Society of America B*, 25(12):C136–C143, 2008.

[27] Z. Shi, R.W. Boyd, R.M. Camacho, P.K. Vudyasetu, and J.C. Howell. Slow-light Fourier transform interferometer. *Physical Review Letters*, 99(24):240801, 2007.

[28] A. Schweinsberg, Z. Shi, J.E. Vornehm, and R.W. Boyd. Demonstration of a slow-light laser radar. *Optics Express*, 19(17):15760–15769, 2011.

[29] Y.A. Vlasov, M. O'Boyle, H.F. Hamann, and S.J. McNab. Active control of slow light on a chip with photonic crystal waveguides. *Nature*, 438(7064):65–69, 2005.

[30] M.S. Bigelow, N.N. Lepeshkin, and R.W. Boyd. Observation of ultraslow light propagation in a ruby crystal at room temperature. *Physical Review Letters*, 90(11):113903–113903, 2003.

[31] M. González Herráez, K.Y. Song, and L. Thévenaz. Arbitrary-bandwidth Brillouin slow light in optical fibers. *Optics Express*, 14(4):1395–1400, 2006.

[32] M. Gonzalez-Herraez, K.Y. Song, and L. Thevenaz. Optically controlled slow and fast light in optical fibers using stimulated Brillouin scattering. *Applied Physics Letters*, 87:081113, 2005.

[33] B. Zhang, L. Yan, L. Zhang, and A.E. Willner. Multichannel SBS slow light using spectrally sliced incoherent pumping. *Journal of Lightwave Technology*, 26(23):3763–3769, 2008.

[34] M.A. Neifeld and M. Lee. Information theoretic framework for the analysis of a slow-light delay device. *Journal of the Optical Society of America B*, 25(12):31–38, 2008.

[35] M.J. Damzen, V. Vlad, A. Mocofanescu, and V. Babin. *Stimulated Brillouin scattering: Fundamentals and applications*. Taylor and Francis, first edition, 2003.

[36] M.D. Stenner, M.A. Neifeld, Z. Zhu, A.M.C. Dawes, and D.J. Gauthier. Distortion management in slow-light pulse delay. *Optics Express*, 13(25):9995–10002, 2005.

[37] K.Y. Song and K. Hotate. 25 GHz bandwidth Brillouin slow light in optical fibers. *Optics Letters*, 32(3):217–219, 2007.

[38] T. Sakamoto, T. Yamamoto, K. Shiraki, and T. Kurashima. Low distortion slow light in flat Brillouin gain spectrum by using optical frequency comb. *Optics Express*, 16(11):8026–8032, 2008.

[39] N.A. Olsson and J.P. Van Der Ziel. Fibre Brillouin amplifier with electronically controlled bandwidth. *Electronics Letters*, 22(9):488–490, 1986.

[40] A. Zadok, A. Eyal, and M. Tur. Extended delay of broadband signals in stimulated Brillouin scattering slow light using synthesized pump chirp. *Optics Express*, 14(19):8498–8505, 2006.

[41] L. Yi, Y. Jaouen, W. Hu, Y. Su, and S. Bigo. Improved slow-light performance of 10 Gb/s NRZ, PSBT and DPSK signals in fiber broadband SBS. *Optics Express*, 15(25):16972–16979, 2007.

[42] R. Pant, M.D. Stenner, M.A. Neifeld, and D.J. Gauthier. Optimal pump profile designs for broadband SBS slow-light systems. *Optics Express*, 16(4):2764–2777, 2008.

[43] A.L. Gaeta and R.W. Boyd. Stochastic dynamics of stimulated Brillouin scattering in an optical fiber. *Physical Review A*, 44(5):3205–3209, 1991.

[44] S. Le Floch and P. Cambon. Theoretical evaluation of the Brillouin threshold and the steady-state Brillouin equations in standard single-mode optical fibers. *Journal of the Optical Society of America A*, 20(6):1132–1137, 2003.

[45] R.W. Boyd, K. Rzążewski, and P. Narum. Noise initiation of stimulated Brillouin scattering. *Physical Review A*, 42(9):5514–5521, 1990.

[46] P. Gysel and R.K. Staubli. Statistical properties of Rayleigh backscattering in single-modefibers. *Journal of Lightwave Technology*, 8(4):561–567, 1990.

[47] P. Maine, D. Strickland, P. Bado, M. Pessot, and G. Mourou. Generation of ultrahigh peak power pulses by chirped pulse amplification. *Journal of Quantum Electronics*, 24(2):398–403, 1988.

[48] A. Chong, W.H. Renninger, and F.W. Wise. All-normal-dispersion femtosecond fiber laser with pulse energy above 20nj. *Optics Letters*, 32(16):2408–2410, 2007.

[49] L. Zhang, C. Silberhorn, and I.A. Walmsley. Secure quantum key distribution using continuous variables of single photons. *Physical Review Letters*, 100(11):110504, 2008.

[50] J. Mower, Z. Zhang, P. Desjardins, C. Lee, J.H. Shapiro, and D. Englund. High-dimensional quantum key distribution using dispersive optics. *Physical Review A*, 87(6):062322, 2013.

[51] J.M. Donohue, M. Agnew, J. Lavoie, and K.J. Resch. Coherent ultrafast measurement of time-bin encoded photons. *Physical Review Letters*, 111:153602, Oct 2013.

[52] P. Bowlan and R. Trebino. Complete single-shot measurement of arbitrary nanosecond laser pulses in time. *Optics Express*, 19:1367–1377, 2011.

[53] Y. Zhu, J. Kim, and D. J. Gauthier. Aberration-corrected quantum temporal imaging system. *Physical Review A*, 87:043808, Apr 2013.

[54] Andrew Weiner. *Ultrafast optics*, volume 72. John Wiley & Sons Inc., 2009.

[55] J. Yao. A tutorial on microwave photonics. *IEEE Photonics Society Newsletter*, pages 5–12, 2012.

[56] M. Fridman, A. Farsi, Y. Okawachi, and A.L. Gaeta. Demonstration of temporal cloaking. *Nature*, 481(7379):62–65, 2012.

[57] R.M. Shelby, M.D. Levenson, and P.W. Bayer. Guided acoustic-wave Brillouin scattering. *Physical Review B*, 31(8):5244, 1985.

[58] M.S. Kang, A. Nazarkin, A. Brenn, and P.St.J. Russell. Tightly trapped acoustic phonons in photonic crystal fibres as highly nonlinear artificial raman oscillators. *Nature Physics*, 5(4):276–280, 2009.

[59] M.S. Kang, A. Brenn, G.S. Wiederhecker, and P.St.J. Russell. Optical excitation and characterization of gigahertz acoustic resonances in optical fiber tapers. *Applied Physics Letters*, 93(13):131110–131110, 2008.

[60] N. Shibata, A. Nakazono, N. Taguchi, and S. Tanaka. Forward Brillouin scattering in holey fibers. *Photonics Technology Letters, IEEE*, 18(2):412–414, 2006.

[61] J. Beugnot, T. Sylvestre, H. Maillotte, G. Mélin, and V. Laude. Guided acoustic wave Brillouin scattering in photonic crystal fibers. *Optics Letters*, 32(1):17–19, 2007.

[62] P.St.J. Russell, D. Culverhouse, and F. Farahi. Experimental observation of forward stimulated Brillouin scattering in dual-mode single-core fibre. *Electronics Letters*, 26(15):1195–1196, 1990.

[63] M.S. Kang, A. Brenn, and P.St.J. Russell. All-optical control of gigahertz acoustic resonances by forward stimulated interpolarization scattering in a photonic crystal fiber. *Physical Review Letters*, 105(15):153901, 2010.

[64] P. Dainese, P.St.J. Russell, G.S. Wiederhecker, N. Joly, H.L. Fragnito, V. Laude, and A. Khelif. Raman-like light scattering from acoustic phonons in photonic crystal fiber. *Optics Express*, 14(9):4141–4150, 2006.

[65] K. Okamoto. *Fundamentals of optical waveguides*. Academic Pr, second edition, 2010.

[66] G.P. Agrawal. *Application of nonlinear fiber optics*. Academic Pr. second edition, 2010.

[67] M. Born and E. Wolf. *Principle of optics*. Cambridge University Press, seventh edition, 1999.

[68] R.W. Boyd. *Nonliner optics*. Academic Pr, second edition, 2003.

[69] R.W. Boyd, K. Rzaewski, and P. Narum. Noise initiation of stimulated Brillouin scattering. *Physics Review A*, 42:5514, 1965.

[70] R.W. Boyd, D.J. Gauthier, A.L. Gaeta, and A.E. Willner. Maximum time delay achievable on propagation through a slow-light medium. *Physical Review A*, 71:023801, 2005.

[71] A. Zadok, H. Shalom, M. Tur, W.D. Cornwell, and I. Andonovic. Spectral shift and broadening of DFB lasers under direct modulation. *IEEE Photonic Technology Letters*, 10(12):1709, 1998.

[72] P. Narum, A.L. Gaeta, M.D. Skeldon, and R.W. Boyd. Instabilities of laser beams counterpropagating through a Brillouin-active medium. *Journal of the Optical Society of America B*, 5(3):623–628, 1988.

[73] Myungjun Lee, Yunhui Zhu, Daniel J Gauthier, Michael E Gehm, and Mark A Neifeld. Information-theoretic analysis of a stimulated-brillouin-scattering-based slow-light system. *Applied Optics*, 50(32):6063–6072, 2011.

[74] T.M. Cover and J.A. Thomas. *Elements of information theory*. Wiley-Interscience, second edition, 2006.

[75] Z. Shi, R. Pant, Z. Zhu, M.D. Stenner, M.A. Neifeld, D.J. Gauthier, and R.W. Boyd. Design of a tunable time-delay element using multiple gain lines for increased fractional delay with high data fidelity. *Optics Letters*, 32(14):1986–1988, 2007.

[76] A. Minardo, R. Bernini, and L. Zeni. Low distortion Brillouin slow light in optical fibers using am modulation. *Optics Express*, 14(13):5866–5876, 2006.

[77] E. Brinkmeyer. Analysis of the backscattering method for single-mode optical fibers. *Journal of the Optical Society of America*, 70(8):1010–1012, 1980.

[78] M. Nakazawa. Rayleigh backscattering theory for single-mode optical fibers. *Journal of the Optical Society of America*, 73(9):1175–1180, 1983.

[79] R.H. Stolen, J.P. Gordon, W.J. Tomlinson, and H.A. Haus. Raman response function of silica-core fibers. *Journal of the Optical Society of America B*, 6(6):1159–1166, 1989.

[80] E.M. Dianov, P.V. Mamyshev, A.M. Prokhorov, and S.V. Chernikov. Generation of a train of fundamental solitons at a high repetition rate in optical fibers. *Optics Letters*, 14(18):1008–1010, 1989.

[81] E. Brainis, D. Amans, and S. Massar. Scalar and vector modulation instabilities induced by vacuum fluctuations in fibers: Numerical study. *Physics Review A*, 71:023808, 1987.

[82] Solange B. Cavalcanti, Govind P. Agrawal, and M. Yu. Noise amplification in dispersive nonlinear media. *Physics Review A*, 51(5):4086–4092, 1995.

[83] A. Mussot, E. Lantz, H. Maillotte, T. Sylvestre, C. Finot, and S. Pitois. Spectral broadening of a partially coherent CW laser beam in single-mode optical fibers. *Optics Express*, 12(13):2838–2843, 2004.

[84] A. Demircan and U. Bandelow. Supercontinuum generation by the modulation instability. *Optics Communications*, 244(1-6):181–185, 2005.

[85] L.G. Cohen and C. Lin. Pulse delay measurements in the zero material dispersion wavelength region for optical fibers. *Applied Optics*, 16(12):3136–3139, 1977.

[86] K. Tai, A. Hasegawa, and A. Tomita. Observation of modulational instability in optical fibers. *Physics Review Letters*, 56(2):135–138, 1986.

[87] N. Olsson and Van D.J. Characteristics of a semiconductor laser pumped Brillouin amplifier with electronically controlled bandwidth. *Journal of Lightwave Technology*, 5(1):147–153, 1987.

[88] K.Y. Song, M. Herráez, and L. Thévenaz. Observation of pulse delaying and advancement in optical fibers using stimulated Brillouin scattering. *Optics Express*, 13(1):82–88, 2005.

[89] Y. Okawachi, M.S. Bigelow, J.E. Sharping, Z. Zhu, A. Schweinsberg, D.J. Gauthier, R.W. Boyd, and A.L. Gaeta. Tunable all-optical delays via Brillouin slow light in an optical fiber. *Physical Review Letters*, 94:153902, 2003.

[90] J.A. Greenberg and D.J. Gauthier. Transient dynamics and momentum redistribution in cold atoms via recoil-induced resonances. *Physical Review A*, 79(3):033414, 2009.

[91] S.P. Shipman and S. Venakides. Resonant transmission near nonrobust periodic slab modes. *Physical Review E*, 71(2):026611, 2005.

[92] S.H. Mousavi, I. Kholmanov, K.B. Alici, D. Purtseladze, N. Arju, K. Tatar, D.Y. Fozdar, J.W. Suk, Y. Hao, and A.B. Khanikaev. Inductive tuning of fano-resonant metasurfaces using plasmonic response of graphene in the mid-infrared. *Nano Letters*, 13(3):1111–1117, 2013.

[93] R. Singh, I.A. Al-Naib, M. Koch, and W. Zhang. Sharp fano resonances in thz metamaterials. *Optics Express*, 19(7):6312–6319, 2011.

[94] J. Wang, Y. Zhu, R. Zhang, and D.J. Gauthier. FSBS resonances observed in a standard highly nonlinear fiber. *Optics Express*, 19(6):5339–5349, 2011.

[95] E.K. Sittig and G.A. Coquin. Visualization of plane-strain vibration modes of a long cylinder capable of producing sound radiation. *The Journal of the Acoustical Society of America*, 48:1150, 1970.

[96] M.W. Haakestad and J. Skaar. Slow and fast light in optical fibers using acoustooptic coupling between two co-propagating modes. In *SPIE OPTO: Integrated Optoelectronic Devices*, pages 72260F–72260F. International Society for Optics and Photonics, 2009.

[97] E. Peral and A. Yariv. Degradation of modulation and noise characteristics of semiconductor lasers after propagation in optical fiber due to a phase shift induced by stimulated Brillouin scattering. *Journal of Quantum Electronics*, 35(8):1185–1195, 1999.

[98] A.J. Poustie. Bandwidth and mode intensities of guided acoustic-wave Brillouin scattering in optical fibers. *Journal of the Optical Society of America B*, 10(4):691–696, 1993.

[99] D. Pohl and W. Kaiser. Time-resolved investigations of stimulated Brillouin scattering in transparent and absorbing media: Eetermination of phonon lifetimes. *Physical Review B*, 1(1):31, 1970.

[100] R. Pant, C.G. Poulton, D. Choi, E. Li, S.J. Madden, B. Luther-Davies, and B.J. Eggleton. On-chip stimulated Brillouin scattering. *Optics Express*, 19(9).

[101] H. Shin, W. Qiu, R. Jarecki, J.A. Cox, R.H. Olsson III, A. Starbuck, Z. Wang, and P.T. Rakich. Tailorable stimulated Brillouin scattering in nanoscale silicon waveguides. *Nature Communications*, 4, 2013.

[102] G. Bahl, K.H. Kim, W. Lee, J. Liu, X. Fan, and T. Carmon. Brillouin cavity optomechanics with microfluidic devices. *Nature Communications*, 4, 2013.

[103] M. Aspelmeyer, S. Gröblacher, K. Hammerer, and N. Kiesel. Quantum optomechanics – throwing a glance [invited]. *Journal of the Optical Society of America B*, 27(6):A189–A197, 2010.

Biography

Yunhui Zhu receives her B.S degree in Physics from Peking University in 2008. She pursued Ph.D degree in Professor Gauthier's group in Duke University. She received Walter Gordy Graduate Fellowship in 2011. Her research has been focused on nonlinear and quantum optics in optical fiber. Particularly, she has investigated in application and optimization of stimulated-Brillouin-scattering based slow light for optical buffer and optical coherence tomography. She also conducted the research in the area of quantum communication and networking to develop quantum circuits that connect hybrid quantum memories.

Below is a list of her publication and conference presentations.

Journal articles

1. Y. Zhu, J. Kim, and D.J. Gauthier, "Aberration-corrected quantum temporal imaging," Physical Review A **87**, 043808 (2013).

2. M. Lee, Y. Zhu, D.J. Gauthier, M.E. Gehm, and M.A. Neifeld, "Information-theoretic analysis of a stimulated-Brillouin-scattering-based slow-light system," Applied Optics **50**, 6063 (2011).

3. Y. Zhu, M. Lee, M.A. Neifeld, D.J. Gauthier, "High-fidelity, broadband stimulated-Brillouin-scattering-based slow light using fast noise modulation," Optics Express **19**, 687-697 (2011).

4. J. Wang,* Y. Zhu,* R. Zhang and D.J. Gauthier, "FSBS resonance observed in a

standard highly-nonlinear fiber," Optics Express **19**, 5339(2011), *Co-First Author.

5. R. Zhang, Y. Zhu, J. Wang and D.J. Gauthier "Slow light with a frequency swept source," Optics Express **18**, 27263(2010).

6. Y. Zhu, E. Cabrera-Granado,O.G. Calderson, S. Melle, Y. Okawachi, A.L. Gaeta, D.J. Gauthier, "Competition between the modulation instability and stimulated Brillouin scattering in a broadband slow light device," Journal of Optics **12**, 104019 (2010).

Peer-reviewed conference proceedings

1. D.J. Gauthier, G. Hannah, Y. Zhu, M. Shi, K. McCusker, B. Christensen, P. Kwiat, T. Brougham, S.M. Barnett, and V. Chandar, "Quantum Key Distribution Using Hyperentanglement," in Research in Optical Sciences, OSA Technical Digest, paper QT4A.2, Optical Society of America, (2012)

2. Y. Zhu, J. Kim and D.J. Gauthier, "Selective phased-matched Bragg scattering for single-photon frequency conversion in a nonlinear waveguide," Photonics Society Summer Topical Meeting Series, IEEE **47-48** (2011).

3. Y. Zhu, J. Wang, R. Zhang and D.J. Gauthier, "Interference of FSBS and Kerr effect in a standard highly-nonlinear fiber," Proc. SPIE **7917**, 79170Z (2011).

4. R. Zhang, Y. Zhu, J. Wang, and D.J. Gauthier, "Fiber-length dependence of slow light with a frequency source," Proc. SPIE, **7949**, 794909 (2011).

5. Y. Zhu, J. Wang, R. Zhang and D.J. Gauthier, "Observation of Forward Stimulated Brillouin Scattering in a Standard Highly-Nonlinear Fiber," in Frontiers of Optics, OSA Technical Digest, paper FThA5, Optical Society of America, (2010).

6. R. Zhang, Y. Zhu, J. Wang and D.J. Gauthier, “Broadband Slow Light with a Swept-Frequency Source,” in Frontiers in Optics, OSA Techniqcal Digest, paper FThH3, Optical Society of America, (2010).

Conference Presentations

1. Y. Zhu, J.A. Greenberg, and D. J. Gauthier, “Group velocity dispersion engineering,” invited oral presentation at Photonics West (2013).

2. Y. Zhu, J. Kim, and D. J. Gauthier, “Selective phase-matched Bragg scattering for single-photon frequency conversion in a nonlinear waveguide,” oral presentation at IEEE Photonics Society Summer Topical Meeting (2011).

3. Y. Zhu, J. Kim, and D. J. Gauthier, “Flying qubit interface for hybrid quantum circuits,” poster presentation at Fitzpatrick Institution of Photonics (FIP) 11th Annual Symposium (2011).

4. Y. Zhu, J. Wang, R. Zhang, and D.J. Gauthier, “Forward stimulated Brillouin scattering observed in standard highly-nonlinear optical fiber,” oral presentation at Photonics West (2011).

5. Y. Zhu, J. Wang, R. Zhang, D.J. Gauthier, “Observation of forward stimulated Brillouin scattering in a standard highly-nonlinear fiber,” oral presentation at Frontiers in Optics (FiO)/Laser Science XXVI (LS) Conference (2010).

6. Y. Zhu, M. Lee, M.A. Neifeld and D.J. Gauthier, “Study of the noise characteristics of stimulated-Brillouin-scattering-based slow-light buffers,” poster presentation at Fitzpatrick Institution of Photonics (FIP) 9th Annual Symposium (2009).

7. Y. Zhu and D.J. Gauthier, “Increasing Slow Light Delay via Stimulated Brillouin Scattering by suppressing the modulation instability,” poster presentation at Fitzpatrick Institution of Photonics (FIP) 8th Annual Symposium (2008).

She holds the membership of the following organizations.

- Student member of the American Physics Society
- Student member of the Optical Society of America
- Student member of SPIE
- Student member of IEEE

She has recieved the following honors and awards during the graduate study.

- 2012-2013 Gordy Fellowship of Duke Physics
- 2010 Student Travel Grant Award from the APS Division of Laser Science
- 2008-2009 Gordy Fellowship of Duke Physics
- 2008 Outstanding Teaching Assistant of the Year, American Association of Physics Teachers
- 2007-08 Charles H. Townes Fellowship and James B. Duke Fellowship
- 2005-06 Chun-Tsung Scholar Undergraduate Research Endowment
- 2004 Mary Kay Scholarship for exceptional female student